Carbon Trends 20 (2025) 100551

Contents lists available at ScienceDirect

Carbon Trends

journal homepage: www.elsevier.com/locate/cartre

Recent advancements in MXene-based catalysts: Synthesis, characterization, and applications in sustainable energy production

Nur-Sultan Mussa [a], Kydyr Askaruly [b], Kalampyr Bexeitova [b], Seitkhan Azat [b], Kainaubek Toshtay [b,c,*]

[a] Lille University, Lille, 59000, France
[b] Laboratory of Engineering Profile, Satbayev University, Almaty, Kazakhstan
[c] Faculty of Chemistry and Chemical Technology, Al-Farabi Kazakh National University, Almaty, 050040, Kazakhstan

ARTICLE INFO

Keywords:
Selective etching
Two-dimensional materials
MXene-based catalysts
Hydrocarbon fuel

ABSTRACT

MXenes have emerged as promising two-dimensional (2D) materials for catalytic applications in energy production due to their exceptional structural, electronic, and chemical properties. Their high surface area, tunable surface terminations, and excellent electrical conductivity make them ideal candidates for facilitating surface reactions and enhancing charge transfer processes. Additionally, the ability to modify their composition and structure at the atomic level allows for the design of tailored MXene-based catalysts suited for various energy-related reactions. This review highlights recent advancements in MXene-based catalysts, focusing on novel synthesis techniques, including selective etching, CVD and ALD, as well as advanced characterization methods such as XRD, Raman spectroscopy, TEM, FTIR, and *In-situ*/Operando techniques. Their applications in key catalytic processes, including the Fischer-Tropsch synthesis of hydrocarbons, CO_2 hydrogenation to methane, and hydrogen production via electrochemical water splitting, are discussed, as these reactions play a crucial role in carbon utilization, energy storage, and the transition to sustainable fuels. Notably, Mo_2C-based catalysts favor heavier hydrocarbon formation, while NiV oxycarbide electrocatalysts exhibit high durability and hydrogen selectivity. These findings emphasize MXenes' potential in sustainable energy conversion and highlight the need for further optimization to enhance their catalytic efficiency and stability.

1. Introduction

MXenes, a class of two-dimensional materials composed of transition metal carbides, nitrides, and carbonitrides, have become a focal point of scientific interest due to their exceptional properties. These include adjustable flexibility, tailored optical and electronic behaviors, high electrical conductivity, versatile surface chemistry, robust chemical stability, resistance to chemicals, and active metal hydroxide sites [1–10]. Their structure, represented by the formula $M_{n+1}X_nT_x$ ($n = 1–4$), consists of $n + 1$ as transition metal layers (M) interspersed with carbon, nitrogen, or a combination thereof (X), and terminated with surface functional groups (T_x) like -Cl, -O, -F, or –OH [11–13]. Numerous distinct MXene compounds have been successfully produced, with the potential for many more [14–17]. Their applications span various fields, electromagnetic shielding, including electrochemistry, gas sensing, wireless communication, and biology [18–25]. However, a significant challenge lies in the tendency of MXene sheets to aggregate during synthesis, primarily due to van der Waals interactions and π–π stacking between adjacent layers. This aggregation leads to altered interlayer spacing and a reduction in active sites, consequently impacting catalytic processes and diminishing recyclability and long-term stability [26–29]. To address these issues, researchers are focusing on creating MXene derivatives and hybrids by manipulating surface functional groups and controlling surface oxidation [30]. Compositing MXenes with materials such as conducting polymers, metal sulfides, graphene, carbon nanotubes, and metal nanoparticles is also being explored. These strategies aim to leverage MXenes' unique characteristics in electrochemical applications. Both pure MXenes and MXene-based composites have shown promise as catalysts in energy storage and electrochemical energy conversion, yielding highly encouraging results. The affordability and comparable performance of MXenes to expensive noble metal catalysts make them highly sought after for energy applications [31–33].

Furthermore, MXenes have a greater density of surface functional groups than graphene, which improves their ability to interact with

* Corresponding author.
E-mail address: kainaubek.toshtay@kaznu.kz (K. Toshtay).

https://doi.org/10.1016/j.cartre.2025.100551
Received 29 May 2025; Received in revised form 11 July 2025; Accepted 26 July 2025
Available online 29 July 2025
2667-0569/© 2025 The Authors. Published by Elsevier Ltd. This is an open access article under the CC BY-NC license (http://creativecommons.org/licenses/by-nc/4.0/).

reactant molecules. MXenes are superior compared to their competitive counterparts, such as graphene and 2D MoS_2, in some electrocatalytic reactions, such as the oxygen reduction reaction (ORR) and hydrogen evolution reaction (HER), because of their tunable catalytic characteristics, which are made possible by the presence of transition metal atoms [34,35]. Graphene, on the other hand, requires doping or decorating with metal nanoparticles due to its lack of intrinsic active sites. Because of its high density of active edge sites, MoS_2 shows exceptional catalytic performance, especially in its 1T phase [36]. In contrast to MXenes, its electrical conductivity is limited by its semiconducting nature. MoS_2 still has difficulties in large-scale catalytic applications, despite the fact that techniques like phase engineering and heterostructure synthesis have enhanced its catalytic performance. Under normal circumstances, graphene is oxidation-resistant and chemically stable. High temperatures and oxidative atmospheres can cause MoS_2 to oxidize, despite its stability in a variety of conditions. Even though MXenes have promising qualities, they oxidize with time, especially in wet or humid settings, which can impair their catalytic activity [37]. MXene-based catalysts are currently employed in a broad spectrum of catalytic reactions. A general illustration of these applications is provided in Fig. 1. Addressing this stability issue is critical for the practical use of MXenes in catalysis. The most recent developments in the application of MXene-based nanomaterials have emerged for a range of catalytic transformations, such as heat catalysis and electrochemical processes. The Suzuki–Miyaura coupling reaction [38], methanol oxidation reaction (MOR) [39], sulfur reduction reaction (SRR) [40], dry reforming of methane (DRM) [41], water-gas shift (WGS) reaction [42], and hydrogen evolution reaction (HER) [43] are some of the critical reactions that were investigated by many researchers. Furthermore, the function of MXenes in light alkane dehydrogenation [44], CO_2 photochemical reduction [45], and alkaline hydrogen evolution [46] is showcased by other research works. Along with a summary of their synthesis procedures and structural alterations, they addressed the catalysts' functionality, characterisation methodologies, and recyclability.

Catalytic processes, which are essential to renewable energy technologies, are increasingly being investigated using these two-dimensional MXene materials. Usually derived from renewable sources, the energy utilized in these MXene-catalyzed processes aids in the shift to a low-carbon future (Fig. 2). Syngas from biomass or other renewable feedstocks are transformed into hydrocarbons in Fischer-Tropsch synthesis (FTS) using thermal energy [47]. The advantageous active site configurations and surface chemistry of MXenes, facilitate the synthesis of heavier hydrocarbons. Likewise, in CO_2 hydrogenation to methane, collected carbon dioxide is converted into synthetic natural gas using chemical energy stored in green hydrogen, with MXenes enhancing reaction efficiency and selectivity [48].

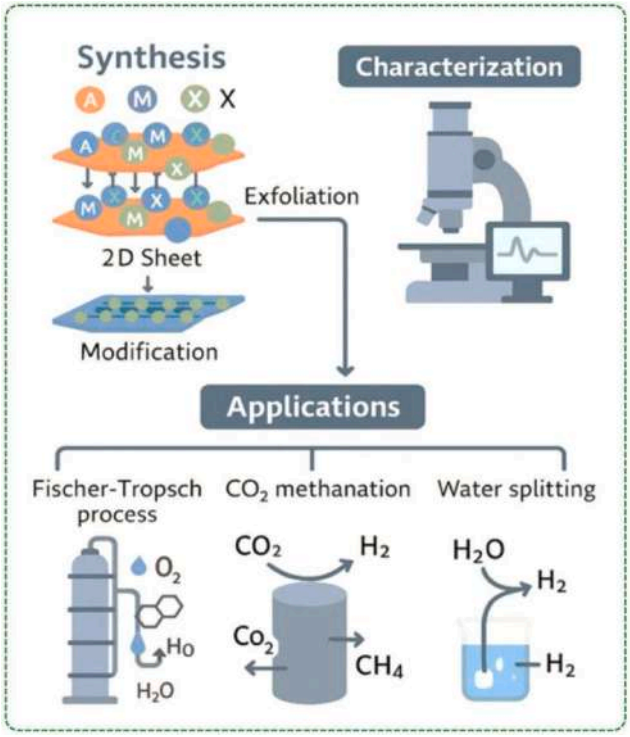


Fig. 2. A brief illustrative review of MXene-based catalysts used in energy technologies.

Furthermore, MXenes are essential to electrochemical water splitting, a method that directly generates hydrogen fuel using renewable electricity. The high conductivity, surface reactivity, and structural tunability of MXene catalysts are advantageous for the HER and ORR, which are the basis of this technique [49,50]. MXenes facilitate more effective hydrogen synthesis from water by reducing activation energy and enhancing catalytic durability, which is crucial for creating a green hydrogen economy. MXene-based catalysts have the potential to facilitate decarbonization and long-term energy storage solutions when

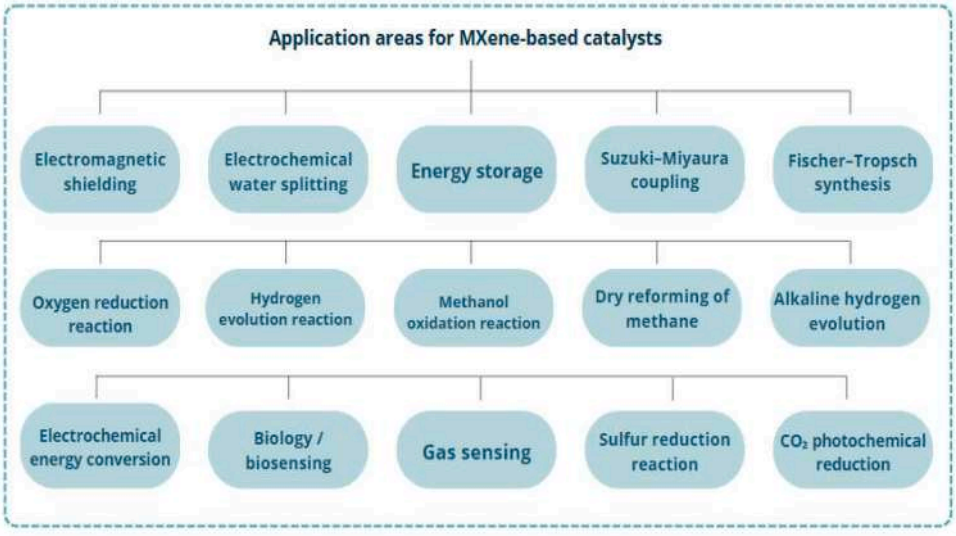


Fig. 1. Applications of MXene-based catalysts in catalytic processes.

included in energy systems [51] that are powered by sustainable inputs, such as heat from biomass [52], green hydrogen [53], and clean electricity [54]. As global energy systems transition toward more sustainable sources, integrating of advanced materials like MXenes becomes increasingly critical. Their unique physicochemical properties enable efficient catalysis in processes essential for carbon-neutral fuel production and storage. By examining both their synthesis and functional roles in key energy conversion reactions, this review highlights the strategic potential of MXenes in shaping a sustainable energy future. Specifically, it examines their role in the Fischer-Tropsch process for hydrocarbon fuel synthesis, CO_2 methanation, and hydrogen production via water splitting. The insights from this comprehensive review will contribute to advancements in the field, fostering future research and innovation.

This review differs from previous research [55,56] in that it focuses extensively on the catalytic processes and synthesis pathways of MXene-based systems, with a particular emphasis on their use in energy-relevant applications such as the hydrogen evolution reaction and Fischer–Tropsch synthesis. This review offers a more detailed comparison of top-down and bottom-up synthesis strategies than other works that frequently provide a broad overview of MXene chemistry. It emphasizes how methods such as electrochemical exfoliation, alkaline activation, and molten salt etching can be customized for particular catalytic results. The incorporation of operando and in situ characterisation techniques with catalytic testing, which offers real-time insights into structural dynamics under operating circumstances, is a noteworthy strength. For instance, the ability of Mo_2C-based MXenes to favor heavier hydrocarbon formation (C_5+ alkanes) in Fischer–Tropsch synthesis is connected to both their intrinsic surface energetics and the morphology achieved via chemical vapor deposition, an angle rarely emphasized in such detail in comparable studies [57–61].

The coverage of MXene-derived NiV oxycarbide catalysts (NiPt@N-VOC) for electrochemical water splitting is also unique in that it links the remarkable durability and hydrogen production rates to structural design principles like metal dispersion and nanosphere formation, rather than just presenting them. The review discusses how tuning redox characteristics and electrical behavior by the introduction of vanadium into MXene-based catalysts provides mechanistic insights that surpass surface-level reporting. Additionally, this work meticulously links the linkages between synthesis, structure, and performance, enabling readers to observe the direct effects of particular etching agents or deposition techniques on catalytic lifespan and product selectivity. This review also functions as a crucial roadmap for customizing MXene catalysts for long-term, industrial-scale energy conversion applications, in addition to being a list of advances pertaining to MXene.

2. Synthesis of MXene-based catalysts

The synthesis of MXene-based catalysts primarily involves the exfoliation of bulk MAX phases as a class of hexagonal-structure ternary carbides and nitrides (“X”) of a transition metal (“M”) and an A-group element into 2D sheets, followed by modifications that enhance their catalytic properties. These alterations may involve surface functionalization, interlayer engineering, and the addition of active metal sites or heteroatoms to customize MXenes for certain catalytic reactions. The selection of synthesis processes has a major impact on MXenes’ structural, electronic, and physicochemical characteristics, all of which have an impact on their catalytic activity. To maximize MXenes for use in heterogeneous catalysis, electrocatalysis, and photocatalysis, a number of strategies have been devised, including selective etching, delamination methods, and hybridization with other materials. MXene-based catalysts can improve stability, reactivity, and selectivity in a variety of catalytic processes by adjusting their shape and composition.

2.1. Top-down approaches

Top-down approaches for the synthesis of MXene-based catalysts involve the selective removal of "A" elements from bulk MAX phases to obtain 2D MXene nanosheets. These techniques mostly rely on chemical etching, in which the bonds between the transition metal (M) and the "A" element (usually Al, Si, or Ga) in the MAX phase are broken by strong acids or solutions containing fluoride. The resultant MXene layers can undergo further processing using delamination procedures to improve their surface area and dispersibility. While maintaining the layered arrangement from the parent MAX phase, top-down synthesis offers greater control over the composition and structural integrity of MXenes than bottom-up approaches. However, in order to optimize these synthesis processes for catalytic applications, issues including chemical stability, scalability, and precise surface termination control continue to be important research topics. All top-down approaches discussed in this section are illustrated in Fig. 3, with each method elaborated upon in the subsequent parts of the section.

2.1.1. Selective etching of MAX phases

Molten salt etching has emerged as a promising method for synthesizing MXenes due to its high efficiency, scalability, and elimination of hazardous HF usage. This method entails heating MAX phases in molten salts like $ZnCl_2$, KCl, or NaCl to high temperatures, usually 500–800 °C. The selective extraction of the A-element from the MAX structure is made easier by the reactive media provided by the molten salt [66].

The molten salt and the A-layer interact during the etching process to create soluble intermediates, such as $AlCl_3$ in the case of Al-based MAX phases, which are then eliminated by post-synthesis washing. This process produces high-purity MXene flakes with fewer defects and lower environmental concerns than HF-based etching. Furthermore, it has been discovered that $ZnCl_2$ increases the etching efficiency while concurrently functionalizing the MXene surface with chloride groups, which can subsequently be altered for specific uses [67]. A work by Rostami and associates investigated the synthesis of Ti_3AlC_2 MAX phases utilizing a molten salt-shielded technique in an air atmosphere [68]. Their study showed that TiO_2-$Ti_3C_2Cl_2$ MXenes may be formed by in situ etching Ti_3AlC_2 with $CuCl_2$ Lewis acid salts at 750 °C.

In the study conducted by Cui et al. [62], the authors developed a CuNi/MXene heterostructure catalyst designed to enhance the electrochemical nitrite reduction reaction (NO_2RR), offering a promising route for environmentally benign ammonia (NH_3) production. Bimetallic hybrid molten salt etching was used to overcome the traditional problems of low NH_3 production and poor Faradaic efficiency. Well-dispersed CuNi alloy nanoparticles (NPs) anchored on the MXene substrate were formed as a result of the selective removal of the Al layer in the MAX phase and the simultaneous reduction of Cu^{2+} and Ni^{2+} salts. CuNi NPs and MXene formed a strong metal–support interaction (MSI) that greatly enhanced NO_2RR performance by preventing nanoparticle agglomeration and facilitating a larger density of accessible active sites. The Cu_x-Ni_y/MXene heterostructure’s synthesis pathway is depicted in Fig. 3a. $CuCl_2$ and $NiCl_2{\cdot}6H_2O$ molten salt combination was used to etch the MAX phase, and the remaining molten salts were subsequently removed to produce the Cu_xNi_y/MXene heterostructure. Because exposed Al has a weak connection with Ti, Cu^{2+} and Ni^{2+} can oxidize Al to Al^{3+}during the etching process, forming the volatile $AlCl_3$. At the same time, Cu^{2+} and Ni^{2+}co-reduce to CuNi NPs. Importantly, the process resulted in the formation of –O and –Cl terminal functional groups on the MXene surface, which enhanced charge distribution and interaction with metal nanoparticles. These groups, along with the improved anchoring of CuNi, suppress nanoparticle aggregation and boost the density of accessible active sites, making the catalyst highly effective in nitrite electro-reduction. The molten salt route thus provides a platform for tuning surface chemistry and achieving structural integration between active metals and the support [69]. The mechanistic interpretation is grounded in the multi-functional role of the CuNi/MXene interface: (i) Cu provides active sites for NO_2 adsorption and activation, (ii) Ni facilitates electron transfer, (iii) MXene stabilizes intermediates via hydrogen bonding and surface polarity, and (iv) DFT studies confirm

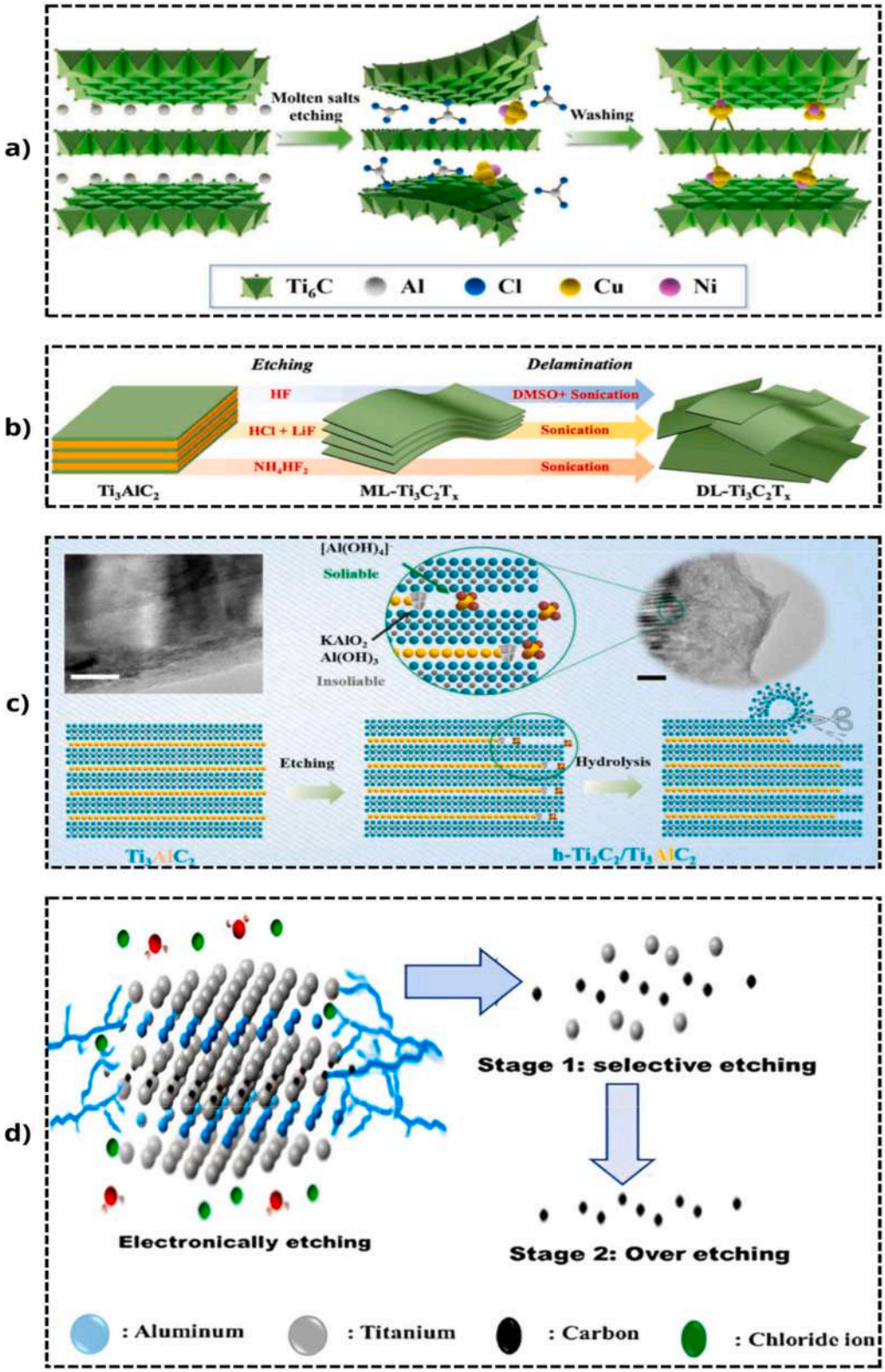
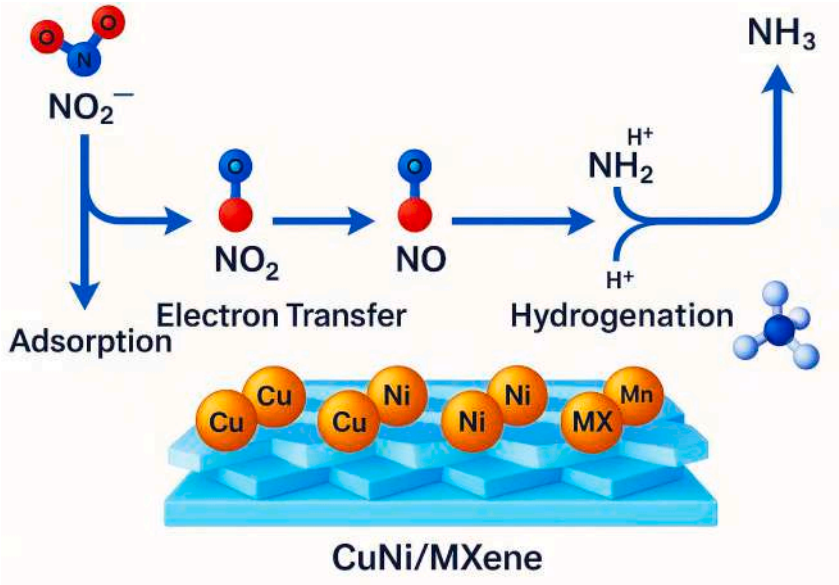


Fig. 3. Schematic representations for: a) synthesis of Cu_xNi_y/MXene composite, b) synthesis method of ML- and DL-Ti_3C_2Tx by various etching and delamination methods, c) h-TC/TAC catalyst preparation, and d) EC etching mechanism of Ti_2CT_x. Reproduced with permission from Ref. [62–65].

low energy barriers for all transformations (Scheme 1).

The d-band center of copper is also moved closer to the Fermi level when copper and nickel are alloyed, which enhances the adsorption of NO_2^- intermediates. Thus, the Cu_3Ni/MXene catalyst showed remarkable performance, with a high Faradaic efficiency of 95.6 % and a high ammonia output of 10.22 mg h^1 mg_cat^1. The Cu_3Ni/MXene combination produced an outstanding power density of 8.34 mW cm^{-2}, an NH_3 production of 1.91 mg h^{-1} mg_cat^{-1}, and a Faradaic efficiency of 90.3 % when used in a Zn–NO_2^- battery. This method allows electricity output, ammonia production, and pollutant nitrite removal all at once.



Scheme 1. Proposed mechanism of NO_2^- reduction over CuNi/MXene catalyst showing key intermediates and transformation steps.

Furthermore, the NO_2RR pathway and mechanism were better understood through the combined application of in situ FTIR spectroscopy and Density Functional Theory (DFT) calculations, which helped to direct the development of more effective catalysts. According to recent developments, molten salt etching greatly enhances MXenes' electrochemical characteristics for supercapacitors and batteries, among other uses. This improvement is ascribed to the fine control it provides over layer thickness and surface termination groups [70,71]. This technique also makes it possible to synthesize unusual MXene compositions, such as those that contain high-entropy elements, which expands the range of accessible MXene materials.

Additionally, fluoride salt etching is a widely adopted method for MXene synthesis due to its simplicity and adaptability. This method usually uses hydrochloric acid (HCl) and fluoride salts, like LiF, NaF, NH_4F or FeF_3, to remove the A-element from MAX phases in a selective manner. The M layers are revealed when the acid dissolves the soluble fluoride complexes that are created when fluoride ions react with the A-element during the etching process [72]. The minimum intensive layer delamination (MILD) approach, which uses HCl and lithium fluoride (LiF) for MXene production, has seen a noteworthy improvement by the work of Sarkar et al. [73,74]. This approach has drawn interest due to its improved performance in a variety of applications, scalability, and reproducibility. For example, $Ti_3C_2T_x$ MXene is made by employing LiF and HCl to selectively etch aluminum atoms from the Ti_3AlC_2 MAX phase in accordance with the MILD protocol. Additionally, this technique produces functional surface termination groups (-OH, -F, and -O), which improve MXenes' hydrophilicity and chemical reactivity.

In the work by Zhang et al., the Cr(VI) removal efficiency of $Ti_3C_2T_x$ MXenes with varying morphologies—specifically multilayered (ML-) and delaminated (DL-) forms—was systematically investigated [63]. Several etching techniques, such as hydrofluoric acid (HF), acid/-fluoride salt, and bifluoride salt etching, were used to create these structures. Delamination techniques were then used. These new synthesis pathways have a major impact on the final MXene morphology and performance, as seen in Fig. 3b The samples that showed the most promise in terms of removing Cr(VI) were ML- and DL-$Ti_3C_2T_x$ made using the acid/fluoride salt etching procedure. Both materials demonstrated quick reduction and adsorption, reaching equilibrium in 500 min. ML-$Ti_3C_2T_x$ had an adsorption capacity of 92.7 mg/g, while DL-$Ti_3C_2T_x$ had a significantly greater capacity of 205 mg/g. This morphological transformation increases surface area, enhances accessibility to active sites, and reduces diffusion limitations. The selective etching and subsequent delamination preserve structural integrity while exposing more reactive edges and terminal groups, improving catalytic or adsorption performance in environmental applications. These results highlight how important structural engineering is to improving MXenes' adsorption capabilities for environmental remediation applications [75]. Thus, fluoride salt etching is crucial for tailoring MXene morphology and maximizing catalytic contact surfaces.

Remarkably, the chemical reduction capacity of DL-$Ti_3C_2T_x$ was slightly limited by its partial oxidation into TiO_2. Through the creation of $Ti_3C_2T_x/TiO_2$ heterojunctions, $Ti_3C_2T_x$ may yet continue to function as a co-catalyst, boosting the photocatalytic activity of TiO_2. This interaction can help with the photoreduction of Cr(VI) and enhance light responsiveness. Overall, both types of $Ti_3C_2T_x$ MXenes show exceptional detoxification and removal capacities for Cr(VI), underscoring their great potential for heavy metal remediation in wastewater treatment.

Alternative fluoride salts, like CoF_2 and $NaBF_4$, have been used to increase layer separation and introduce unique surface terminations in order to further customize MXene characteristics [76]. Furthermore, MXenes with distinct termination groups that are produced by etching with FeF_3 and HCl have shown improved energy storage capacities, especially in lithium-ion batteries [77]. Notwithstanding its benefits, fluoride salt etching has drawbacks, such as the need for dangerous chemicals and the issue of totally eliminating any remaining fluoride ions from the MXene surface, which may affect functionalization later on.

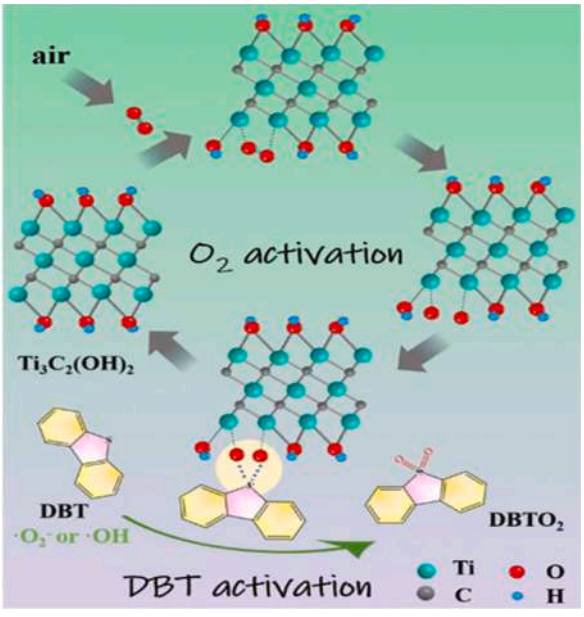
2.1.2. Alkaline etching strategies

Alkali etching has emerged as a promising alternative to acidic etching techniques, utilizing strong bases such as sodium hydroxide (NaOH) or potassium hydroxide (KOH) to selectively remove the A-layer from MAX phases. This process greatly lowers the environmental concerns connected to the production of MXene by doing away with the necessity for dangerous hydrofluoric acid (HF) or fluoride-containing salts [78]. The M-X layers are left behind after the A-element and base react to create soluble hydroxide complexes during alkali etching. For example, magnesium hydride (MgH_2) can be used as a reductant to efficiently promote the extraction of aluminum from Ti_3AlC_2 MAX phases [79]. The resultant MXenes usually have surface terminations like oxygen (-O) and hydroxyl (-OH), which are essential for improving their catalytic and electrochemical capabilities. These functional groups increase MXene's dispersibility in aqueous solutions, which makes them ideal for applications involving electrocatalysis and energy storage [80].

Alkali etching has also been used in recent research to create single-layer MXene nanosheets with customized surface functions. One method is to remove the A-layer from the MAX phase selectively using organic alkali etchants, like tetramethylammonium hydroxide (TMAOH) [81]. Through further dialysis and deionized water intercalation, hydroxyl-functionalized $Ti_3C_2T_x$ (OH-$Ti_3C_2T_x$) can be further delaminated into single-layer nanosheets. This procedure produces a multilayer accordion-like structure. The enhanced stability, conductivity, and adjustable surface chemistry of these hydroxyl-rich MXenes increase their potential uses in electrocatalysis, water purification, and electromagnetic absorption.

Although hydrofluoric acid is frequently utilized in the majority of MXene manufacturing pathways, it presents serious environmental and safety hazards. Zhang et al., on the other hand, developed a safer and greener method by using alkaline etching to create hydroxylated Ti_3C_2/Ti_3AlC_2 (h-TC/TAC) catalysts [64]. This technique started the creation of a surface hydroxylated Ti_3C_2 MXene layer by selectively etching the Ti_3AlC_2 MAX phase using an alkali solution. Ti–C bonds at the surface were partially hydrolyzed as a result of this process, revealing additional active sites that are essential for catalytic activity. The synthesis technique for h-TC/TAC catalysts consists of two easy but efficient processes, as shown in Fig. 3c. The Ti_3AlC_2 MAX phase is first etched alkalinely to start the process. Particularly in conditions of water-assisted heating that enhance reaction kinetics, the alkali's potent corrosiveness permits a selective interaction with the aluminum layers in Ti_3AlC_2 [82–88]. The development of passivating oxide and/or hydroxide layers on the MAX surface can restrict the etching process by preventing more reaction, even though in theory the entire aluminum can be removed. The catalyst's surface chemistry and electronic structure are successfully altered by this technique, which concentrates the catalytic active sites and improves substrate activation and conversion efficiency [89]. The generated catalyst demonstrated a desulfurization rate of up to 99 % for the aerobic oxidative desulfurization of a model fuel with a sulfur concentration of 220 ppm when air was used as a low-cost molecular oxygen source. The constant activation of molecular oxygen to produce •OH and $\bullet O_2^-$was thought to be the cause of the h-TC/TAC catalyst's increased activity.

In the oxidative desulfurization (ODS) reaction catalyzed by h-TC/TAC-5–120, the deactivation of the catalyst demonstrates that the most significant active species are the •OH and $\bullet O_2^-$ radicals (Scheme 2).



Scheme 2. Proposed mechanism of oxidative desulfurization. Reproduced with permission from Ref. [64].

These discoveries have led to the proposal of a catalytic route. First, a large number of active sites with Ti–OH and Ti–O groups on the surface of h-TC/TAC-5–120 are revealed by the alkaline etching method. •OH and $\bullet O_2^-$ radicals are created within the catalyst structure when the oxidant reacts with these surface Ti–OH or Ti–O species at the start of the ODS process. The results of the electron spin resonance (ESR) test, which verify that the radicals can be produced under the reaction conditions, support the theory that oxygen molecules from the surrounding air play a role in the creation of these radicals. The activation and oxidation of aromatic sulfide compounds precisely take place at the nanoscale surface layer of the catalyst, where these active sites are concentrated as a result of the etching process stopping. The two radical species then oxidize dibenzothiophene (DBT) once it has been adsorbed on the catalytic surface. At the same time, the constant flow of air, the oxidant, guarantees a constant production of new radicals, maintaining the catalytic activity.

Overall, alkaline etching provides a safer, HF-free alternative to MXene synthesis while introducing desirable structural defects and hydroxyl terminations that significantly influence catalytic properties. Moreover, the formation of passivating oxide layers, while limiting complete etching, strategically confines defect formation to specific regions, promoting selective substrate interaction. These hydroxylated sites serve as proton donors or adsorption anchors, which are particularly relevant in aqueous-phase or redox reactions. The increased density of catalytic sites and improved electron density distribution make alkaline-etched MXenes highly suitable for reactions requiring strong metal–support synergy and surface reactivity. Additionally, it offers a productive and sustainable method for synthesizing MXene while allowing for exact control over surface functions. To improve the etching procedure and broaden its application to a larger variety of MAX phases, more study is necessary [90].

2.1.3. *Electrochemical etching*

Electrochemical etching is an innovative technique for MXene synthesis that utilizes an applied electrical potential to control the etching process precisely. This technique involves submerging the MAX phase in an electrolyte solution, usually one that contains fluoride or chloride ions, and then applying a voltage to it. As a result, the A-layer is selectively oxidized and dissolved by an electrochemical process, leaving behind MXene layers with minor structural flaws and adjustable surface chemistry [90].

By altering the electrolyte composition and applied voltage, electrochemical etching may fine-tune the characteristics of MXene, which accounts for its adaptability. $Ti_3C_2T_x$ MXenes have been successfully synthesized using electrolytes such as NaCl and NaF, resulting in materials functionalized with specific surface groups that enhance their catalytic and electrical properties [91]. A mild electrochemical exfoliation technique was suggested in recent work to produce $Ti_3C_2F_x$ while carefully regulating the level of fluorination [92]. In order to guarantee controlled etching, this method used a sealed three-electrode electrochemical setup, producing MXenes with distinct surface functions and fewer structural defects.

In their comprehensive review, Isa et al. examine the evolving role of MXenes as co-catalysts in hydrogen fuel production through photocatalytic water splitting [65]. Applying a controlled electric potential in electrolyte solutions like NaCl, HCl, or NH_4Cl, using the MAX precursor as an electrode, allows for the effective removal of the A-layer (e.g., Al) in the MAX phase. This technique is based on electron transfer mechanisms during the surface reaction and is primarily influenced by the chemical reactivity of the metal-aluminum (M–A) bonds rather than the stronger metal-carbon (M–C) bonds to eventually produce bilayer or single Ti_2CT_x, as shown in Fig. 3d [93]. Although the EC etching approach produces hydrophilic and accordion-like MXenes, its low yield is caused by the production of CDC layers [94,95]. Therefore, efficient pathways for the large-scale synthesis of MXenes and the removal of CDC layers must be created. The Al layer in the MAX phase is removed

first due to its weaker bond with titanium, which is stronger compared to the bond between titanium and carbon. However, in the second step, only carbon atoms remain when the titanium and aluminum are etched out [96]. As a result, EC etching offers a highly controllable method to produce MXenes with clean surfaces and enhanced hydrophilicity, both of which are essential for catalytic efficiency in aqueous environments. Unlike HF-based routes, EC etching introduces minimal residual contamination, yielding surfaces with well-defined terminations. However, challenges such as the co-formation of carbide-derived carbon (CDC) layers can reduce product yield and must be mitigated. Nevertheless, the high purity and hydrophilic nature of EC-etched MXenes improve their dispersibility, ion accessibility, and interaction with reactants, making them highly effective for electrocatalytic applications like water splitting and CO_2 reduction.

Scalability and environmental sustainability are two of electrochemical etching's main benefits because it does not require the dangerous acids or salts that are frequently employed in chemical etching techniques. It also enables selective surface functionalization, which makes it a desirable choice for energy storage, electronic devices, and catalytic applications. To prevent over-etching or insufficient A-layer removal, it is essential to carefully optimize reaction parameters such as voltage, electrolyte concentration, and etching time.

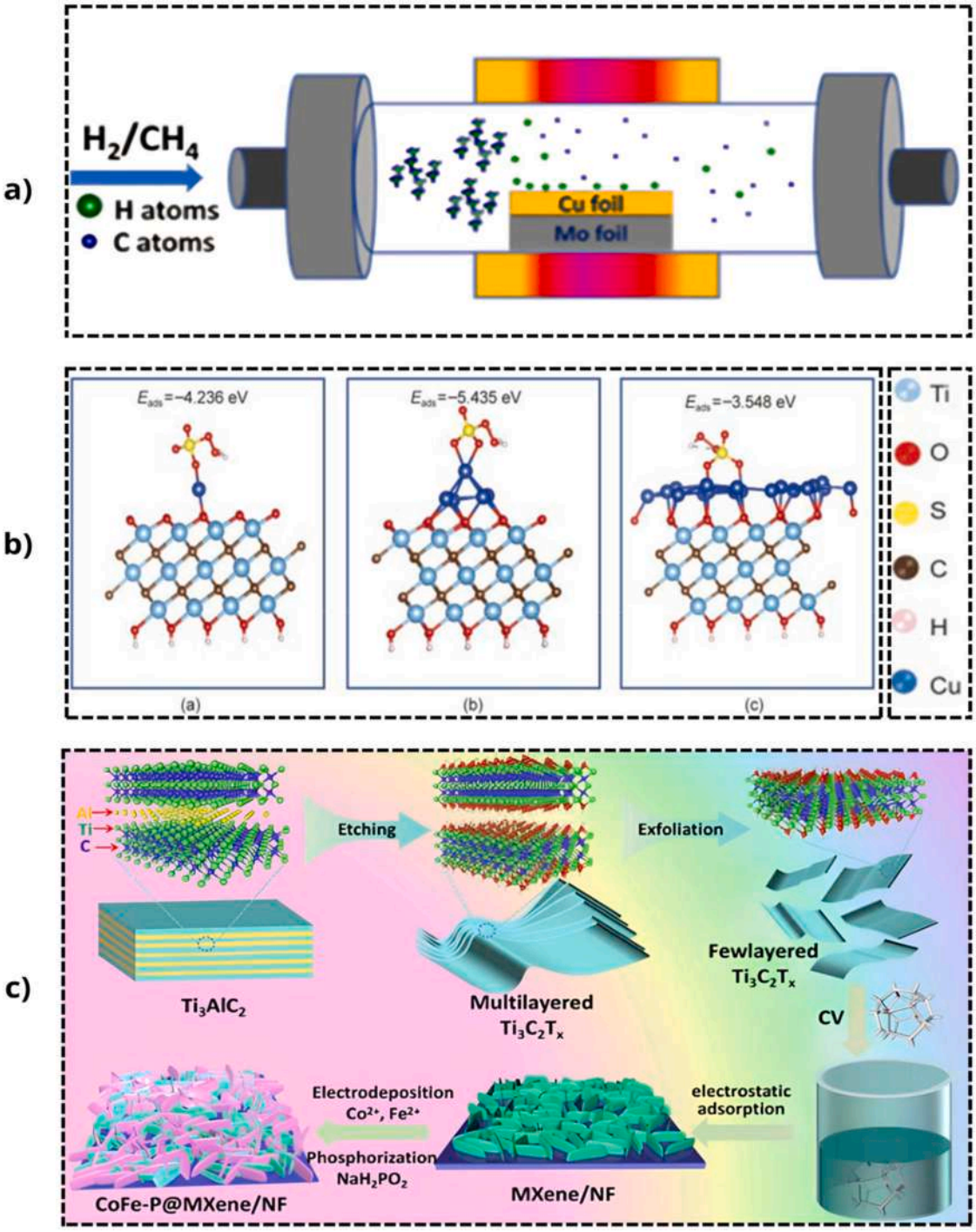


Fig. 4. Illustrations of a) the growth of Mo_2C by CVD method, b) optimization configurations of (a*) SA-Cu-MXene, (b*) C—Cu-MXene, and (c*) F-Cu-MXene, c) the CoFe-P@MXene/NF catalyst preparation steps. Reproduced with permission from Ref. [98–100].

The specific benefits and drawbacks of each etching technique for MXene production vary based on the intended material qualities and applications. One of the most versatile and popular methods for creating different MXene compositions with functionalized surfaces is still fluoride salt etching. In contrast, molten salt etching offers a scalable and environmentally benign substitute that yields high-purity MXenes with few flaws. Although it necessitates strict control over reaction conditions, electrochemical etching offers a high degree of precision and sustainability, making it an attractive alternative to chemical etching. Even though alkali etching is safer and less harmful to the environment, it still needs to be further optimized to improve yield and structural integrity. Improvements in these synthesis methods will increase the potential uses of MXenes in energy storage, catalysis, and other fields as research progresses. Improved control over MXene characteristics could result from combining several etching techniques or creating innovative hybrid approaches, which could lead to innovations in next-generation materials and technology.

2.2. Bottom-up approaches

Bottom-up approaches for material synthesis involve the assembly of atoms, molecules, or small clusters to form larger structures with controlled properties. These techniques are highly effective for designing MXene-based catalysts, providing precise control over thickness, morphology, and composition. Chemical Vapor Deposition (CVD) and Atomic Layer Deposition (ALD) are the most popular bottom-up synthesis methods for fabricating MXene-based thin films and catalytic nanostructured materials with excellent compositional accuracy, scalability, and homogeneity [97]. Electrodeposition is another versatile bottom-up approach, enabling the controlled deposition of metals, metal oxides, or other active phases onto conductive MXene substrates by applying an external electric field. This method is particularly attractive due to its simplicity, low cost, and ability to finely tune the size, distribution, and loading of catalytic species. Fig. 4 visually summarizes all the bottom-up methods discussed in this section, and each method will be explained in more detail later.

2.2.1. Chemical vapor deposition (CVD)

Chemical Vapor Deposition (CVD) is a widely used technique for fabricating thin films and coatings through the chemical reaction of vapor-phase precursors. This method enables the synthesis of MXene-based catalysts by introducing gaseous reactants into a reaction chamber and allowing them to react chemically with a heated substrate [101]. The main benefit of CVD in MXene synthesis is its capacity to create homogeneous, high-purity films with superior conformality and adherence. The energy source and reaction conditions can be used to categorize CVD into several categories. The Plasma enhanced CVD (PECVD) employs plasma to activate precursor molecules, enabling lower deposition temperatures, Thermal CVD depends on high temperatures to induce chemical reactions [98]. Metal-organic CVD (MOCVD) employs metal-organic precursors for fabricating MXene-based catalysts and functionalized MXene-based films for catalytic applications [102]. Because of its scalability and adaptability, CVD is widely used in energy conversion, electrocatalysis, protective coatings, and electronic applications involving MXene materials. However, the procedure frequently calls for dangerous precursors and high temperatures, which can present problems with regard to environmental safety and material compatibility.

2D-Mo_2C (Molybdenum carbide) has emerged as a new member of the MXene group catalytic material due to its high conductivity, stability, and unique surface chemistry, making it suited for energy conversion and chemical synthesis applications. Following the approach of Kimbulapitiya et al. [98], the synthesis of Mo_2C crystals and their related heterostructures was done using chemical vapor deposition (CVD). In order to prevent undesired graphene synthesis, a Mo-thick sheet was applied to a Cu foil and subjected to a low concentration of CH_4 gas precursor, as shown in Fig. 4a. Different morphologies, such as hexagonal, triangular, pentagonal, and quadrangular structures, were displayed by the resulting Mo_2C crystals. This morphological precision allows surface exposure and facet orientation tuning, directly impacting catalytic site density and reactivity. Moreover, the ability to grow continuous thin films enhances electrical conductivity and mechanical stability, both crucial for electrocatalytic and thermocatalytic processes. Unlike top-down methods, CVD introduces fewer defects and allows functionalization via post-treatment, resulting in highly stable, uniform layers ideal for energy conversion reactions.

The presence of a metallic phase and highly active sites produced by plasma-assisted selenium and sulfurization at low temperatures were responsible for the created Mo_2C-based heterostructures' exceptional electrocatalytic performance for HER. However, the shift into a semiconducting phase caused its HER activity to decrease at higher temperatures. All heterostructures, with the exception of Mo_2C/MoO_x, demonstrated outstanding stability during a 10-hour period. This work offers exciting opportunities for enhanced electrocatalysts by introducing novel approaches for creating high-quality MXene and transition metal dichalcogenide (TMD) heterostructures with tailored metal-semiconductor interfaces.

2.2.2. Atomic layer deposition

Atomic Layer Deposition (ALD) is a specialized variant of CVD that enables atomic-level precision in thin film deposition, making it an excellent technique for synthesizing MXene-based catalysts with controlled surface properties [99]. ALD is based on sequential, self-limiting surface reactions, as opposed to traditional CVD, in which precursors are added cyclically one at a time. Prior to surplus material being purged and the subsequent precursor being introduced, each precursor has a controlled reaction with the surface to build a monolayer. Even on intricate 3D MXene nanostructures, ALD guarantees extremely uniform and conformal coatings. Applications needing accurate thickness control and flawless films, like electrocatalysis [103], energy production [104], and advanced functional materials [105] based on MXene, benefit significantly from ALD. Temperature-sensitive MXene substrates can benefit from the process's ability to function at lower temperatures than conventional CVD. ALD also makes it possible to deposit barrier coatings, ultrathin dielectric layers, and catalytic nanomaterials with improved performance attributes. Despite its benefits, ALD's layer-by-layer structure results in slow deposition rates, which may restrict its use in large-scale industrial applications.

Peroxymonosulfate (PMS) activation and contaminant degradation can be strongly impacted by the distribution pattern of metals as active centers on a substrate. By varying the number of deposition cycles, Li et al.'s work [99] used ALD to create Cu single-atom (SA-Cu), cluster (C—Cu), and film (F-Cu) decorated MXene catalysts. With an adsorption energy (Eads) of −5.435 eV, C—Cu-MXene outperformed SA-Cu-MXene (−4.236 eV) and F-Cu-MXene (−3.548 eV) among these configurations, allowing for greater activation efficiency. The SA-Cu-MXene, C—Cu-MXene, and F-Cu-MXene samples' optimization configurations were displayed in Fig. 4b Additionally, structural changes in the O–O bond length (l_{O-O}) with PMS adsorption was discovered using DFT calculations. Compared to SA-Cu-MXene (1.469 Å) and F-Cu-MXene (1.462 Å), the O—O bond length for C—Cu-MXene (1.476 Å) was extended considerably. This extension implied that PMS molecules might be activated on the C—Cu-MXene surface more successfully than the intrinsic O–O bond length of PMS in a vacuum (1.332 Å). As a result, this improvement promoted the production of reactive oxygen species (ROS) for effective pollutant degradation by facilitating O–O bond cleavage.

Overall, ALD not only introduces well-dispersed active metal centers but also maintains the structural integrity and stability of the MXene substrate. By avoiding harsh chemical treatments, this method minimizes structural collapse and excessive defect formation, preserving both hydrophilicity and surface functional groups essential for catalytic interactions. Therefore, ALD is a strategic tool for functionalizing

MXenes with high catalytic selectivity and controlled electron transfer properties for environmental remediation and oxidative catalysis. Depending on the necessary MXene film characteristics, deposition circumstances, and application requirements, CVD and ALD are both essential methods in advanced catalyst synthesis and surface engineering, providing complimentary advantages. ALD offers unparalleled control at the atomic scale, making it essential for MXene surface chemistry and optimizing catalytic performance in next-generation applications, whereas CVD is preferred for its high throughput and scalability.

2.2.3. Electrodeposition

Electrodeposition involves the electrochemical reduction of metal ions from a precursor solution onto the surface of an electrically conductive substrate, such as MXene. The technique allows for precise control over deposition parameters, including current density, potential, and deposition time, which in turn governs the morphology, crystallinity, and catalytic behavior of the resulting composite. Given MXene's inherent conductivity and surface functionality, it serves as an ideal support for electrodeposited materials in applications such as hydrogen evolution, CO_2 reduction, and selective oxidation.

Guo et al. addressed the pressing need for efficient and stable noble-metal-free oxygen evolution reaction (OER) electrocatalysts capable of operating at industrial-level current densities in alkaline conditions [100]. A $Ti_3C_2T_x$ MXene-based method for creating $Co_2P/Ti_3C_2T_x$, $Fe_2P/Ti_3C_2T_x$, and Co_2P/Fe_2P multiple heterojunctions referred to as CoFe-P@MXene is shown in their work. This process includes low-temperature phosphorization, electrodeposition, and strong electrostatic adsorption. The resultant CoFe-P@MXene takes advantage of MXene's high conductivity and displays a variety of three-dimensional porous formations. Electrochemical testing was performed in a three-electrode arrangement, with a saturated calomel electrode (SCE) acting as the reference electrode, a platinum plate acting as the counter electrode, and a $Ti_3C_2T_x$ MXene/NF composite acting as the working electrode. The electrolyte was composed of 0.1 M CH_3COONa, 1 M NH_4Cl, 0.05 M $FeSO_4{\cdot}7H_2O$, and 0.05 M $Co(NO_3)_2{\cdot}6H_2O$. To create the CoFe@MXene/NF composite, the sample was electrodeposited for 10 min at −1.5 V (vs. SCE) and dried for 6 h at 60 °C, as shown in Fig. 4c.

Experimental findings supported by DFT calculations reveal that the integration of multiple heterojunctions between transition metal phosphides and $Ti_3C_2T_x$ MXene effectively modulates the electronic environment of active Co and Fe sites. This alteration optimizes the adsorption energies of important oxygen-containing intermediates and changes the d-band center, which is necessary for effective oxygen evolution reaction (OER) activity. Superior catalytic performance is facilitated by the designed nanoporous structure, which also improves electrolyte penetration and speeds up product desorption. The CoFe-P@MXene electrocatalyst thus exhibits exceptional OER activity, attaining low overpotentials of 328 mV at 1000 mA cm^{-2} in 1 M KOH and 215 mV at 20 mA cm^{-2}. Additionally, it demonstrates remarkable operational longevity, sustaining consistent performance for 100 h at a current density of 100 mA cm^{-2}, underscoring its promise for alkaline electrolysis applications on an industrial scale.

Importantly, the MXene surface functional groups (–O, –OH, –F) facilitated strong interfacial bonding and the formation of electronic bridges, contributing to enhanced stability and minimized structural defects. This tailored morphology and surface chemistry significantly improved the accessibility of active sites, increased electron transport, and supported the long-term durability of the catalyst under electrochemical conditions. As a result, the electrodeposition method not only optimized the physical and chemical attributes of the MXene-based catalyst but also ensured structural integrity and high activity in catalytic applications.

Overall, the two main categories of MXene catalyst production techniques are top-down and bottom-up, each with unique advantages and disadvantages (Table 1). Top-down methods, such as fluoride salt etching (with HF or safer bifluoride/acid-fluoride salts), are frequently employed because they can create layered, delaminated MXenes with high surface areas and adjustable terminations. Nevertheless, surface pollution and safety issues restrict their scalability. Strong metal–support contacts and homogeneous active site dispersion are made possible by alternatives such as molten salt etching, which combines etching and nanoparticle deposition in a single operation. Although alkaline etching is a more environmentally friendly top-down method for adding hydroxyl functional groups, it has drawbacks in terms of surface passivation and etching depth. High purity and hydrophilicity are provided by electrochemical etching; however, yields are poor and undesirable CDC layers may be produced.

Superior surface engineering and structural control are provided by bottom-up techniques such as CVD, ALD, and electrodeposition. Although CVD is useful for producing consistent MXene films with minimal flaws, its use is constrained by its expense and complexity. ALD is time-consuming and costly, but it is excellent at atomic-scale metal implantation, which is essential for single-atom catalyst creation. The

Table 1
Synthesis methods of MXene-based catalysts.

Synthesis Method	MXenes Used	Advantages	Disadvantages	Methodology	Ref
Molten Salt Etching	Cu_xNi_y/MXene	Simultaneous metal nanoparticle synthesis and etching; improved metal–support interaction; enhanced active site accessibility	Process complexity; high-temperature conditions; limited control over terminal groups	Bimetallic molten salt etching using $CuCl_2$ and $NiCl_2$ to remove Al and deposit CuNi NPs	[62]
Fluoride Salt Etching	$Ti_3C_2T_x$ (ML- and DL-)	Higher surface area; improved active site exposure and terminal groups; effective for environmental applications	Residual fluoride contamination possible; needs careful handling; HF-related safety concerns	Acid/fluoride salt or bifluoride etching followed by delamination for morphology tuning	[63]
Alkali Etching	h-TC/TAC (Hydroxylated Ti_3C_2)	HF-free; greener synthesis; generates hydroxyl groups; enhances substrate activation; highly efficient desulfurization	Limited etching depth; potential passivation by oxide/hydroxide layers; slower kinetics	Alkaline solution etching under water-assisted heating to produce hydroxylated surfaces	[64]
Electrochemical Etching	$Ti_3C_2T_x$	Highly controlled; clean surface terminations; improved hydrophilicity and dispersion; suitable for aqueous catalysis	Low yield due to CDC co-formation; needs optimization for large scale	Electrochemical etching using NaCl/HCl/NH_4Cl under controlled voltage to remove Al	[65]
Chemical Vapor Deposition	Mo_2C	High purity films; fewer defects; controlled morphologies and orientations; good conductivity and stability	Costly setup; limited material versatility; potential C-contamination from CH_4 source	Thermal CVD using CH_4 precursor and Mo on Cu foil to form Mo_2C crystals	[98]
Atomic Layer Deposition	Cu-MXene	Atomic precision; control over metal distribution; enhances O–O bond activation and ROS generation	Slow deposition rates; high-cost instrumentation; limited to thin film or SA applications	Cycle-controlled ALD of Cu in SA, cluster, and film forms on MXene surface	[99]
Electrodeposition	CoFe-P@MXene	Strong metal–support interaction; porous structure; stable under industrial OER conditions	Requires electrode compatibility; multi-step process; metal precursor and electrolyte sensitive	Electrodeposition of Co and Fe precursors onto MXene with phosphorization step	[100]

versatility of electrodeposition, its gentle processing conditions, and its capacity to create strong heterostructures with high catalytic activity and long-term stability make it stand out among them. Molten salt etching is the most effective technique overall when performance and practicalities are taken into account. It balances structural integration, catalytic activity, and customizable surface chemistry, particularly for high-performing bimetallic MXene-based materials.

3. Physicochemical characterization of MXene-Based catalysts

A thorough understanding of the physicochemical properties of MXene-based catalysts is essential for their rational design and performance optimization. These properties encompassing structural, chemical, and electronic features are typically investigated using a suite of advanced characterization techniques. These methods provide critical insights into composition, morphology, surface functionality, and defect structures, all of which influence catalytic behavior. Understanding these aspects is vital not only for correlating catalyst structure with activity and selectivity but also for guiding the development of more efficient catalytic systems. This section explores the principal analytical approaches used to probe the complex nature of MXene-based catalysts, with a particular emphasis on structure–property relationships.

3.1. Structural characterization

Structural characterization is a critical component of understanding the physicochemical nature of MXene-based catalysts. Techniques such as XRD, Raman spectroscopy, and TEM are employed to probe the crystallinity, layered morphology, and atomic-scale architecture of MXenes. These analyses are essential for confirming successful MXene synthesis, revealing structural transformations resulting from functionalization or treatment, and identifying features that may influence catalytic performance, such as interlayer spacing, defects, or edge sites. By mapping these structural attributes, researchers can draw meaningful correlations between material structure and reactivity in catalytic applications.

3.1.1. X-ray diffraction

X-ray Diffraction (XRD) is a fundamental characterization technique for analyzing the structural properties of MXene-based catalysts. It offers crucial information about structural integrity, interlayer spacing, phase composition, and crystallinity, which are vital for understanding their catalytic activity. XRD is especially helpful in monitoring changes brought about by synthesis techniques, surface alterations, and intercalation processes because of the distinct layered structure of MXenes. Specific MXene phases may be identified, oxidation byproducts can be found, and structural stability under reaction conditions can be assessed thanks to the distinctive diffraction peaks. A shift in the (002) diffraction peak, for example, indicates changes in interlayer spacing due to the removal of Al layers or the incorporation of terminal functional groups (e.g., –OH, –F, –O), which can directly affect the material's surface chemistry and catalytic reactivity. Furthermore, peak broadening or the presence of additional phases may reveal structural defects or incomplete etching, which impact both the conductivity and stability of MXene-based catalysts.

Salma et al. conducted an experiment on the degradation of Congo red (CR) dye in water using microwave-induced reaction technology for the formation of 2D $Ti_3C_2T_x$ MXene for this purpose [106]. They investigated the phase structure and crystallinity of the produced 2D $Ti_3C_2T_x$ MXene as well as the precursor $Ti_3C_2T_x$ MAX phase by utilizing XRD analysis (Fig. 5). According to their investigation, 99 % of a 25 ppm CR dye solution was efficiently destroyed in just 6 min by 50 mg of the synthesized 2D $Ti_3C_2T_x$ MXene. The catalyst also showed outstanding stability, allowing for up to five cycles of reuse without compromising degrading efficiency. They used scavengers such as benzoquinone, Na-EDTA, and isopropyl alcohol to identify the active species participating in the process in order to comprehend the degradation mechanism. They refined the degradation parameters using a response surface approach analysis and found that a CR dye concentration of 29.07 ppm and 35.30 mg of 2D $Ti_3C_2T_x$ MXene may result in the highest deterioration. This study demonstrates the possibility of 2D $Ti_3C_2T_x$ MXene as a productive and reusable catalyst for the quick breakdown of CR dye caused by microwaves.

Sharp diffraction peaks in the $Ti_3C_2T_x$ MAX phase's XRD pattern verified its high phase purity and crystallinity. A notable alteration was noted following the etching procedure and the creation of 2D $Ti_3C_2T_x$ MXene: the distinctive sharp peak of the MAX phase at 39° almost disappeared. This disappearance confirms the development of the 2D-layered $Ti_3C_2T_x$ MXene and shows that the aluminum (Al) layers were successfully removed from the $Ti_3C_2T_x$ MAX phase [107–110]. The structural change from MAX to MXene is crucial because the elimination of Al improves surface reactivity and accessibility by increasing the exposure of catalytically active Ti sites and enabling greater interlayer spacing. On the other hand, structural flaws or reduced catalytic effectiveness may result from partial Al removal or remaining dopants. However, trace carbon (C) residues from the initial carbide layers can potentially affect the MXene surface's electrical structure. These carbon residues can function as inert barriers that impede active sites or as conductive bridges that improve charge transfer, depending on whether they are graphitic, amorphous, or linked. These leftover elements can also be beneficial if handled appropriately.

The MXene sheets can occasionally be stabilized by carbon residues, enhancing structural integrity and avoiding layer collapse during cycling. Additionally, surface terminations are introduced during the

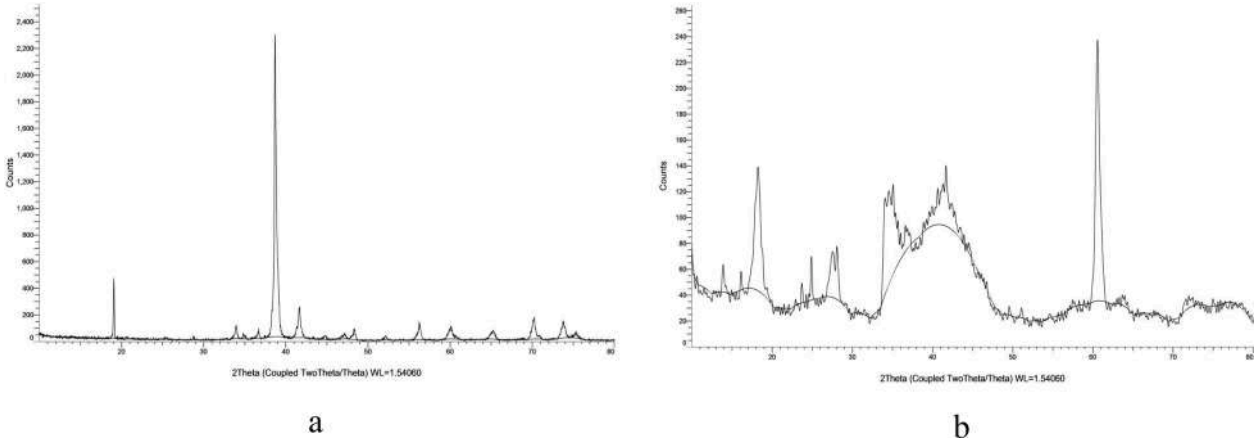


Fig. 5. XRD patterns of (a) Ti_3AlC_2 MAX and (b) 2D $Ti_3C_2T_x$ MXene. Reproduced with permission from Ref. [106].

dopant removal process, and these are known to affect adsorption behavior and catalytic activity. The distribution of surface charges and their interaction with reactants are changed by the presence or lack of these functionalities, which are partially determined by how well dopants like Al are etched. Therefore, regulated carbon content can improve electrical conductivity and reusability, even though good Al removal is required for optimal MXene production. In conclusion, modifying MXene catalytic performance requires optimizing both the removal of Al dopants and the management of residual carbon, particularly in applications such as advanced oxidation processes and environmental remediation.

3.1.2. Raman spectroscopy

Raman spectroscopy is a powerful tool for investigating the structural and electronic properties of MXene-based catalysts. Understanding catalytic performance requires knowledge of bond vibrations, phase composition, surface functionalization, and defect structures, all of which are crucially revealed by this approach. These characteristics are closely linked to surface reactivity, hydrophilicity, and chemical stability all of which govern catalytic efficiency. For instance, the presence and intensity of characteristic D and G bands can be used to assess the degree of disorder and the density of defects in the MXene lattice. Functional groups revealed by Raman shifts can also indicate potential anchoring sites for metal nanoparticles or reaction intermediates, influencing catalytic selectivity and durability under reactive environments.

The work of Kao et al. presents a fresh approach to improving electrochemical water splitting, an essential step in the manufacture of sustainable hydrogen [111]. Moreover, their research tackles the drawbacks of conventional catalysts, including the low conductivity of metal oxides and metal-organic frameworks (MOFs) and the high cost of noble metals. They created a trimetallic oxide/MXene composite by fusing MOFs and MXenes in a novel heterostructure to get around these obstacles. They examined the carbon structure of their produced materials using Raman spectroscopy (Fig. 6). Specifically, they utilized a copper(II) benzene-1,3,5-tricarboxylate (Cu-BTC) precursor, which was transformed into NiCoCu-BTC. This MOF, when integrated with MXene and subjected to carbonization, produced the BTC—NiCoCuO/MXene heterostructure. This innovative catalyst demonstrated exceptional electrocatalytic performance, achieving overpotentials of 227 mV for the oxygen evolution reaction (OER) and 164 mV for the hydrogen evolution reaction (HER) at a current density of 10 mA cm^{-2}.

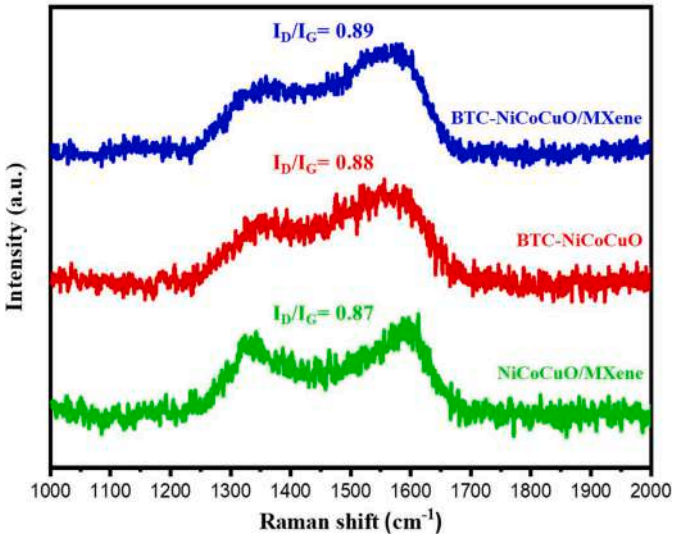


Fig. 6. Raman spectra of NiCoCuO/MXene, BTC—NiCoCuO and BTC—NiCoCuO/MXene. Reproduced with permission from Ref. [111].

They were paying particular attention to the disordered carbon (D band) and graphitic carbon (G band) linkages located at 1350 and 1582 cm^{-1}, respectively [112]. They assessed the degree of graphitization by measuring the intensity ratio (ID/IG) of these bands, noting that a lower ratio denotes a more organized, graphitic structure. According to their findings, which are displayed in Fig. 8, the ID/IG ratios of the BTC—NiCoCuO/MXene, BTC—NiCoCuO, and NiCoCuO/MXene samples were extremely close (0.89, 0.88, and 0.87, respectively), indicating that the three materials had similar levels of graphitization [113–116]. Their results demonstrate the great promise of this MOF-MXene heterostructure technique for creating affordable, high-performing catalysts for the production of sustainable hydrogen.

3.1.3. Transmission electron microscopy

Transmission electron microscopy (TEM) is a crucial technique for investigating the nanoscale morphology, structural features, and atomic-scale composition of MXene-based catalysts. Layer stacking, edge structures, and surface flaws are revealed by high-resolution imaging, all of which have a direct impact on catalytic activity. Additionally, TEM makes it possible to analyze particle size, dispersion, and interactions with support materials, providing important information about the stability and functionality of catalysts. Characterizing lattice fringes, elemental distribution, and oxidation states is further aided by sophisticated methods like energy-dispersive X-ray spectroscopy (EDS) and high-resolution TEM (HRTEM) [117,118]. Moreover, electron diffraction patterns acquired via selected area electron diffraction (SAED) can validate crystallinity and identify any phase transformations. Such detailed morphological analysis ensures that the catalyst retains a high density of accessible active sites, which is vital for optimal catalytic performance.

According to the work of Zhang et al. [119], Mo_2TiC_2 MXene, a novel 2D material characterized by its exceptional electrical conductivity, has been successfully synthesized and explored for applications in supercapacitors, lithium batteries, and electrocatalysis. Additionally, they emphasized Mo_2TiC_2 MXene's significant potential in photocatalytic processes, citing its advantageous light absorption and electron-accepting properties as the reason. As a result, they used etching and intercalation procedures to develop and create a few-layered Mo_2TiC_2 MXene with a huge lamellar structure. A $ZnIn_2S_4/Mo_2TiC_2$ binary composite that was tightly bonded was then created by an in situ solvothermal technique. With 10 mg of catalyst, the ideal $ZnIn_2S_4$/10 % Mo_2TiC_2 composite demonstrated an impressive photocatalytic hydrogen evolution (PHE) rate of 4.3 mmol g^{-1} h^{-1} under simulated sunshine irradiation. This rate exceeded the activity of $ZnIn_2S_4$ with 1 % Pt as a co-catalyst and was 3.8 times greater than that of pure $ZnIn_2S_4$. The superior activity of few-layered Mo_2TiC_2 MXene as a noble-metal-free co-catalyst was successfully proven by Zhang et al.'s study. Additionally, they stressed that the produced MXene's massive lamellar structure makes it a perfect substrate for additional semiconductor integration, allowing for the creation of high-performance MXene-based heterostructures.

The morphological and structural characteristics of the Mo_2TiC_2 MXene and the $ZnIn_2S_4/Mo_2TiC_2$ composite were the main focus of their thorough characterization. Many stacked nanosheets made up the enormous lamellar structure of the original Mo_2TiC_2 (M-Mo_2TiC_2). The resulting Mo_2TiC_2 showed a comparable big lamellar morphology after intercalation and delamination, but with fewer stacked nanosheets, which was thought to be beneficial for its intimate integration with $ZnIn_2S_4$ (Fig. 7a). The successful creation of a few-layered structure was confirmed by atomic force microscopy (AFM) analysis, which showed a considerable drop in thickness from over 100 nm for M-Mo_2TiC_2 to less than 1.80 nm for the few-layered Mo_2TiC_2 nanosheets [120]. In accordance with earlier observations, high-resolution transmission electron microscopy (HRTEM) revealed a lattice spacing of 0.24 nm, which corresponds to the (011) crystal plane of Mo_2TiC_2 as shown in Fig. 7b-c [121]. Aggregated nanosheets gave Pristine $ZnIn_2S_4$ its microsphere-like

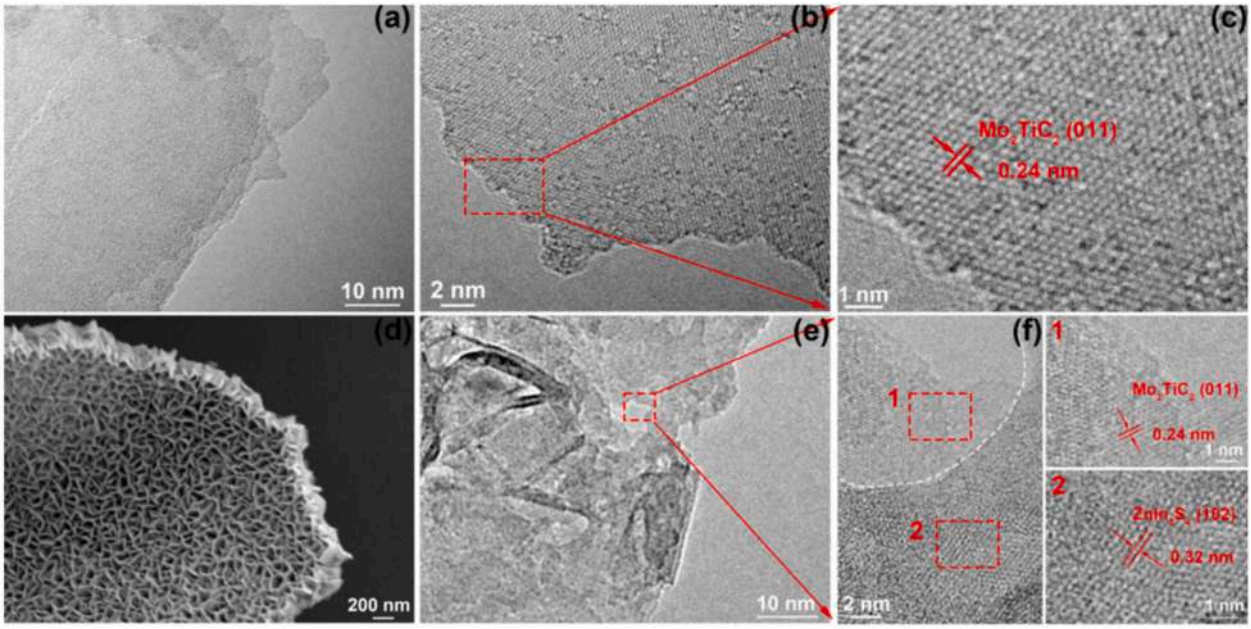


Fig. 7. TEM image (a), HRTEM image (b) and enlarged HRTEM image (c) of Mo_2TiC_2, SEM image (d), TEM image (e) and HRTEM image (f) of $ZnIn_2S_4$/50 % Mo_2TiC_2, the marked 1, 2 rectangles represent Mo_2TiC_2 and $ZnIn_2S_4$. Reproduced with permission from Ref. [119].

shape. $ZnIn_2S_4$ nanosheets were found to grow uniformly on the surface of Mo_2TiC_2 nanosheets in the $ZnIn_2S_4$/50 % Mo_2TiC_2 composite, forming a tightly bound interface and a closely integrated hierarchical structure, as depicted in Fig. 7d-e. It was anticipated that this interface would improve charge transfer efficiency and shorten charge transfer distances. As shown in Fig. 7f, with lattice distances of 0.24 nm and 0.32 nm, respectively, corresponding to the (011) plane of Mo_2TiC_2 and the (102) plane of $ZnIn_2S_4$, additional HRTEM analysis verified a distinct boundary between $ZnIn_2S_4$ and Mo_2TiC_2 in the composite, further confirming the tightly bound interface within the manufactured binary composite.

3.2. *Surface and chemical state characterization*

A comprehensive evaluation of the surface chemistry and electronic structure of MXene-based catalysts is crucial for understanding their performance in catalytic reactions. Advanced techniques such as XPS, FTIR, and *in situ*/Operando spectroscopic methods are employed to probe elemental distribution, oxidation states, surface terminations, and chemical interactions. These surface-sensitive analyses reveal the presence and transformation of functional groups, track the evolution of catalytic sites, and monitor the adsorption and desorption of intermediates under reaction conditions. By identifying the influence of surface defects, dopants, or modifications, these methods offer essential insights into the structure–activity relationships and guide the rational design of high-performance MXene-based catalysts.

3.2.1. *X-ray photoelectron spectroscopy*

X-ray Photoelectron Spectroscopy (XPS) is a powerful technique for analyzing the chemical states of surface elements and functional groups. It offers a greater understanding of catalyst activation and stability by providing useful information on elemental composition, surface flaws, and oxidation states. XPS also reveals the presence and proportion of surface terminations (–OH, –F, –O), which impact surface acidity/basicity, electronic conductivity, and interactions with reactants or deposited metal nanoparticles. Moreover, shifts in binding energy can indicate charge transfer between the MXene support and active species, offering insight into catalyst-support synergy. An extensive study by Nugroho et al. examined how an external magnetic field affected the photocatalytic activity of Ti_3C_2 MXene/GQDs@ZnO, specifically with regard to drug degradation [122]. The relationship between magnetic fields and MXene-based photocatalysts is still poorly understood, despite the growing interest in these systems. Their study used Ti_3C_2 MXene/GQDs@ZnO as a catalyst to investigate the photomagnetocatalytic (PMC) degradation of ibuprofen and amoxicillin in aqueous solutions.

The surface chemistry of Ti_3C_2 MXene/GQDs@ZnO was thoroughly revealed by their XPS investigation. Fig. 8a uses the doublet spectral lines of Zn 2p at binding energies of 1021.7 eV (Zn $2p_{3/2}$) and 1044.8 eV (Zn $2p_{1/2}$) to demonstrate the presence of Zn^{2+} in ZnO [123,124]. These findings are consistent with earlier ZnO research. Fig. 8b displays the high-resolution spectra of O 1 s, which show two distinctive peaks at 531.0 eV and 531.9 eV, which represent C–O–C and C–O bonding, respectively [125,126].

The oxidation states of titanium in MXene are suggested by the deconvolution of the Ti2p spectrum in Fig. 8c, which shows the presence of Ti $2p_{3/2}$ and Ti $2p_{1/2}$ at 463.4 and 457.9 eV, respectively, with an area ratio near 2:1 [14,127]. Additionally, the C1s spectra is shown in Fig. 8d, where two different peaks at 283.3 and 284.2 eV, respectively, represent C–C/–CH bonds and C=C bonds [128]. The XPS data clearly show that the components in the Ti_3C_2 MXene/GQDs@ZnO composite have changed chemical states. Well-defined doublet peaks in the Zn 2p spectrum, which correspond to Zn $2p_{3/2}$ and Zn $2p_{1/2}$, respectively, demonstrated the structural and chemical stability of ZnO in the composite and confirmed that zinc is still in the Zn^{2+} oxidation state. Two separate peaks were found in the O 1 s area, which were ascribed to C–O–C and C–O bonds, respectively. These signals, which represent surface chemical changes, indicate the addition of functional groups including oxygen from GQDs or partially oxidized MXene. The existence of titanium in mixed oxidation states (Ti^{3+}/Ti^{4+}) was indicated by the characteristic peaks in the Ti 2p spectrum, which had a constant 2:1 area ratio. This alteration implies that the Ti_3C_2 MXene layers underwent partial surface oxidation either during production or during photocatalytic activity. Lastly, the coexistence of graphitic domains and aliphatic carbon species introduced through GQDs is indicated by the C 1 s spectrum, which corresponds to C–C/–CH and C=C bonds, respectively. The customized interfacial chemistry and electrical environment, which are essential for increasing photocatalytic activity, are reflected in all of these observed shifts and chemical changes.

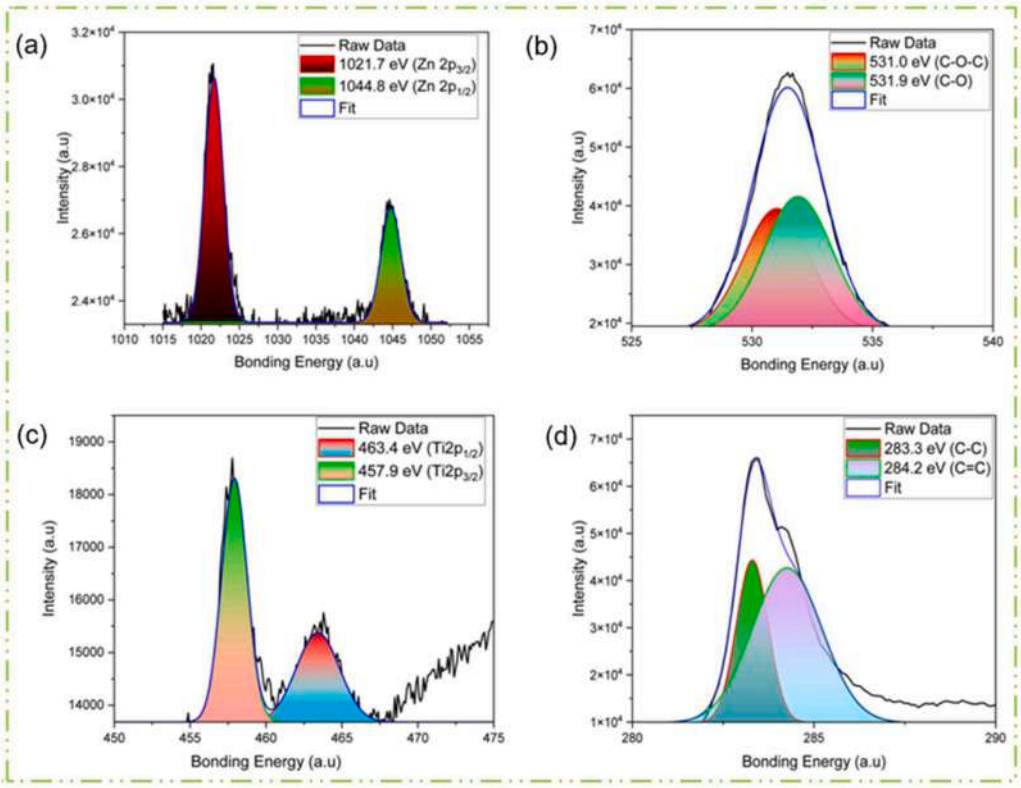


Fig. 8. XPS spectra of (a) Zn2p (b) O1s, (c) Ti2p, and (d) C1s. Reproduced with permission from Ref. [122].

The study looked at important reaction parameters to maximize PMC degradation, including pH, pollutant concentration, catalyst loading, and voltage variation. Significant durability and reusability were demonstrated by the Ti_3C_2 MXene/GQDs@ZnO catalyst, which had remarkable degradation efficiencies of 99 % for amoxicillin and 97 % for ibuprofen. These results open the door for more research into photo-magnetocatalytic processes in environmental remediation by highlighting the potential of MXene-based catalysts for sophisticated wastewater treatment applications, especially when exposed to an external magnetic field.

3.2.2. Fourier transform infrared spectroscopy

Key interactions between active sites and reactant molecules can be identified by using Fourier Transform Infrared Spectroscopy (FTIR), which is used to detect functional groups and surface bonding. The nature of adsorption processes and the function of surface functionalities in catalytic reactions are both clarified by this method. In catalytic reactions, FTIR can track intermediate species and bonding configurations during adsorbate-surface interactions. For example, peaks corresponding to C=O, –OH, or adsorbed CO_2 can help deduce how effectively MXenes activate reactants. This understanding is pivotal for optimizing active site composition and designing more selective and efficient catalytic pathways.

The photocatalytic performance of g-C_3N_4 is significantly hindered by severe charge recombination due to its s-triazine unit structure. Therefore, attaining high-efficiency photocatalysis requires enhancing the separation and transfer of photogenerated carriers. In their work, Nie et al. created a sophisticated BiOI/g-C_3N_4 p-n heterojunction photocatalyst coated with MXene quantum dots (MQDs) [45]. By combining the powerful electron-withdrawing capability of MQDs with the internal electric field (IEF) of the BiOI/g-C_3N_4 heterojunction, this composite structure improves charge separation and transfer. Furthermore, light absorption and reactive site availability are greatly enhanced by the addition of BiOI, which has a narrow bandgap, and MQDs, which have a wide surface area and many active sites. Consequently, the ternary g-C_3N_4/MQDs/BiOI photocatalyst shows a noteworthy 42.23 % NO removal efficiency with decreased NO_2 byproduct generation. Trapping experiments and in situ Fourier Transform Infrared (FTIR) spectroscopy were used to investigate the photocatalytic mechanism, offering fresh perspectives on charge separation improvement techniques for g-C_3N_4-based photocatalysts.

FTIR spectroscopy investigations were carried out to learn more about the interface interactions within the g-C_3N_4/MQDs/BiOI heterojunction. The s-triazine ring units of g-C_3N_4 are represented by a

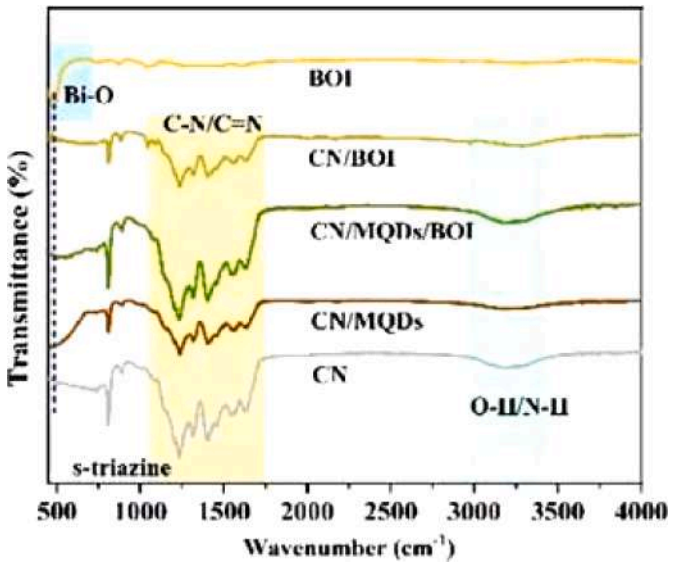


Fig. 9. FTIR spectroscopy of all prepared photocatalysts. Reproduced with permission from Ref. [45].

distinctive band at 808 cm^{-1} in the FTIR spectrum (Fig. 9). Furthermore, C–N/C=N and O–H/N–H stretching vibrations are responsible for two significant absorption zones between 1010 and 1720 cm^{-1} and 2930 and 3500 cm^{-1}, respectively [129]. The successful integration of BiOI into the heterostructure is further confirmed by the presence of Bi-O vibrations at 485 cm^{-1}, which are linked to BOI [130]. The CN/MQDs and CN/MQDs/BOI composites notably retain the distinctive vibrational bands of both CN and BOI, suggesting a stable combination of CN with BOI and MQDs. However, there are no noticeable vibrational bands that match MQDs, most likely because the strong CN interactions block their signals [131]. Furthermore, the inorganic character of the composite, which has little effect on the functional groups of CN, is responsible for the faint BOI peaks in the material [132,133].

A crucial finding is that, in comparison to pristine CN, all composites exhibit minor changes in the distinctive CN vibrational modes [134]. The g-C_3N_4/MQDs/BiOI heterojunction appears to have close interfacial contacts, which are essential for improved charge transfer and separation, according to these spectrum changes. In order to maximize the performance of MXene-based photocatalysts for cutting-edge environmental applications, the results support the significance of heterojunction generation and co-catalyst decoration.

In Fig. 10, the mechanism of CO_2 photoreduction was investigated by tracking reaction intermediates through in-situ FTIR spectroscopy over the CN/MQDs/BOI photocatalyst. A number of spectral bands appeared and grew stronger with the addition of CO_2 and H_2O, signifying the development and buildup of chemical intermediates.

Bicarbonates (HCO_3^-) and formate (COO^-) species are represented by the peaks at 1361 cm^{-1}, 1526 cm^{-1}, and 1561 cm^{-1}, which indicate that CO_2 was first activated at the photocatalyst surface [135,136]. Further supporting the chemical adsorption of CO_2 onto the photocatalyst are bands that emerge at 1385 cm^{-1}, 1459 cm^{-1}, 1656 cm^{-1}, and 1700 cm^{-1} and are attributable to different carbonate (CO_3^{2-}) species [137,138]. The presence of these intermediates without light suggests that CO_2 experiences initial surface activation in the absence of light, which makes subsequent photocatalytic reduction easier (Fig. 10a).

The CN/MQDs/BOI photocatalyst exhibits a number of additional peaks at roughly 1249 cm^{-1}, 1447 cm^{-1}, 1638 cm^{-1}, 1672 cm^{-1}, 1720 cm^{-1}, and 1779 cm^{-1} when exposed to simulated sunshine after achieving adsorption-desorption equilibrium (Fig. 10b). Prolonged lighting causes these peaks to become more intense, suggesting that they are involved in the photocatalytic activity [139]. The generation of HCO_3^- is represented by the bands at 1249 cm^{-1}, 1367 cm^{-1}, 1638 cm^{-1}, and 1672 cm^{-1}, whilst CO_3^{2-} species are responsible for the peaks at 1384 cm^{-1} and 1447 cm^{-1}. Furthermore, *COOH, a crucial step in the conversion of CO_2, is linked to the peaks at 1720 and 1779 cm^{-1}. It reaches saturation as a result of the balance between its production and consumption. Additionally, COO^- species strongly adsorb onto the photocatalyst surface, as seen by peaks at 1526 cm^{-1} and 1561 cm^{-1}. The conversion of CO_2 into intermediates, which are thereafter transformed into CO and CH_4, is confirmed by the notable increase in the intensities of HCO_3^-, *COOH, and COO^-. Thus, this pathway is probably the main mechanism for CO_2 photoreduction to CO: CO_2 gas is first adsorbed onto the surface of the photocatalyst, where it is activated to create CO_3^{2-} and HCO_3^- species. These intermediates eventually convert CO_2 into CO by reacting with photogenerated charge carriers when exposed to light.

s. *Catalytic performance evaluation*

To effectively understand and optimize the catalytic performance of MXene-based materials, a comprehensive set of physicochemical characterization techniques is essential. These methods provide critical insights into the surface chemistry, redox behavior, and interaction

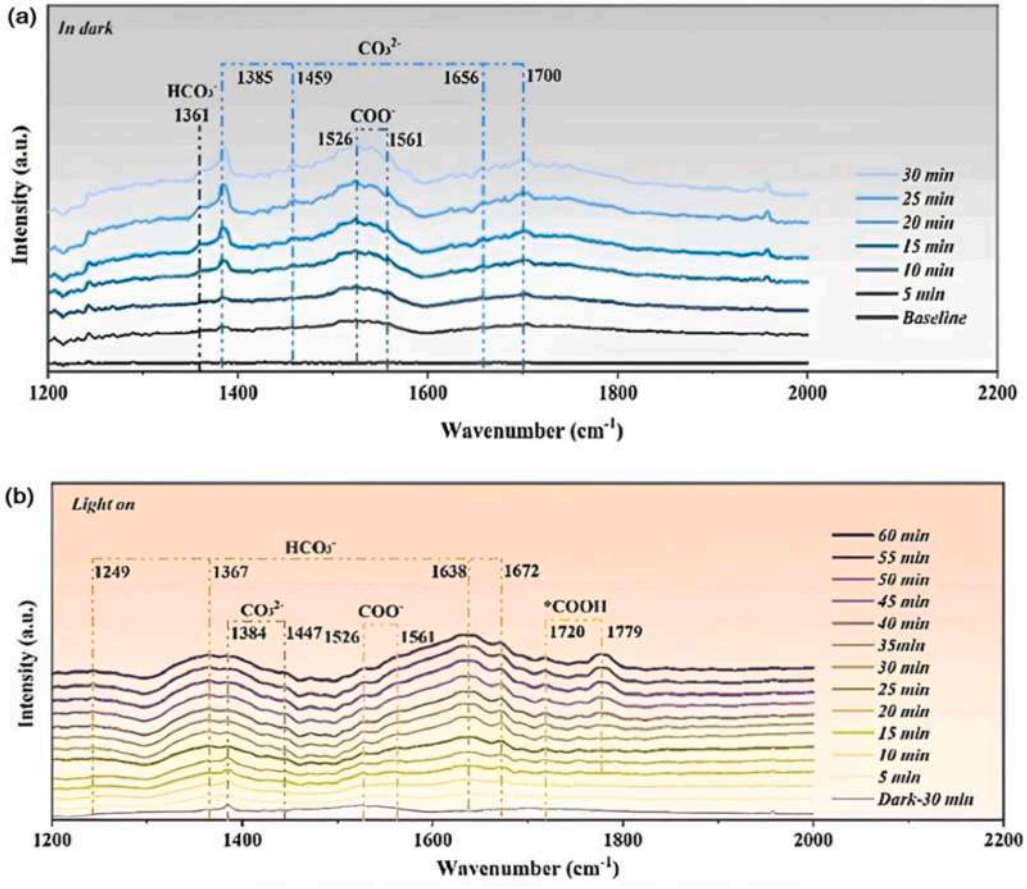


Fig. 10. CO_2 photoreduction in-situ FTIR spectra (a) in the dark and (b) in the presence of light. Reproduced with permission from Ref. [45].

mechanisms of the catalysts under relevant reaction conditions. By probing the ability of MXenes to facilitate reactant activation, sustain redox cycles, and undergo structural changes during catalysis, these analyses form the basis for correlating material properties with catalytic efficiency. The following subsections highlight key techniques employed in the evaluation of MXenes' catalytic functionalities.

3.3.1. Temperature-programmed desorption

Temperature-programmed desorption (TPD) is a powerful technique used to investigate the adsorption and desorption behavior of molecules on the surface of MXene catalysts. TPD offers important insights into the quantity and kind of surface interactions, the number of active sites, and the thermal stability of adsorbed intermediates by tracking the desorption of adsorbed species as a function of temperature. Understanding how reactants attach to and are released from the MXene surface, which has a direct impact on catalytic activity, requires the use of this approach. To assess surface acidity, NH_3-TPD (ammonia temperature-programmed desorption) was specifically employed, providing a detailed evaluation of acid site density and strength on MXene surfaces. This technique was instrumental in analyzing how zinc incorporation influenced the acidic properties of the catalysts.

CoZnyB/Nb_2CT_x catalysts' catalytic efficiency is greatly influenced by their surface acidity, especially when it comes to the selective hydrogenation of cinnamonaldehyde (CAL) to cinnamonyl alcohol (COL). Although they have low intrinsic activity, amorphous cobalt boride (CoB) catalysts have strong $C = O$ selectivity. According to Shi et al.'s work, CoZnyB/Nb_2CT_x catalysts with different Zn contents ($y = 0$, 0.025, 0.05, 0.075, and 0.1) were created using a wet reduction technique in order to improve their performance [140]. Their research showed that by altering surface acid characteristics and increasing active site exposure, Zn inclusion greatly enhanced catalytic efficiency. With a 91.4 % CAL conversion and a 66.3 % COL yield, $CoZn_{0.05}B/Nb_2CT_x$ demonstrated the greatest low-temperature performance among the produced catalysts.

Through NH_3-TPD tests, the impact of Zn on surface acidity was examined; the outcomes are shown in Fig. 11. The thermal stability of the CoZnyB/Nb_2CT_x catalysts was verified by TG-DSC analysis prior to these tests. The TG curve of $CoZn_{0.05}B/Nb_2CT_x$, as illustrated in Fig. 12, may be divided into three phases: the removal of MXene surface groups (150–400 °C), the desorption of H_2O (30–140 °C), and a phase change of Nb_2CT_x that takes place at about 720 °C, as indicated by a weak compensating peak in the DSC curve [141]. These results indicate that the CoZnyB/Nb_2CT_x catalysts' surface acid sites are responsible for the NH_3-TPD peaks below 700 °C.

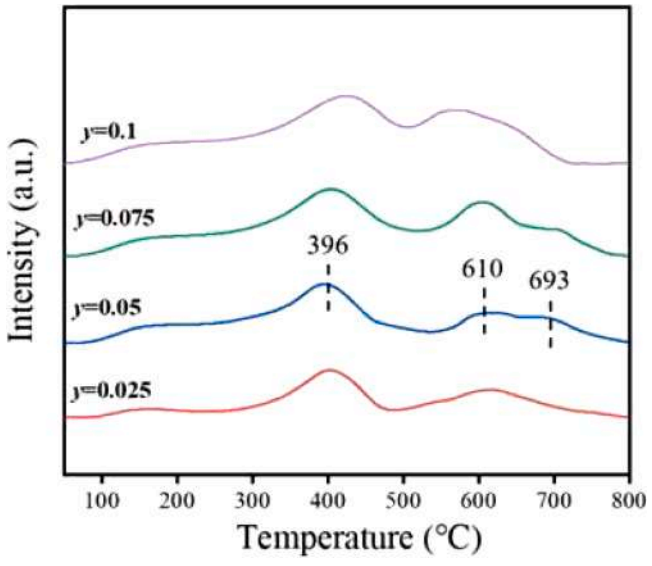


Fig. 11. NH_3-TPD profiles of $CoZn_{0.05}B/Nb_2CT_x$ and CoB/Nb_2CT_x. Reproduced with permission from Ref. [140].

According to earlier research, acid sites can be categorized into three regions based on their quantity and strength: weak acid sites are located in Region I (below 300 °C), medium-strength acid sites are located in Region II (between 300 and 500 °C), and strong acid sites are located above 500 °C [142]. Three peaks can be seen in the CoB/Nb_2CT_x NH_3-TPD profiles at 92 °C, 529 °C, and 800 °C (Fig. 13). The medium-strength acid site at 529 °C is caused by the OH and F groups on the Nb_2CT_x surface, whereas the peak at 92 °C is associated with weak acid sites that are contributed by CoB [143,144]. The thermal breakdown of Nb_2CT_x is linked to the high-temperature peak of about 800 °C. On the other hand, the CoZnyB/Nb_2CT_x catalysts' NH_3-TPD spectra show two strong peaks at 396 °C and 610 °C in addition to a smaller peak at 693 °C. Because of the development of CoZnyB species and their interaction with Nb_2CT_x, the medium-strength acid sites indicate that Zn inclusion changes the acidity of CoB/Nb_2CT_x.

Based on the NH_3-TPD results, the total acid site concentration in CoB/Nb_2CT_x and $CoZn_{0.05}B/Nb_2CT_x$ was computed and is shown in Table 2. With an increase in Zn concentration, the acidity of CoZnyB/Nb_2CT_x catalysts rose from 0.24 mmol/g to 0.81 mmol/g. This improvement implies that Zn either works as an extra acid site contributor or encourages the exposure of already-existing acid sites, changing the surface characteristics of CoB catalysts. By concurrently increasing surface acidity and active site exposure, these results shed light on how zinc contributes to increased catalytic activity and, ultimately, better CAL hydrogenation efficacy.

3.3.2. Temperature-programmed reduction

Temperature-programmed reduction (TPR) is a crucial technique for characterizing the redox properties of MXene-based catalysts, providing valuable insights into the reducibility of metal species supported on the MXene surface and the nature of metal-support interactions. It is critical to comprehend how easily metal oxides or other reducible species can be reduced in the context of catalysis since this directly affects the activity and selectivity of the catalyst. In H_2-TPR, the catalyst is heated in a reducing environment (usually H_2/Ar) while the hydrogen consumption is tracked. With peak positions and intensities revealing details about the strength of metal-oxygen interactions, the dispersion of metal species, and the development of different metal phases, the resulting profile, also known as the TPR spectrum, shows the temperatures at which reduction events take place. Because of their distinct layered structure and capacity to accommodate a wide range of metal species, MXene-based catalysts benefit greatly from this method, which enables the tuning of catalytic performance through customized redox characteristics.

Traditional hydrodeoxygenation (HDO) catalysts often suffer from low activity and susceptibility to deactivation. To address these limitations, Wang and his colleagues developed a range of MXene-supported Ni-M (M = Pd, Pt, Ru) bimetallic catalysts in order to overcome these constraints [144]. Under ideal circumstances, the Ni-Pd/MXene catalyst produced a 35.15 % total yield of HDO products and 100 % guaiacol conversion, demonstrating better catalytic performance among them. Its high specific surface area, low acidity, and robust three-electron transfer channels between the active and support metals were credited with this improved performance. As explained below, the metal reducibility and the interaction between the support and active metals were characterized using the H_2-TPR method in order to understand the catalytic mechanism better.

The reduction peaks of Ni species in the H_2-TPR curves of all catalysts may be deconvoluted into three different regions, as illustrated in Fig. 14, which is suggestive of different Ni-support interactions [145]. Firstly, 'free' Ni species are reduced, showing limited interactions with the MXene support, with a low-temperature reduction peak in the 300–500 °C range. Second, the decrease of Ni species with moderate support interactions is shown in a medium-temperature reduction peak

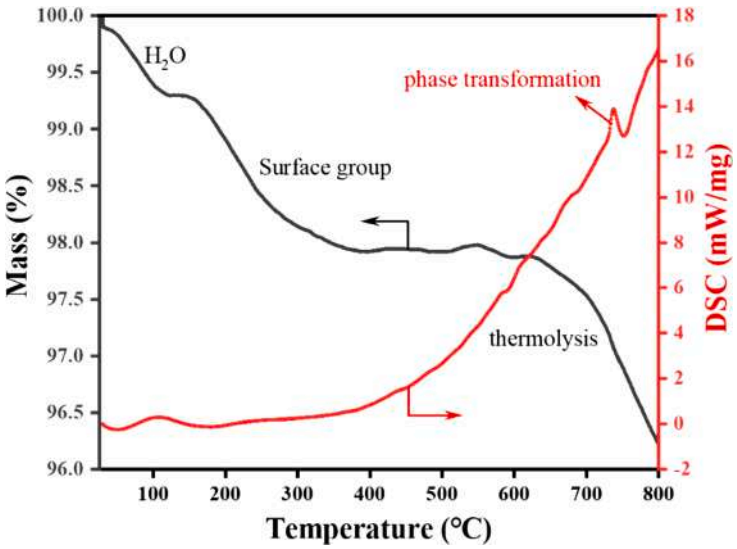


Fig. 12. TG-DSC profiles of $CoZn_{0.05}B/Nb_2CT_x$. Reproduced with permission from Ref. [140].

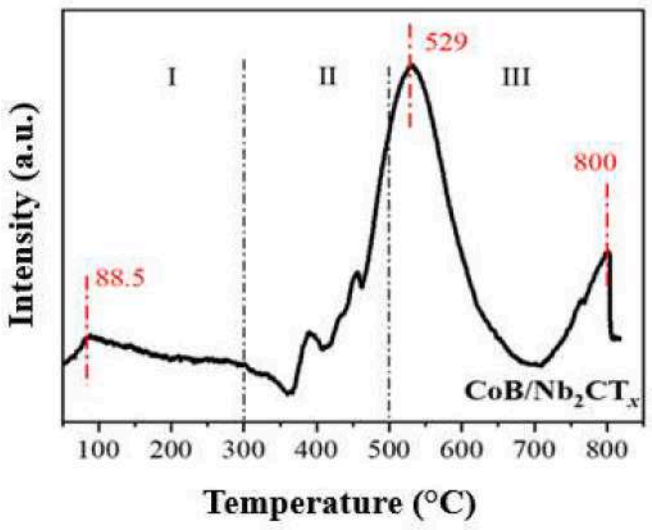


Fig. 13. NH_3-TPD profiles of CoB/Nb_2CT_x catalyst. Reproduced with permission from Ref. [140].

Table 2
The quantity of acid sites from NH_3-TPD profiles.

Catalysts	Acidity (mmol/g)
$CoZn_{0.025}B/Nb_2CT_x$	0.24
$CoZn_{0.05}B/Nb_2CT_x$	0.36
$CoZn_{0.075}B/Nb_2CT_x$	0.48
$CoZn_{0.1}B/Nb_2CT_x$	0.81
spent $CoZn_{0.05}B/Nb_2CT_x$	0.31
CoB/Nb_2CT_x	0.68

that ranges from 500 to 700 °C. Last but not least, the reduction of a Ni-Ti-O_x solid solution is responsible for a high-temperature reduction peak at about 810 °C. This finding is consistent with earlier studies, including one by Gao et al. [146], which showed that for Ni/TiP, Ni/ZrP, and Ni/NbP catalysts, reduction peaks in the 775–800 °C range correlated to the reduction of Ni-O-Ti, Ni-O-Zr, and Ni-O-Nb solid solutions, respectively.

Notably, the Ni component and the MXene support interact more strongly in Ni-Pd/MXene, as evidenced by the more prominent high-temperature reduction peak of Ni in comparison to the other catalysts [147]. Additionally, notable variations in the center temperatures of the Ni species' low- and medium-temperature reduction peaks across the catalysts imply that the noble metals (Pd, Pt, and Ru) have a major impact on Ni reducibility. In particular, Ni-Pd/MXene has a slightly lower Ni reduction temperature than Ni-Pt/MXene in the low-temperature region, whereas Ni-Ru/MXene does not exhibit a discernible reduction peak. The Ni reduction peak temperature in Ni-Pd/MXene is approximately 520 °C in the medium-temperature range, which is lower than that of the other catalysts.

The overall lower reduction peak temperatures of Ni species in Ni-Pd/MXene suggest that Pd effectively facilitates hydrogen adsorption, dissociation, and transfer to NiO, thereby enhancing NiO reduction. This demonstrates that Pd and Ni have a strong synergistic effect [148]. Further demonstrating the intricate redox behavior of these bimetallic MXene catalysts are low-temperature reduction peaks in the H_2-TPR curves of Ni-Pd/MXene, Ni-Pt/MXene, and Ni-Ru/MXene, respectively, at 143.7, 199.5, and 63.9 °C. These peaks are ascribed to the reduction of Pd, Pt, and Ru oxide particles. This thorough H_2-TPR research confirms Wang et al.'s suggested "relay catalytic" theory and adds to their findings, strengthening our knowledge of Ni-Pd/MXene's improved catalytic performance in HDO processes.

3.3.3. *In situ/operando spectroscopic techniques*

Operando and in situ, spectroscopic techniques are indispensable for unraveling the intricate mechanisms governing catalytic reactions on MXene-based materials. Operando and in situ techniques allow for the real-time monitoring of structural and chemical changes during reaction circumstances, in contrast to conventional ex-situ characterization, which offers a static image of the catalyst [149]. Understanding the development of active sites, the creation of reaction intermediates, and how reaction parameters affect catalytic performance all depend on this dynamic approach. These methods provide a thorough understanding of the catalytic process by concurrently examining the structure and activity of the catalyst, enabling researchers to link certain reaction pathways to observable phenomena. When used in situ or operando, methods like diffuse reflectance infrared Fourier transform spectroscopy (DRIFTS) and X-ray absorption spectroscopy (XAS) offer vital information about the dynamic behavior of MXene-based catalysts, which helps to create more effective and selective catalytic systems [150,151].

Through *in-situ* synthesis, Li et al. combined ZIF-67 with $Ti_3C_2T_x$ MXene to increase its photocatalytic efficiency, maximizing activity by adjusting the MXene concentration [152]. The ZIF-67/$Ti_3C_2T_x$ MXene

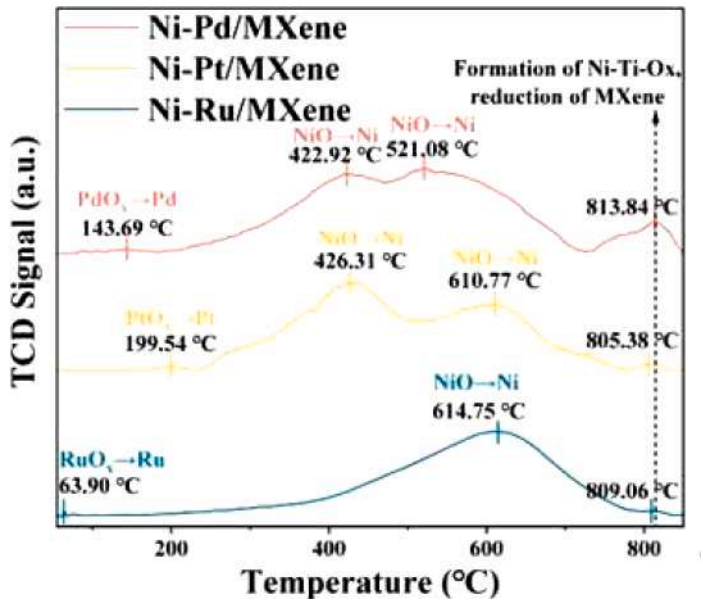


Fig. 14. H_2-TPR profiles of Ni-Pd/MXene, Ni-Pt/MXene and Ni-Ru/MXene bimetallic catalysts. Reproduced with permission from Ref. [144].

composite that was produced, known as ZT-450, showed noticeably better performance, producing CO, CH_4, and H_2 at 62.7, 6.7, and 7.3 μmol g^{-1}, respectively. Notably, ZT-450 produced CO at a rate 4.8 times higher than $Ti_3C_2T_x$ and 16.1 times higher than pure ZIF-67. Additionally, $Ti_3C_2T_x$ improved CO_2 adsorption, reaching 127.90 μmol g^{-1}, which was significantly higher than that of individual components. They demonstrated that $Ti_3C_2T_x$ promotes quick electron transport, boosts CO_2 activation, and improves light absorption in the ZIF-67 matrix using DFT calculations.

As seen in Fig. 15a-b, ZIF-67 and ZT-450 underwent *in-situ* DRIFTS testing to determine the reaction intermediates during photocatalytic CO_2RR. Light irradiation was started after CO_2 and H_2O had been darkly adsorbed for 30 min. The adsorption and activation of CO_2 were indicated by the distinctive peaks corresponding to bicarbonate (HCO^{3-}at 1541 cm^{-1}), monodentate carbonate (m-CO_3^{2-}at 1506 and 1339 cm^{-1}), and bidentate carbonate (b-CO_3^{2-}at 1557 and 1473 cm^{-1}) for both pure ZIF-67 and ZT-450. Furthermore, the presence of adsorbed H_2O was confirmed by a signal at 1651 cm^{-1}.

Importantly, both surfaces showed the COOH absorption peak at 1636 cm^{-1}, which is a crucial step in the reduction of CO_2 to CO or CH_4. Nevertheless, ZT-450′s *COOH peak intensity was noticeably higher than ZIF-67′s, indicating the improved CO_2 reduction capacity following $Ti_3C_2T_x$ inclusion. In addition to *COOH, ZT-450 showed peaks at 1195, 1067, and 1417 cm−1 that corresponded to the *CHO, *OCH_3, and *CH_3 groups, respectively. ZIF-67 was unable to produce CH_4 during CO_2RR, which is consistent with the absence of these intermediates linked to CH_4 formation. This finding emphasizes how crucial $Ti_3C_2T_x$ is for improving the usage of photogenerated carriers and providing enough electrons for CO protonation to CH_4.

Furthermore, a CO absorption peak at 2075 cm^{-1} was observed, with ZT-450 showing a higher peak intensity than ZIF-67, reflecting the enhanced CO production. As the light exposure period increased, the CO adsorption strength on ZT-450 first increased and subsequently dropped, suggesting partial CO conversion. At the same time, the *CHO, *OCH_3, and *CH_3 peaks' rising intensities with light exposure time indicated that some CO had been converted to CH_4. The activity trends in photocatalytic CO_2 reduction, where ZT-450 demonstrated superior CO and CH_4 production, are consistent with these results. In addition to facilitating higher CO intermediate generation and desorption, adding $Ti_3C_2T_x$ to ZT-450 accelerates the protonation of some CO intermediates to *CHO, *OCH_3, and eventually CH_4. This in-situ DRIFTS investigation offers a thorough mechanistic insight into the improved photocatalytic CO_2RR performance of the ZIF-67/$Ti_3C_2T_x$ MXene composite.

4. Applications of MXene-based catalysts in sustainable energy production

MXene-based catalysts have been actively explored for their

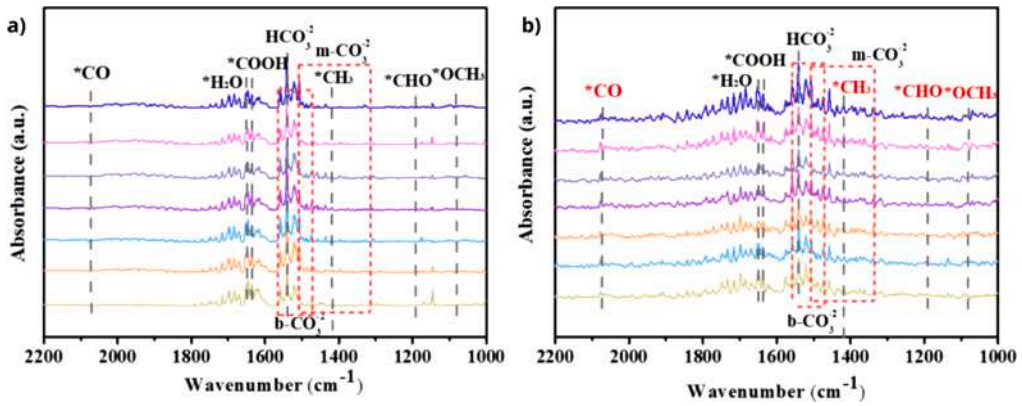


Fig. 15. Detected reaction intermediates in photocatalytic CO_2RR over ZIF-67 and ZT-450 by in-situ DRIFTS. Reproduced with permission from Ref. [152].

applicability across several key processes in sustainable energy production, particularly in the Fischer–Tropsch (FT) synthesis, CO_2 hydrogenation to methane (CH_4), and electrochemical water splitting via the hydrogen evolution reaction (HER). MXene-supported catalysts in the FT process allow synthesis gas, which is a combination of CO and H_2, to be converted into long-chain hydrocarbons, which helps produce synthetic fuels with less need for fossil fuels. They are appropriate for improving selectivity toward heavier hydrocarbon fractions (C_{5+}) due to their exceptional capacity to anchor and disseminate active metals as well as their adjustable surface chemistry. Similarly, MXene-based materials offer effective platforms for activating both CO_2 and H_2 in the catalytic hydrogenation of CO_2 to CH_4 under comparatively mild circumstances, and some MXene-metal composites exhibit excellent activity and stability. The generated CH_4 can be used as a renewable fuel or added to the natural gas infrastructure that already exists, facilitating the recycling and storage of carbon. Because of their high electrical conductivity, layered structure, and functional surface terminations that promote proton adsorption and hydrogen generation, MXene-based catalysts have shown exceptional performance in the HER in electrochemical water splitting. In the shift to a low-carbon energy system, these three energy pathways - CO_2 conversion to methane, hydrocarbon fuel synthesis via FT, and green hydrogen production - are complementary pillars, and MXene catalysts play an increasingly central role in improving their efficiency, selectivity, and operational stability.

4.1. Fischer-Tropsch synthesis (FTS)

The Fischer−Tropsch (FT) process has been a cornerstone in synthetic fuel production for nearly a century, facilitating the hydrogenation of carbon monoxide (CO) into hydrocarbons and oxygenates [153]. In FT synthesis, syngas are often obtained from biomass, natural gas, or coal, and catalyst selection determines product selectivity. Because of their high activity and selectivity, transition metals like iron (Fe) and cobalt (Co) are the mainstay of industrial FT catalysts [154–158]. The goal of alternative catalyst development in recent years, however, has been to improve the chain-length distribution of FT products, especially in the C_{10}–C_{20} hydrocarbon range, which is essential for the synthesis of diesel fuel [159,160].

Early transition metal carbides (TMCs), particularly Mo_2C, have drawn more attention in this context as possible FT catalysts [161]. With a chain growth probability coefficient (α) of 0.3–0.4, unsupported Mo_2C catalysts, such as cubic α-MoC_{1-x} and orthorhombic β-Mo_2C phases, mainly produce methane, CO_2, lower alkanes, and alkenes [162–164]. Furthermore, Mo_2C catalysts are selective for alcohols, especially C_{2+} alcohols [165,166]. Mo_2C's selectivity for alcohol synthesis has been improved using a number of techniques, such as distributing Mo_2C onto supports like Al_2O_3 or TiO_2 and alkali metal promotion (such as potassium doping) [167–169].

Model catalyst complexes with clearly defined surfaces and structures are essential for enhancing our comprehension of Mo_2C catalysis because they enable accurate spectroscopic characterization. 2D Mo_2C catalysts (Mo_2CT_x) generated from MXene have become attractive model systems in this regard [170–173]. Mo_2CT_x MXenes allow for the fine-tuning of catalytic characteristics through the tunable partial or complete reductive defunctionalization of surface termination groups (O, OH, and F). Additionally, Mo_2CT_x MXenes have a well-defined basal surface structure and good thermal stability (~550−600 °C in multilayered nanoplatelet morphology), which makes them perfect platforms for connecting computational modelling and mechanistic investigations with actual catalysis [174,175].

Recent research by Kountoupi et al. has shown that the coverage of surface passivating groups (T_x, such as O, OH, and F) directly affects the catalytic activity of Mo_2CT_x in FT synthesis [47]. Interestingly, under FT conditions, a significant increase in CO conversion results from a decrease in T_x species, especially surface-bound oxygen (O*). The strong activation of Mo_2CT_x pretreatment in H_2 at 400 °C, which markedly increased syngas conversion efficiency, served as proof of this. Because controlled defunctionalization of MXene-derived Mo_2C structures can open up novel catalytic routes, these findings emphasize the significance of surface changes in Mo_2C catalysis. These insights provide a strong foundation for further optimizing Mo_2C-based catalysts for selective FT transformations, particularly in oxygenate conversion and hydrocarbon chain growth.

Significant carbon vacancies are not produced when Mo_2CT_x is pretreated with H_2 at 400 °C. However, the remaining Tx passivating groups are removed in situ without the concurrent creation of carbon vacancies when Mo_2CT_x−400 is exposed to FT reaction conditions. Therefore, upon in situ activation, the active state of Mo_2CT_x−400 can be defined as 2D-Mo_2C, while the active state of Mo_2CT_x−500 is better represented as 2D-Mo_2C_{1-x} (Fig. 16). These results demonstrate how important it is to use optimum reductive surface defunctionalization techniques in order to fully utilize the catalytic potential of materials obtained from Mo_2CT_x for FT synthesis. In the next part, we describe the most likely FT reaction route and utilize DFT calculations to explain the selectivity trends seen for 2D-Mo_2C.

The basic steps of FTS mechanism are depicted in this schematic over a 2D-Mo_2C catalyst surface (Scheme 3). It shows the progressive hydrogenation and C–C coupling reactions that lead from CO dissociation to the creation of ethane (C_2H_6). The dissociation of adsorbed CO* into C* and O* first releases CO_2 and produces reactive surface carbon. The surface carbon undergoes sequential hydrogenation to produce CH*, CH_2*, and CH_3* intermediates, which subsequently undergo C–C coupling processes. Through insertion and hydrogenation, these intermediates gradually create longer hydrocarbon chains, giving rise to species such as CCH_3*, $CHCH_3$*, and CH_2CH_3*, before desorbing as ethane (CH_3CH_3(g)). The stabilization of transition states and adsorbed intermediates on the Mo_2C surface in each step highlights the catalyst's function in facilitating the formation of carbon chains through regulated hydrogenation and bond activation.

The prepared Mo_2C-based catalysts' Fischer–Tropsch (FT) performance was assessed at 330 °C, 25 bar, H_2:CO = 2:1, and a weight hourly space velocity (WHSV) of 5.1 $L\cdot(g_{cat}\cdot h)^{-1}$. With a low CO conversion of only 2 %, the β-Mo_2C(400) catalyst demonstrated a CO consumption rate of 1.3 mmol $CO\cdot gcat^{-1}\cdot h^{-1}$ (Fig. 17a). The partial selectivities to CH_4, C_2–C_4 alkanes, C_2–C_4 alkenes, and C_5+ alkanes were 52 %, 23 %, 13 %, and 12 %, respectively, but the selectivity to CO_2 was 15 %. There were no discernible levels of liquid hydrocarbons.

The Mo_2CT_x−500 catalyst, on the other hand, demonstrated an initial CO conversion of 94 % that held steady for 20 h while in operation (Fig. 17b). However, rather than being an effective FT catalyst, this material primarily served as a methanation catalyst. Selectivity to CO_2 was 48 %, and the product distribution was composed of 61 % CH_4, 37 % C_2–C_4, and 2 % C_{5+} alkanes, respectively. In contrast to β-Mo_2C(400), no appreciable levels of liquid hydrocarbons or olefins (>0.5 %) were found.

An initial CO conversion of 12 % was noted for the Mo_2CT_x−400 catalyst, however over time, an impressive in situ activation took place (Fig. 17c). The conversion rose to 88 % after eight hours on stream and stayed there throughout the entire experiment (20 h TOS). Similar to Mo_2CT_x−500, the selectivity to CO_2 was 50 %; however, there was a notable shift in the distribution of hydrocarbons. The percentages of CH_4, C_2–C_4, and C_{5+} alkanes that were partially selected were 25 %, 20 %, and 55 %, respectively. The dynamic evolution of Mo_2CT_x−400 under reaction conditions is highlighted by this transition, which results in a more favorable distribution of FT products with increased selectivity for long-chain hydrocarbons (C_{5+}).

Overall, under stable Fischer-Tropsch (FT) conditions, 2D Mo_2C produces heavier hydrocarbons (C_{5+} alkanes), with a selectivity of 55 %. The α value of 0.87 for these alkanes, which extend into the kerosene range, is roughly double that of three-dimensional (3D) Mo_2C catalysts. In comparison to a reference β-Mo_2C catalyst that does not activate at the same FT circumstances, the production rate of C_{5+} hydrocarbons from

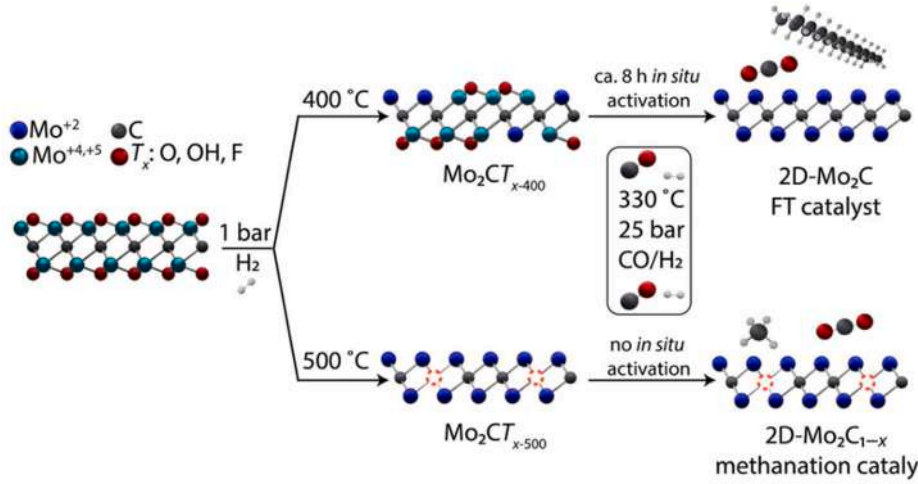
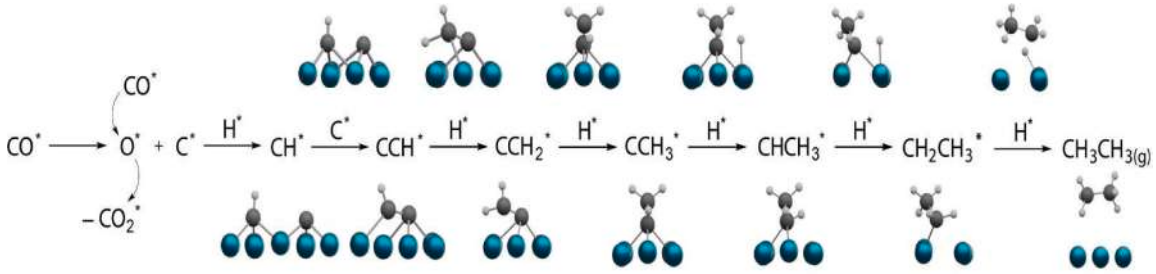


Fig. 16. Likely routes of reductive defunctionalization of Mo_2CT_x in H_2 and under FT conditions, and implications for FT selectivity. Reproduced with permission under terms of CC-BY license from Ref. [47].



Scheme 3. Key Steps of the Calculated Reaction Mechanism on 2D-Mo_2C with Selected Transition States and Intermediates. Reproduced with permission under terms of CC-BY license from Ref. [47].

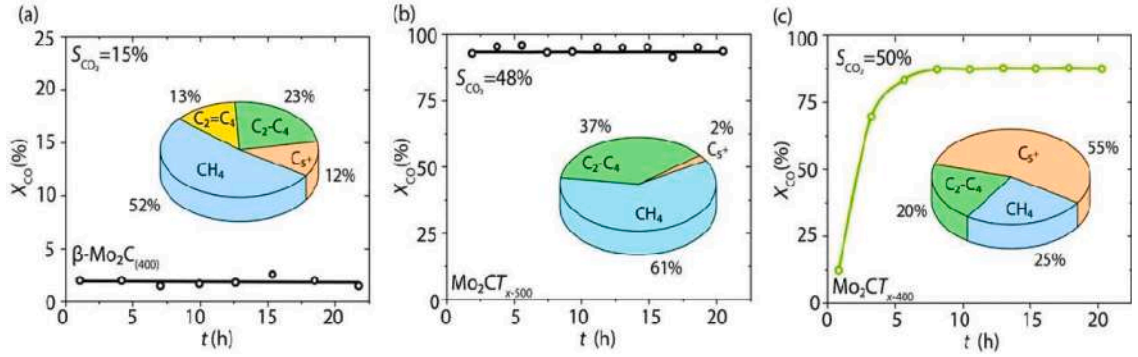


Fig. 17. CO conversion as a function of time on stream (TOS) for (a) β-Mo_2C(400), (b) Mo_2CT_x−500, and (c) Mo_2CT_x−400 during Fischer–Tropsch (FT) synthesis. The insets illustrate the gas-phase product distribution at steady-state conditions, corresponding to CO conversions of 2 %, 94 %, and 88 %, respectively. Reproduced with permission under terms of CC-BY license from Ref. [47].

2D-Mo_2C is approximately 100 times higher. According to DFT calculations, the remarkable selectivity of 2D-Mo_2C towards C_{5+}alkanes is caused by a larger energy barrier for hydrogenating surface alkyl molecules than the barrier for carbon-carbon coupling. The rate-limiting step in the FT reaction over 2D-Mo_2C is the elimination of oxygen (O*). The substantial CO_2 selectivity (about 50 %) that has been seen is consistent with O* being preferentially removed as carbon dioxide (CO_2) as opposed to water (H_2O). The reason for the lack of additional carbon-oxygenates is that straight dissociation of carbon monoxide (CO) is energetically preferable to dissociation aided by hydrogen.

4.2. *Methane production by CO_2 hydrogenation*

Photocatalysis is a highly effective approach for CO_2 conversion, utilizing only light and water to generate various solar fuels. A crucial element of this procedure involves the meticulous selection of photocatalysts according to their physicochemical characteristics [176]. Many transition metal oxide semiconductors, such as TiO_2, g-C_3N_4, ZnO, WO_3, $BiVO_4$, CdS, Fe_2O_3, Cu_2O, $CdIn_2S_4$, $CsPbBr_3$, and Bi_2WO_6, have been thoroughly studied because of their advantageous properties, such as non-toxicity and thermal stability [177–179]. However, the majority of single-component photocatalysts have low efficiency because of poor selectivity, limited UV spectrum activity, and rapid charge

recombination, which makes their practical use difficult [180,181]. By substituting co-catalysts for noble metals, Madi et al. explored the creation of heterostructure photocatalysts, a difficult undertaking intended to improve the effective separation and transmission of photo-induced electrons and holes [182]. For photocatalytic CO_2 reduction to greener fuels, they specifically investigated a well-designed 2D V_2C MXene cocatalyst-assisted $LaCoO_3$ perovskite-based g-C_3N_4 composite. A new cocatalyst called V_2C MXene showed great promise in establishing close contact with the $LaCoO_3$/g-C_3N_4 heterojunction, allowing for improved charge carrier separation and increased visible light absorption. Selectivities of 34 % and 66 % were achieved with the improved $LaCoO_3$/g-C_3N_4/V_2C heterojunction, resulting in CH_4 and CO yield rates of 332 and 171 μmol g^{-1} h^{-1}, respectively. The 15 % V_2C/g-C_3N_4 photocatalyst generates more CH_4 and CO than $LaCoO_3$, g-C_3N_4, and a 15 % $LaCoO_3$/g-C_3N_4photocatalyst, as shown in Fig. 18a. $LaCoO_3$, g-C_3N_4, and their composites were found to convert CO_2 to CO efficiently. The V_2C/g-C_3N_4 nanocomposite, on the other hand, particularly increases CH_4 synthesis. In comparison to the V_2C/g-C_3N_4 composite, the rapid recombination of photoexcited charges on pure g-C_3N_4 and $LaCoO_3$ results in poor CO_2 reduction and reduced CH_4 yields.

Under visible light, MXene-based composites, such as 15 % V_2C/g-C_3N_4, encourage the production of methane in a single step [183]. Because 2D porous g-C_3N_4 and 2D V_2C work in concert, the 2D/2D V_2C/g-C_3N_4 photocatalyst produces the most methane. This facilitates the conversion of CO_2 to CO and CH_4 by slowing recombination and providing various electron routes. The composite efficiently produces protons and electrons, increasing the generation of methane in the presence of visible light. The intimate interaction between 2D V_2C and 2D porous g-C_3N_4 nanosheets is responsible for the increased photoactivity. Additionally, charge separation is improved by the Schottky barrier that forms at the MXene/semiconductor contact, which functions as an electron sink. Additionally, 2D V_2C MXene functions as a 2D substrate for semiconductor development and a reservoir for charges.

The ternary $LaCoO_3$/g-C_3N_4/V_2C catalyst demonstrates the highest photocatalytic performance for the formation of CH_4 and CO, as illustrated in Fig. 18b The maximum efficiency of CO_2 methanation is shown by this compound. This composite's V_2C/g-C_3N_4 heterojunction enhances electron transport from g-C_3N_4 to V_2C. Under visible light, 2D V_2C functions as an electron acceptor, promoting charge separation and CO_2 activation, which results in the generation of CH_4 and CO. As illustrated in Fig. 18c-d, the effect of V_2C loading on $LaCoO_3$/g-C_3N_4 was examined. Surprisingly, a 15 % V_2C loading reduced CH_4 and CO

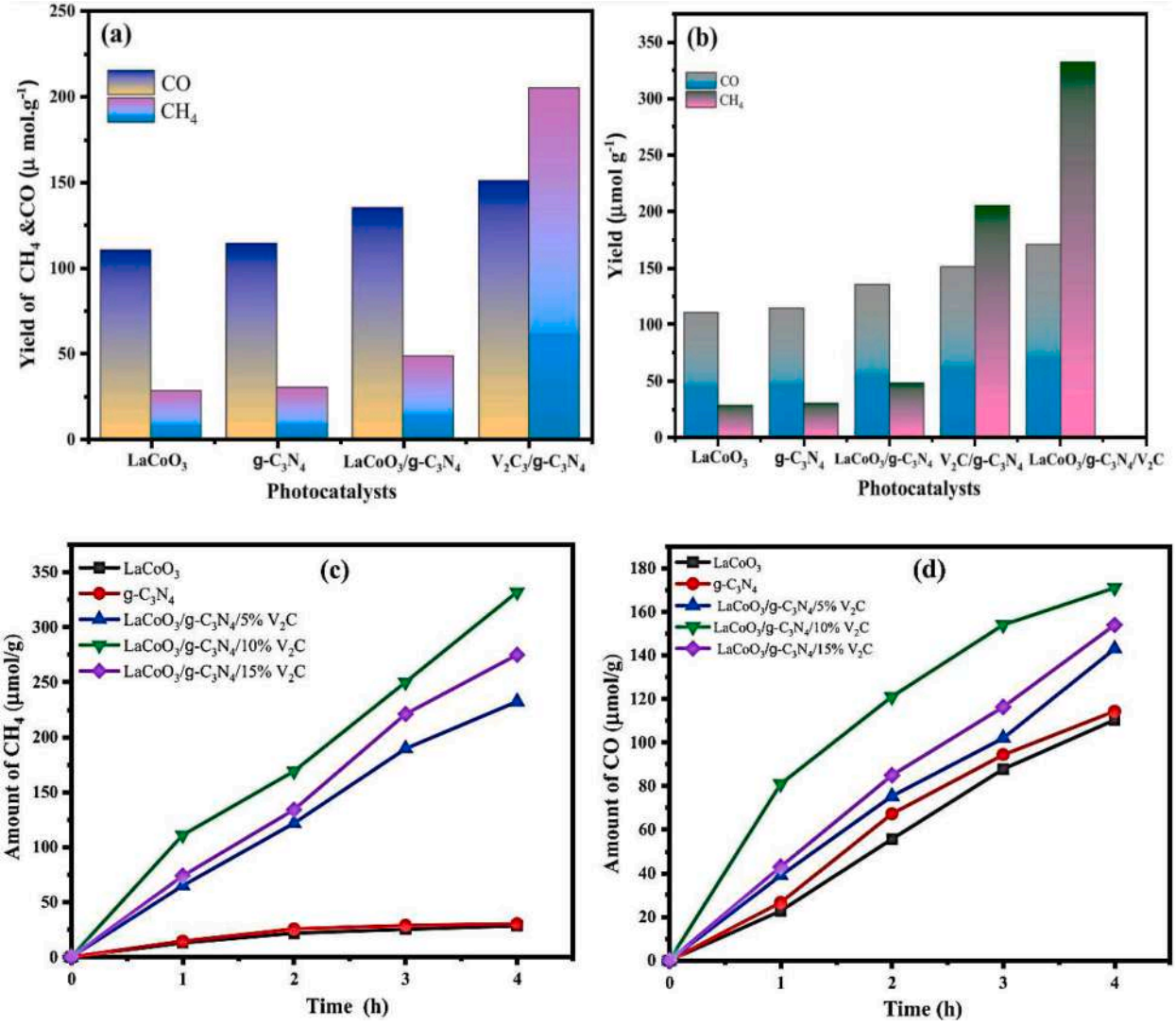


Fig. 18. (a) Performance analysis of $LaCoO_3$, g-C_3N_4, $LaCoO_3$/g-C_3N_4, and V_2C/g-C_3N_4 for the production of CHg-C_3N_4 and CO via photocatalysis COg-C_3N_4 conversion within visible light range; (b) Performance analysis of LaCoOg-C_3N_4, g-C_3N_4, $LaCoO_3$/g-C_3N_4, V_2C/g-C_3N_4, and $LaCoO_3$/g-C_3N_4/V_2Cto produce CHg-C_3N_4 and CO via photocatalytic COg-C_3N_4conversion in presence of visible light; The product of (c) CHg-C_3N_4 and (d) CO production over $LaCoO_3$, g-C_3N_4, 15 % $LaCoO_3$/g-C_3N_4/5 %V_2C, 15 %$LaCoO_3$/g-C_3N_4/10 %V_2C, and 15 % $LaCoO_3$/g-C_3N_4/15 %V_2C. Reproduced with permission from Ref. [182].

generation compared to varying V_2C loading (5 %, 10 %, and 15 %) with a fixed 15 wt % LaCoO3 loading. This is probably because too much V_2C creates shielding and more charge recombination centers, which prevent reactants from reaching active sites and lessen light scattering. Consequently, for effective charge separation and improved CO_2 conversion, an ideal V_2C loading is essential.

The suggested photocatalytic mechanism is depicted in Fig. 19. According to experimental findings, CO and CHg-C_3N_4 could be produced by pure $LaCoO_3$ and g-C_3N_4. However, the development of a $LaCoO_3$/g-C_3N_4 composite improved the performance of these materials. Likewise, combining 2D V_2C and 2D g-C_3N_4 nanotextures produced encouraging outcomes. This knowledge facilitates comprehension of the charge transfer and separation pathways as well as photoactivity. In accordance with earlier research, the band gaps for g-C_3N_4 and $LaCoO_3$ were found to be 2.86 eV and 1.51 eV, respectively [184]. However, a Z-scheme heterojunction was not supported by $LaCoO_3$'s lower conduction band (CB) (−0.62 eV) and lower valence band (VB) (+0.88 eV) in comparison to g-C_3N_4's CB (−1.38 eV) and VB (+1.48 eV). Consequently, a type 1 heterojunction in the $LaCoO_3$/g-C_3N_4 composite, where V_2C acts as a cocatalyst to trap and transport photoinduced charge carriers, is responsible for the increased efficiency.

Overall, the improved rate of CO_2 attachment over the V_2C-assisted nanotexture was responsible for the maximum CO and CH_4 generation rates, which were often attained at a pressure of 0.4 bar. H_2 exhibited the highest photoactivity among the hydrogen sacrificial reagents, methanol, and water. Because the CO_2 methanation reaction involved effective charge carrier formation, CH_4 production was 1.33 times higher with H_2 than with water. The conclusion was that V_2C MXene is a promising cocatalyst that can be utilized to replace noble metals. It is also appropriate for photocatalytic CO_2 reduction in solar fuels and other solar energy applications.

4.3. Hydrogen production via electrochemical water-splitting

The production of high-purity hydrogen in an emission-free, eco-friendly manner is made possible by electrochemical water splitting [185,186]. In recent decades, materials based on noble metals, such as Pt, Ru, Ir, and Pd, have been thought to be the best electrocatalysts for cathodic and anodic half-reactions. However, their extensive industrial application is still limited because of their poor durability, high cost, and scarcity [187–189]. Significant strides have been achieved in creating affordable, environmentally friendly substitutes for traditional noble metal-based catalysts that provide competitive catalytic activity, increased durability, and greater scalability in order to overcome these obstacles. Within MXene-derived NiV oxycarbide nanospheres (NiPt@NVOC), Tran et al. report a very porous electrocatalyst made of NiPt nanostructures with ultra-low Pt loading (1.22 wt %) and tunable surface-confined Pt charge sites [190]. In order to efficiently lower the water dissociation energy barrier and improve intermediate adsorption for efficient hydrogen production, this special structural and morphological design, in conjunction with an optimized electrical configuration, encourages the exposure of negatively charged Pt active centers.

The Gibbs free energy graphs in Fig. 20 show how water dissociation works thermodynamically. The reaction ($^*H_2O \rightarrow H + OH$) is endothermic on NVOC (+1.32 eV) but thermodynamically exothermic on NiPt (−0.04 eV), Ni@NVOC (−0.50 eV), and NiPt@NVOC (−0.67 eV). This suggests that the kinetics of water dissociation into adsorbed hydrogen (H) intermediates favor NiPt@NVOC. Additionally, NiPt@NVOC has superior performance in alkaline hydrogen evolution reaction (HER) kinetics, as evidenced by its ideal Gibbs free adsorption energy of hydrogen intermediates (ΔG_H) compared to the other materials. ΔG_{H^*} is an important metric for assessing catalyst activity in the acidic HER process, which includes proton (H^+) adsorption, H* production, and H_2 desorption.

The NiPt@NVOC material is a suitable electrocatalyst for the hydrogen evolution process (HER) in acidic environments because, as Fig. 21a illustrates, its $|\Delta G_H|$ value of 0.08 eV is closer to zero than that of NiPt (0.11 eV), Ni@NVOC (0.63 eV), and NVOC (0.8 eV). When $|\Delta G_H|$ was computed for each possible site in order to identify the active sites, Pt was shown to be the most advantageous (0.08 eV), followed by Ni in

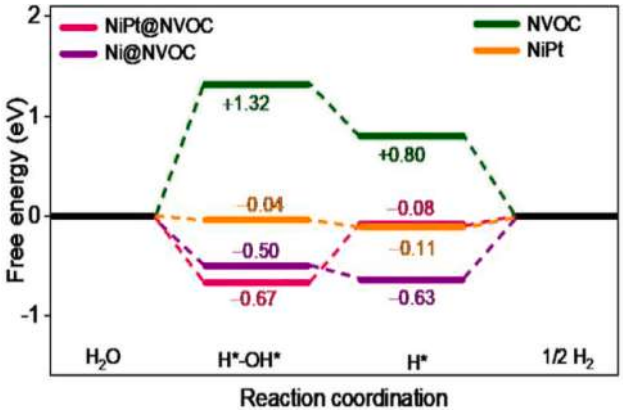


Fig. 20. Gibbs free energy diagram of NiPt, NVOC, Ni@NVOC, and NiPt@NVOC for the HER reaction in alkaline conditions. Reproduced with permission from Ref. [190].

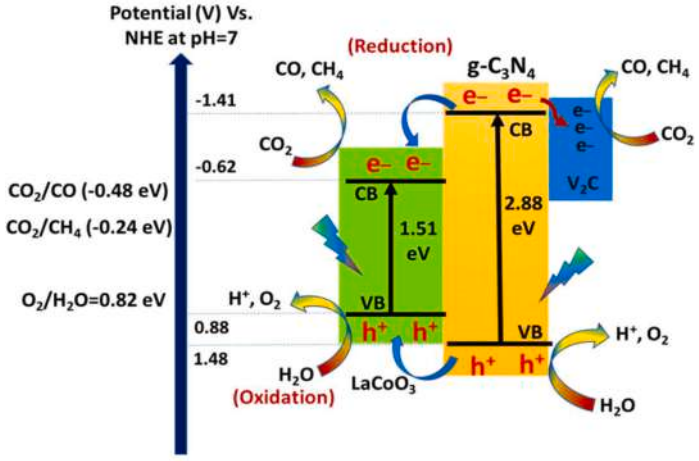


Fig. 19. Schematic illustration for charge carrier separation for photocatalytic CO_2 conversion into CO and CH_4 over the $LaCoO_3$/g-C_3N_4/V_2C photocatalysts under visible light. Reproduced with permission from Ref. [182].

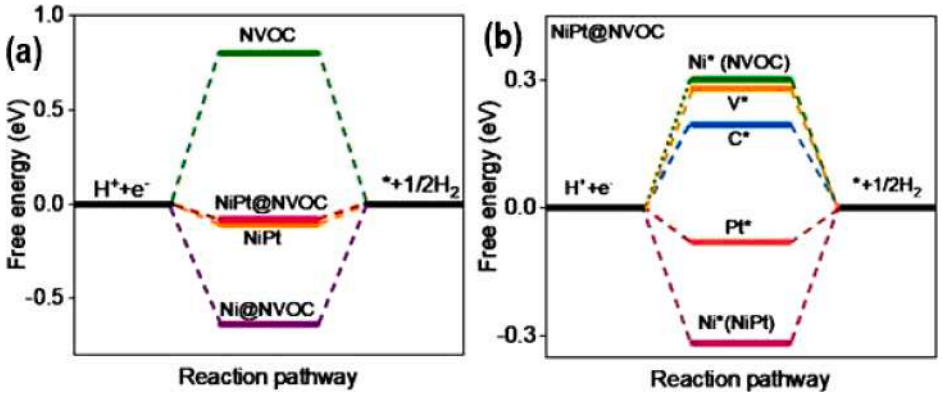


Fig. 21. ΔG_{H^*} diagram of (a) HER in acidic conditions for NiPt, NVOC, Ni@NVOC, and NiPt@NVOC and (b) HER for various active sites in NiPt@NVOC. Reproduced with permission from Ref. [190].

NiPt (0.32 eV), Ni in NVOC (0.3 eV), C (0.2 eV), and V (0.28 eV) (Fig. 21b).

Direct H* generation from H_3O^+, electron absorption, and adsorption on Pt during the Volmer step, followed by H_2 release in the Tafel stage ($H^* + H^* \rightarrow H_2$), comprise the HER mechanism on NiPt@NVOC, as shown in Fig. 22. In alkaline conditions, where H_3O^+ is absent, water dissociation occurs via the Volmer step [191]. This is made possible by positively charged Ni interacting with OH to weaken the H–OH bond, which causes H* adsorption on negatively charged Pt ($H_2O + e^- + * \rightarrow H^* + OH^-$). H_2 results from the following Tafel step ($H^* + H^* \rightarrow H_2$) [192]. The Tafel step is the rate-determining step (RDS) in alkaline solutions because high H_2O adsorption prevents H_2 desorption. In order to balance H_2O adsorption and H_2 desorption and speed up HER kinetics, improving the Tafel step requires optimizing the Pt d-orbital charge density [193].

An essential metric for evaluating electrochemical kinetics and determining the HER's rate-limiting phase is the Tafel slope. The Volmer, Heyrovsky, or Tafel steps are the usual routes used by the HER mechanism; in acidic and alkaline environments, these steps correspond to Tafel slopes of about 120, 40, and 30 mV per decade, respectively. Standard Pt/C catalysts have slopes of about 22.9 or 26 mV per decade, which is similar to these results. With a Tafel slope of 25.8 mV per decade, the NiPt@NVOC catalyst demonstrated better HER kinetics than several other catalysts (Fig. 23). Low Tafel slope values suggest that the Volmer–Tafel mechanism governs the HER on NiPt@NVOC, with the Tafel step serving as the stage that determines the rate. The slower water dissociation process that must take place before proton adsorption on the active electrocatalytic sites is probably the cause of the somewhat

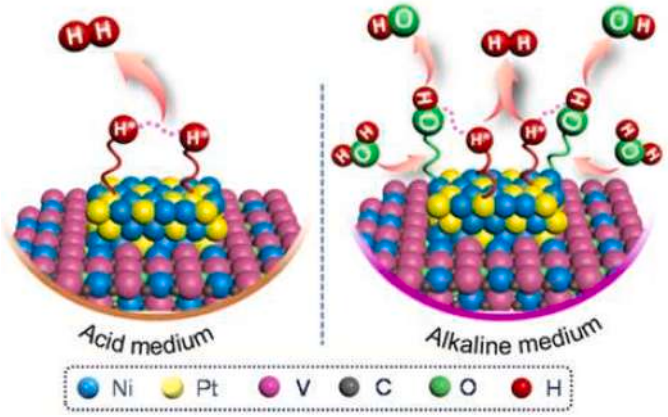


Fig. 22. Schematic representation of HER mechanism on NiPt@NVOC in acidic and alkaline conditions. Reproduced with permission from Ref. [190].

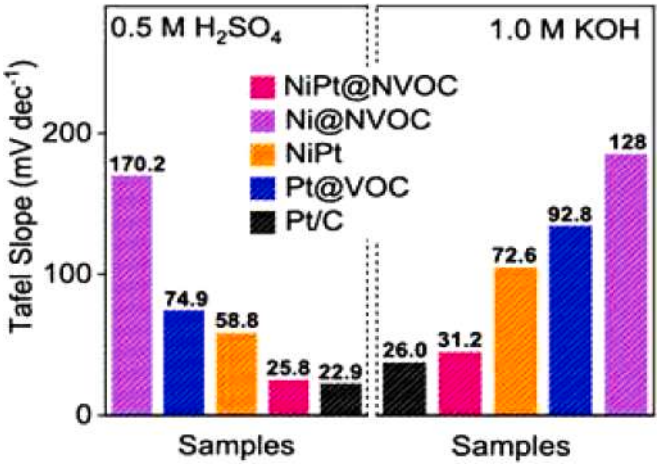


Fig. 23. Tafel slope values of various catalyst materials toward HER. Reproduced with permission from Ref. [190].

greater Tafel slopes seen in alkaline media as opposed to acidic ones. Key performance metrics such as overpotential, durability during long-term operation, and comparative benchmarking against noble metal-based catalysts were comprehensively evaluated when assessing MXene-based electrocatalysts for water splitting, as summarized in Table 3.

Consequently, in 0.5 M H_2SO_4 and 1.0 M KOH, the catalyst attains exceptionally low overpotentials of 11.9 and 35.6 mV at a current density of 10 mA cm^2. An anion exchange membrane water electrolyzer stack using the NiPt@NVOC-based cathode also shows remarkable durability at 1.0 A cm^2 over 2000 h of continuous operation, with a low voltage requirement of 1.70 and 1.83 V to reach 0.5 A cm^2 and 1.0 A cm^2 in 1.0 M KOH at 60 °C. The design of high-performance electrocatalysts for hydrogen production has advanced significantly as a result of these discoveries.

5. Stability and durability of MXene-based catalysts

The long-term stability and durability of MXene-based catalysts remain critical challenges for their practical application in catalysis, despite their excellent electrical conductivity, tunable surface chemistry, and unique 2D morphology. These challenges arise from surface oxidation, loss of active sites, structural degradation, and leaching of metal species under harsh reaction conditions. Addressing these concerns requires effective surface passivation strategies, enhanced structural and chemical stability, and robust regeneration and recycling approaches to maintain catalytic performance over extended operational periods (Fig. 24).

Table 3
Comparative Evaluation of MXene-Based Electrocatalysts for Electrochemical Water Splitting.

MXene electrocatalysts	Overpotential (mV)	Current density (mA/cm^2)	Long-term stability (hours)	Advantages	Ref
CeCoFeP@MXene	91–266	10	120	Structural stability, and a porous, high-surface-area architecture	[194]
Au/MXene	179.9	10	10	Synergetic effect between Au nanoparticles and MXene structures, enhanced ion diffusion and charge transfer.	[195]
$CuS/Ti_3C_2Cl_2$	334	100	48	Efficient bifunctional electrocatalysis for alkaline water splitting	[196]
$MoWS_2$@MXene	186	10	12	High porosity, ample electrochemical active sites, rapid charge transfer kinetics and barrier-free passage for ion transfer	[197]
$CuCl_2/Ti_3AlC_2$	330	100	36	Outstanding electrocatalytic activity	[198]
$MoNi_4-MX_{10}$	122–129	10	300	Chemical stability in alkaline solution	[199]
NiPt@NVOC	11.9–35.6	10	2000	Remarkable durability, low water dissociation energy barrier and kinetically favored intermediate's adsorption and hydrogen production	[190]

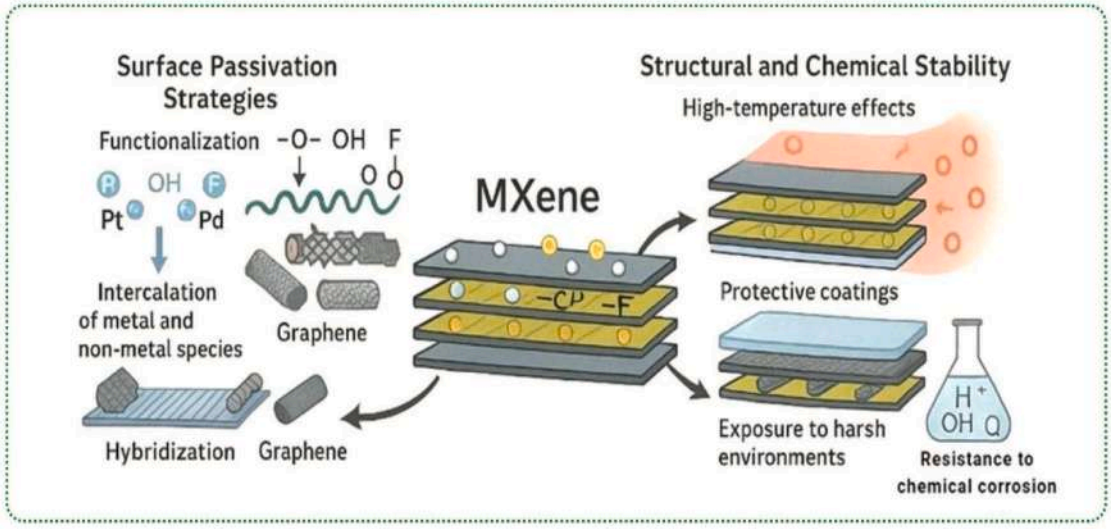


Fig. 24. Stability Challenges and Enhancement Strategies for MXene-Based Catalysts.

Building upon the promising catalytic properties discussed in this section, the long-term stability and durability of MXene-based catalysts represent key areas requiring further advancement for their widespread adoption.

5.1. *Surface passivation strategies*

MXenes are susceptible to passivation and surface oxidation in ambient circumstances, especially in high-temperature reactions and aqueous environments. The catalytic activity and electrical conductivity of MXene-based catalysts are adversely affected by the development of insulating oxides as a result of unchecked oxidation. A number of solutions have been developed to lessen these problems and increase their operating lifespan. The surface of MXenes, after etching from their MAX phase precursors, is typically terminated with functional groups like -O, -OH, and -F. These surface terminations are essential for establishing MXenes' hydrophilicity [200], catalytic activity [201], and electrical characteristics [202]. However, maximizing catalytic effectiveness requires managing the kind and density of these surface groups. Post-synthetic surface functionalization is one technique to customize these surface capabilities [203].

5.1.1. *Surface functionalization*

Oxygen-containing groups, such as oxygen (-O) and hydroxyl (-OH), are inherently present on MXene surfaces due to the etching process [200]. However, a variety of oxidation techniques can be used to control or further improve their density. For example, additional oxygen-containing groups can be introduced via controlled thermal oxidation or treatment with potent oxidizing agents such as potassium permanganate ($KMnO_4$) or hydrogen peroxide (H_2O_2) [204]. The catalytic activity may be considerably impacted by this increased oxygenation. A higher oxygen concentration makes MXenes more hydrophilic, which makes it easier for them to dissolve in polar liquids. This is especially advantageous in liquid-phase catalytic processes, where a high contact area between the catalyst and reactants is ensured by excellent dispersion. Groups that contain oxygen can serve as active sites for a variety of catalytic processes. For instance, surface oxygen species can help reactants become more active in oxidation processes. Furthermore, hydroxyl groups can supply Brønsted acid sites, which are essential for processes that are catalyzed by acids. The electronic structure of MXenes can be changed by surface oxygenation, which can affect their catalytic activity and redox characteristics [205]. Increased oxygen content, for example, can result in the development of oxygen vacancies and surface defects that can alter the electrical band structure or function as active sites. On the other hand, severe oxidation may cause the MXene structure to degrade, which would lower its conductivity and jeopardize its catalytic activity. As a result, careful regulation of the oxidation process is crucial.

5.1.2. *Intercalation of metal and non-metal species*

Intercalation, the insertion of guest species between the layers of MXenes, is another powerful strategy for modifying their catalytic properties [206]. New active sites can be introduced, the electrical structure can be changed, and the interlayer separation can be increased through intercalation. The catalytic activity of MXenes can be considerably increased by the intercalation of metal ions or nanoparticles. By increasing the interlayer gap, intercalation makes it easier for reactants and products to diffuse across the MXene structure. This is especially

advantageous for reactions that include large molecules. Different catalytic reactions can use metal ions or nanoparticles intercalated within MXene layers as active sites. For instance, the catalytic activity of hydrogenation or oxidation reactions can be increased by intercalating noble metal nanoparticles such as Pt, Pd, or Au [207]. By adding new electronic states or changing the charge distribution, metal species intercalation can change the electronic structure of MXenes. This may have an impact on MXenes' catalytic activity and redox characteristics. Ion exchange, impregnation, and electrochemical deposition are common techniques for metal intercalation. The particular catalytic application determines the metal species and intercalation technique.

The catalytic characteristics of MXenes can also be altered by the intercalation of non-metal species, such as polymers [208], organic molecules [209], or heteroatoms [210]. MXenes can be made more flexible and mechanically stable by intercalating organic molecules or polymers, which makes them appropriate for flexible catalytic devices. The interlayer spacing of MXenes can be controlled by the size and form of intercalated non-metal species, enabling the selective adsorption and reaction of particular molecules. The surface chemistry of MXenes can be changed or new active sites can be added by intercalating organic molecules with particular functional groups. For instance, nitrogen heteroatoms can be introduced into the MXene structure through the intercalation of nitrogen-containing organic molecules. These heteroatoms can serve as active sites for a variety of catalytic events.

5.1.3. Hybridization with nanomaterials

Hybridization, the combination of MXenes with other nanomaterials, is a versatile strategy for creating composite catalysts with enhanced performance [211]. This method improves activity, selectivity, and stability by utilizing the synergistic effects of several components [212–214]. Because MXenes provide a high density of active sites and improve charge transfer, they can be used with metal nanoparticles to increase catalytic activity. Metal nanoparticles like Pt, Pd, Au, or Ag are extremely effective catalysts for a variety of processes. They can have a large surface area and better charge transfer when hybridized with MXenes, which will increase their catalytic activity. Metal nanoparticles can be supported by MXenes, which will increase their stability and stop them from aggregating [211]. When MXenes and metal nanoparticles are combined, they can have synergistic effects, where the composite material's catalytic activity is higher than the sum of its constituent parts. MXene-metal nanoparticle hybrids can be prepared by electrochemical deposition, impregnation, and in-situ reduction.

MXenes can be combined with carbon-based materials like graphene, carbon nanotubes, or carbon nanofibers to improve the composite catalysts' stability, conductivity, and surface area [215]. Due to their high conductivity, carbon-based materials can be hybridized with MXenes to increase the composite material's total conductivity. For electrochemical catalytic reactions, this is advantageous. The total surface area of the composite material can be increased by hybridizing carbon-based materials with MXenes, which have high surface areas. This can increase catalytic activity and make active sites more accessible. MXenes can be supported by carbon-based materials, which will increase their stability and stop them from aggregating. Chemical vapor deposition, electrostatic self-assembly, and hydrothermal synthesis are common techniques for creating MXene-carbon-based material hybrids.

5.2. Structural and chemical stability under reaction conditions

During catalytic processes, MXene-based catalysts are exposed to a number of stressors, such as high temperatures [216], chemical corrosion [217], and electrochemical cycling [218]. For long-term uses, their capacity to preserve both structural integrity and catalytic activity in these circumstances is essential. In inert atmospheres, MXenes show good thermal stability; however, in oxidative or high-temperature environments, their stability is greatly impacted. According to studies, multilayer MXene structures may tolerate temperatures of up to 600 °C before experiencing appreciable structural deterioration [219]. However, when they oxidize at high temperatures, titanium oxides may develop (in the case of Ti-based MXenes), which would lower their catalytic efficacy [220]. Their tolerance to high temperatures can be improved by thermal stabilization techniques including doping with refractory metals or applying protective coatings. MXenes frequently come into contact with hostile chemical environments, including acidic, alkaline, and oxidative ones, in liquid-phase catalysis and electrochemical applications. It has been demonstrated that surface functionalization with stabilizing agents, like phosphate or sulfonate groups, increases resistance to chemical corrosion [221]. Furthermore, structural damage can be lessened by creating MXene composites with stable support elements like silica or carbon nanotubes [222].

5.3. Regeneration and recycling of MXene catalysts

Effective regeneration and recycling techniques must be developed to increase the usage of MXene-based catalysis and decrease material waste to attain sustainability [223]. Like other sophisticated catalysts, MXenes deactivate as a result of surface passivation, fouling, and structural deterioration. There are a number of physical and chemical methods for regenerating them. Firstly, thermal treatment in an inert or reducing atmosphere is one of the most straightforward techniques for regaining MXene's catalytic activity. Adsorbed reaction intermediates can be eliminated, active sites can be restored, and heating MXene-based catalysts can enhance catalyst performance to moderate temperatures (300–500 °C) [224]. Optimized thermal conditions are necessary since overheating can result in undesired phase changes.

Chemical reduction treatments can reverse oxidation-induced surface passivation [225]. For instance, surface oxides can be eliminated by hydrogen reduction at regulated temperatures, returning the MXene catalyst to its metallic state [226]. Furthermore, fouling species can be eliminated with mild acid or basic treatments without changing the structure of MXene. Additionally, reactive intermediates and passivation layers can be eliminated from MXene electrode surfaces in electrochemical applications by using pulse regeneration or periodic voltage cycling procedures [227,228]. In electrocatalytic water splitting and CO_2 reduction, when ion buildup or surface poisoning results in catalyst deactivation, this technique is especially helpful [229]. MXene-based catalysts may be effectively reused by putting these regeneration and recycling techniques into practice, which lowers material prices and lessens the impact on the environment (Fig. 25).

Overall, for MXene-based catalysts to be widely used in energy and environmental applications, their stability and longevity must be guaranteed. MXenes can be kept as high-performance catalysts for long operating lives by using strong regeneration and recycling techniques, structural and chemical stability improvements, and efficient surface passivation techniques. The optimization of these strategies should be the main goal of future studies in order to increase the robustness of MXene-based catalysts and open the door for their widespread industrial use.

6. Conclusion

MXenes have emerged as promising 2D materials due to their exceptional properties, including enhanced optical and electronic behavior, robust chemical stability, and tunable flexibility. As a result, extensive research has been conducted to explore their potential in catalysis. Various synthesis methods have been developed to obtain MXene-based catalysts. Top-down approaches involve the selective etching of MAX phases, such as molten salt preparation using the MILD approach with HCl and LiF, alkaline etching strategies with NaOH to remove the A-layer, and electrochemical etching using NaCl and NaF electrolytes to synthesize $Ti_3C_2T_x$ MXenes. On the other hand, bottom-up approaches such as Chemical Vapor Deposition (CVD) have been utilized to obtain Mo_2C crystals, while ALD has been employed to

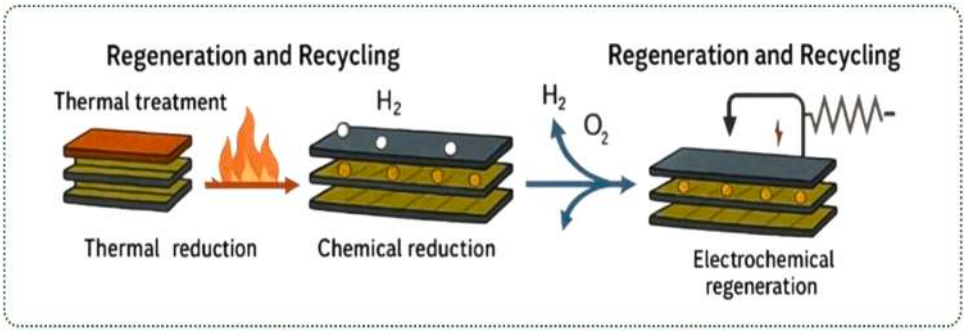


Fig. 25. Schematic diagram of the regeneration and recycling process of MXene-based catalysts.

synthesize metal-cluster-decorated MXene catalysts.

Regarding characterization techniques, XRD is used to define the phase structure and crystallinity of MXene-based catalysts, while Raman spectroscopy determines the phase composition of trimetallic oxide/MXene composites. TEM provides insights into the nanoscale morphology, as demonstrated for Mo_2TiC_2 electrocatalysts. The surface chemistry of Ti_3C_2 is analyzed using XPS, whereas FTIR identifies functional groups in g-C_3N_4-based photocatalysts. Additionally, catalytic performance is evaluated through TPD for Zn-based Nb_2CT_x catalysts and TPR to measure the redox properties of transition metal-supported MXene catalysts. Furthermore, in situ and operando techniques enable real-time monitoring of structural and chemical changes under reaction conditions.

Among key catalytic applications, the Fischer-Tropsch process, a cornerstone of hydrocarbon fuel production, has been investigated using Mo_2C-based catalysts, which demonstrated a tendency to form heavier hydrocarbons (C_{5+} alkanes). Additionally, CO_2 hydrogenation, catalyzed by a $LaCoO_3$/g-C_3N_4/V_2C heterojunction photocatalyst, achieved maximum CO and CH_4 generation rates at 0.4 bar pressure, highlighting its efficiency in methane production. The production of hydrogen, a crucial energy carrier, was explored through the electrochemical water-splitting process over MXene-derived NiV oxycarbide nanospheres (NiPt@NVOC). These catalysts exhibited remarkable durability of 2000 h in continuous operation, along with high hydrogen formation rates and selectivity.

One of the key factors in ensuring the efficiency of MXene-based catalysts is their stability and durability, which can be enhanced through various strategies. Surface passivation, achieved by terminating the surface with oxygen functional groups, helps improve resistance to degradation. Additionally, intercalation of metal and non-metal species, as well as hybridization with nanomaterials such as carbon nanofibers, can further enhance structural integrity and catalytic performance. Alternatively, effective regeneration and recycling techniques, including chemical reduction treatments, can be employed to prevent catalyst deactivation and extend operational lifespan.

Overall, MXene-based catalysts have demonstrated immense potential across various catalytic applications, particularly in energy-related processes such as hydrocarbon fuel synthesis, CO_2 conversion, and hydrogen production. The development of novel synthesis strategies, coupled with advanced characterization techniques, has contributed to a deeper understanding of their catalytic behavior. Future research efforts should focus on optimizing MXene properties, enhancing their stability under reaction conditions, and exploring new functionalization strategies to further expand their applications in sustainable energy production.

Future development in catalysis increasingly points to MXene-based systems due to their exceptional electronic conductivity, high surface area, and tunable surface functionalities. These 2D transition metal carbides and nitrides have a number of benefits that make them appropriate for a wider range of catalytic platforms in addition to the above-mentioned applications such as water-splitting, CO_2 methanation, and Fischer–Tropsch synthesis. MXenes show promise in improved oxidative desulfurization for cleaner fuels, organic pollutant degradation in environmental remediation, and electrocatalytic nitrogen reduction for sustainable ammonia generation. Both thermal and photoelectrocatalytic activity are made possible by the ability to customize their surface terminations (such as -OH, -F, and -O) to produce specific active sites for a variety of redox processes. Furthermore, researchers can create hierarchical structures that get beyond restrictions like stability, mass transport, or charge transfer inefficiencies that are commonly present in other catalytic systems because of their intrinsic flexibility in building composites.

A promising avenue is the combination of MXenes with metal–organic frameworks (MOFs), where the conductivity and catalytic anchoring capability of MXenes are enhanced by the structural diversity and porosity of MOFs. These MXene–MOF hybrids are appropriate for multifunctional catalysis, including biomass conversion, oxygen evolution reactions, electrochemical CO_2 reduction, and even the degradation of pharmaceutical waste, since they can bridge molecular-scale interactions with macroscopic performance. Furthermore, their capacity to function in challenging industrial and environmental settings provides versatility in a variety of fields, such as fuel cells, energy storage, and green chemical synthesis. The full potential of MXenes in next-generation catalytic technologies should be realized through interface engineering between MXenes and other materials, such as MOFs or single-atom catalysts, scalable production techniques, and long-term catalyst stability.

CRediT authorship contribution statement

Nur-Sultan Mussa: Writing – review & editing, Writing – original draft, Methodology, Formal analysis, Data curation, Conceptualization. **Kydyr Askaruly:** Conceptualization. **Kalampyr Bexeitova:** Visualization, Formal analysis, Data curation. **Seitkhan Azat:** Supervision, Conceptualization. **Kainaubek Toshtay:** Writing – review & editing, Writing – original draft, Conceptualization.

Declaration of competing interest

The authors declare that they have no known competing financial interests or personal relationships that could have appeared to influence the work reported in this paper.

Acknowledgements

This research has been funded by the Science Committee of the Ministry of Science and Higher Education of the Republic of Kazakhstan (Grant No BR24992873).

Data availability

No data was used for the research described in the article.

References

[1] M. Han, K. Maleski, C.E. Shuck, Y. Yang, J.T. Glazar, A.C. Foucher, K. Hantanasirisakul, A. Sarycheva, N.C. Frey, S.J. May, V.B. Shenoy, E.A. Stach, Y. Gogotsi, Tailoring electronic and optical properties of MXenes through forming solid solutions, J. Am. Chem. Soc. 142 (2020) 19110–19118, https://doi.org/10.1021/jacs.0c07395.

[2] X. Xu, L. Yang, W. Zheng, H. Zhang, F. Wu, Z. Tian, P. Zhang, Z. Sun, MXenes with applications in supercapacitors and secondary batteries: a comprehensive review, Mater. Reports Energy 2 (2022) 100080, https://doi.org/10.1016/j.matre.2022.100080.

[3] X. Li, Z. Huang, C.E. Shuck, G. Liang, Y. Gogotsi, C. Zhi, MXene chemistry, electrochemistry and energy storage applications, Nat. Rev. Chem. 6 (2022) 389–404, https://doi.org/10.1038/s41570-022-00384-8.

[4] C.E. Shuck, M. Han, K. Maleski, K. Hantanasirisakul, S.J. Kim, J. Choi, W.E. B. Reil, Y. Gogotsi, Effect of Ti_3AlC_2 MAX phase on structure and properties of resultant $Ti_3C_2T_x$ MXene, ACS Appl. Nano Mater. 2 (2019) 3368–3376, https://doi.org/10.1021/acsanm.9b00286.

[5] K. Maleski, C.E. Ren, M.-Q. Zhao, B. Anasori, Y. Gogotsi, Size-dependent physical and electrochemical properties of two-dimensional MXene flakes, ACS Appl. Mater. Interfaces 10 (2018) 24491–24498, https://doi.org/10.1021/acsami.8b04662.

[6] T.P. Nguyen, D.M. Tuan Nguyen, D.L. Tran, H.K. Le, D.-V.N. Vo, S.S. Lam, R. S. Varma, M. Shokouhimehr, C.C. Nguyen, Q. Van Le, MXenes: applications in electrocatalytic, photocatalytic hydrogen evolution reaction and CO_2 reduction, Mol. Catal. 486 (2020) 110850, https://doi.org/10.1016/j.mcat.2020.110850.

[7] V.-H. Nguyen, B.-S. Nguyen, C. Hu, C.C. Nguyen, D.L.T. Nguyen, M.T. Nguyen Dinh, D.-V.N. Vo, Q.T. Trinh, M. Shokouhimehr, A. Hasani, S.Y. Kim, Q. Van Le, Novel architecture titanium carbide ($Ti_3C_2T_x$) MXene cocatalysts toward photocatalytic hydrogen production: a mini-review, Nanomaterials 10 (2020) 602, https://doi.org/10.3390/nano10040602.

[8] R.M. Ronchi, J.T. Arantes, S.F. Santos, Synthesis, structure, properties and applications of MXenes: current status and perspectives, Ceram. Int. 45 (2019) 18167–18188, https://doi.org/10.1016/j.ceramint.2019.06.114.

[9] T. Schultz, N.C. Frey, K. Hantanasirisakul, S. Park, S.J. May, V.B. Shenoy, Y. Gogotsi, N. Koch, Surface termination dependent work function and electronic properties of $Ti_3C_2T_x$ MXene, Chem. Mater. 31 (2019) 6590–6597, https://doi.org/10.1021/acs.chemmater.9b00414.

[10] M. Shekhirev, J. Busa, C.E. Shuck, A. Torres, S. Bagheri, A. Sinitskii, Y. Gogotsi, Ultralarge flakes of $Ti_3C_2T_x$ MXene via soft delamination, ACS Nano 16 (2022) 13695–13703, https://doi.org/10.1021/acsnano.2c04506.

[11] L. Jiang, D. Zhou, J. Yang, S. Zhou, H. Wang, X. Yuan, J. Liang, X. Li, Y. Chen, H. Li, 2D single- and few-layered MXenes: synthesis, applications and perspectives, J. Mater. Chem. A 10 (2022) 13651–13672, https://doi.org/10.1039/D2TA01572B.

[12] I. Persson, A. el Ghazaly, Q. Tao, J. Halim, S. Kota, V. Darakchieva, J. Palisaitis, M.W. Barsoum, J. Rosen, P.O.Å. Persson, Tailoring structure, composition, and energy storage properties of MXenes from selective etching of In-plane, chemically ordered MAX phases, Small 14 (2018), https://doi.org/10.1002/smll.201703676.

[13] Y. Wang, Y. Wang, Recent progress in MXene layers materials for supercapacitors: high-performance electrodes, SmartMat 4 (2023), https://doi.org/10.1002/smm2.1130.

[14] M. Alhabeb, K. Maleski, B. Anasori, P. Lelyukh, L. Clark, S. Sin, Y. Gogotsi, Guidelines for synthesis and processing of two-dimensional titanium carbide ($Ti_3C_2T_x$ MXene), Chem. Mater. 29 (2017) 7633–7644, https://doi.org/10.1021/acs.chemmater.7b02847.

[15] G. Deysher, C.E. Shuck, K. Hantanasirisakul, N.C. Frey, A.C. Foucher, K. Maleski, A. Sarycheva, V.B. Shenoy, E.A. Stach, B. Anasori, Y. Gogotsi, Synthesis of Mo_4VAlC_4 MAX phase and two-dimensional Mo_4VC_4 MXene with five atomic layers of transition metals, ACS Nano 14 (2020) 204–217, https://doi.org/10.1021/acsnano.9b07708.

[16] N. Li, J. Peng, W.-J. Ong, T. Ma, P.Zhang Arramel, J. Jiang, X. Yuan, C. (John) Zhang, MXenes: an emerging platform for wearable electronics and looking beyond, Matter 4 (2021) 377–407, https://doi.org/10.1016/j.matt.2020.10.024.

[17] O. Salim, K.A. Mahmoud, K.K. Pant, R.K. Joshi, Introduction to MXenes: synthesis and characteristics, Mater. Today Chem. 14 (2019) 100191, https://doi.org/10.1016/j.mtchem.2019.08.010.

[18] P. Das, Z.-S. Wu, MXene for energy storage: present status and future perspectives, J. Phys. Energy 2 (2020) 032004, https://doi.org/10.1088/2515-7655/ab9b1d.

[19] K. Hantanasirisakul, Y. Gogotsi, Electronic and optical properties of 2D transition metal carbides and nitrides (MXenes), Adv. Mater. 30 (2018), https://doi.org/10.1002/adma.201804779.

[20] M. Khazaei, A. Mishra, N.S. Venkataramanan, A.K. Singh, S. Yunoki, Recent advances in MXenes: from fundamentals to applications, Curr. Opin. Solid State Mater. Sci. 23 (2019) 164–178, https://doi.org/10.1016/j.cossms.2019.01.002.

[21] P.E. Lokhande, A. Pakdel, H.M. Pathan, D. Kumar, D.-V.N. Vo, A. Al-Gheethi, A. Sharma, S. Goel, P.P. Singh, B.-K. Lee, Prospects of MXenes in energy storage applications, Chemosphere 297 (2022) 134225, https://doi.org/10.1016/j.chemosphere.2022.134225.

[22] A. Maleki, M. Ghomi, N. Nikfarjam, M. Akbari, E. Sharifi, M. Shahbazi, M. Kermanian, M. Seyedhamzeh, E. Nazarzadeh Zare, M. Mehrali, O. Moradi, F. Sefat, V. Mattoli, P. Makvandi, Y. Chen, Biomedical applications of MXene-integrated composites: regenerative medicine, infection therapy, cancer treatment, and biosensing, Adv. Funct. Mater. 32 (2022), https://doi.org/10.1002/adfm.202203430.

[23] J. Pang, R.G. Mendes, A. Bachmatiuk, L. Zhao, H.Q. Ta, T. Gemming, H. Liu, Z. Liu, M.H. Rummeli, Applications of 2D MXenes in energy conversion and storage systems, Chem. Soc. Rev. 48 (2019) 72–133, https://doi.org/10.1039/C8CS00324F.

[24] N. Rabiee, M. Bagherzadeh, M. Jouyandeh, P. Zarrintaj, M.R. Saeb, M. Mozafari, M. Shokouhimehr, R.S. Varma, Natural polymers decorated MOF-MXene nanocarriers for Co-delivery of Doxorubicin/pCRISPR, ACS Appl. Bio Mater. 4 (2021) 5106–5121, https://doi.org/10.1021/acsabm.1c00332.

[25] Y. Sun, C. Dall'Agnese, C. Zhang, L. Yang, X. Jin, Y. Dall'Agnese, X.-F. Wang, Applications of MXenes and their composites in catalysis and photoelectrocatalysis. Mxenes Their Compos, Elsevier, 2022, pp. 449–498, https://doi.org/10.1016/B978-0-12-823361-0.00007-1.

[26] S. Bai, M. Yang, J. Jiang, X. He, J. Zou, Z. Xiong, G. Liao, S. Liu, Recent advances of MXenes as electrocatalysts for hydrogen evolution reaction, Npj 2D Mater. Appl. 5 (2021) 78, https://doi.org/10.1038/s41699-021-00259-4.

[27] A. Bhat, S. Anwer, K.S. Bhat, M.I.H. Mohideen, K. Liao, A. Qurashi, Prospects challenges and stability of 2D MXenes for clean energy conversion and storage applications, Npj 2D Mater. Appl. 5 (2021) 61, https://doi.org/10.1038/s41699-021-00239-8.

[28] W. Kong, J. Deng, L. Li, Recent advances in noble metal MXene-based catalysts for electrocatalysis, J. Mater. Chem. A 10 (2022) 14674–14691, https://doi.org/10.1039/D2TA00613H.

[29] S. Ponnada, M.S. Kiai, D.B. Gorle, R.S.C. Bose, V. Rajagopal, B. Saini, M. Kathiresan, A. Nowduri, R. Singhal, F. Marken, M.A. Kulandainathan, K. K. Nanda, R.K. Sharma, Recent status and challenges in multifunctional electrocatalysis based on 2D MXenes, Catal. Sci. Technol. 12 (2022) 4413–4441, https://doi.org/10.1039/D2CY00428C.

[30] S.G. Peera, C. Liu, A.K. Sahu, M. Selvaraj, M.C. Rao, T.G. Lee, R. Koutavarapu, J. Shim, L. Singh, Recent advances on MXene-based electrocatalysts toward oxygen reduction reaction: a focused review, Adv. Mater. Interfaces 8 (2021), https://doi.org/10.1002/admi.202100975.

[31] M. Carey, M.W. Barsoum, MXene polymer nanocomposites: a review, Mater. Today Adv. 9 (2021) 100120, https://doi.org/10.1016/j.mtadv.2020.100120.

[32] Y. Zhou, K. Maleski, B. Anasori, J.O. Thostenson, Y. Pang, Y. Feng, K. Zeng, C. B. Parker, S. Zauscher, Y. Gogotsi, J.T. Glass, C. Cao, $Ti_3C_2T_x$ MXene-reduced graphene oxide composite electrodes for stretchable supercapacitors, ACS Nano 14 (2020) 3576–3586, https://doi.org/10.1021/acsnano.9b10066.

[33] M. Zubair, M.M. Ul Hassan, M.T. Mehran, M.M. Baig, S. Hussain, F. Shahzad, 2D MXenes and their heterostructures for HER, OER and overall water splitting: a review, Int. J. Hydrogen Energy 47 (2022) 2794–2818, https://doi.org/10.1016/j.ijhydene.2021.10.248.

[34] Z. Lei, S. Ali, C. Sathish, M. Ahmed, J. Qu, R. Zheng, S. Xi, X. Yu, M.B.H. Breese, C. Liu, J. Zhang, S. Qi, X. Guan, V. Perumalsamy, M. Fawaz, J.-H. Yang, M. Bououdina, K. Domen, A. Vinu, L. Qiao, J. Yi, Transition metal carbonitride MXenes anchored with Pt sub-nanometer clusters to achieve high-performance hydrogen evolution reaction at all pH range, Nano-Micro Lett. 17 (2025) 123, https://doi.org/10.1007/s40820-025-01654-y.

[35] H. Liu, Z. Li, D. Kong, X. Chen, FeCN/MXene as novel heterogeneous electro-Fenton catalysts for the degradation of sulfathiazole: performance and mechanism investigation, J. Environ. Sci. 154 (2025) 300–313, https://doi.org/10.1016/j.jes.2024.07.024.

[36] L. Yang, Q. Wen, Y. Chen, C. Lin, H. Gao, Z. Qiu, X. Pan, Capacitive bio–electrocatalyst Mxene@CoMo–ZIF sulfide heterostructure for boosted biofilm electroactivity to enhance renewable energy conversion, Renew. Energy 243 (2025) 122545, https://doi.org/10.1016/j.renene.2025.122545.

[37] S. Chao, Y. Xue, M. Xu, Q. Wu, J. Li, C. Li, Y. Guo, Q. Zhang, Y. Zhao, F. Wu, Strategy of constructing unsaturated bond on hexagonal pore MXene through titanium vacancy defects realizes antioxidant stable storage of potassium-ions in neutral aqueous system, J. Colloid Interface Sci. 688 (2025) 362–374, https://doi.org/10.1016/j.jcis.2025.02.121.

[38] C. Xia, H. Ye, A. Kim, A. Sabahi Namini, S. Li, S.A. Delbari, J.Y. Park, D. Kim, Q. Van Le, R.S. Varma, R. Luque, A. T-Raissi, H.W. Jang, M. Shokouhimehr, Recent catalytic applications of MXene-based layered nanomaterials, Chemosphere 325 (2023) 138323, https://doi.org/10.1016/j.chemosphere.2023.138323.

[39] W. Ye, H. Zhao, X. Wang, R. Ma, W. Liu, W. Zhao, P.F. Msomi, S. Song, O-terminated $Ti_3C_2T_x$ supported sulfurized NiCo layered double hydroxide as efficient electrocatalyst for methanol coupled water electrolysis, Int. J. Hydrogen Energy 92 (2024) 270–282, https://doi.org/10.1016/j.ijhydene.2024.10.237.

[40] K. Wu, G. Lu, B. Huang, Z. Hu, Y. Lv, H.A. Younus, X. Wang, Z. Liu, S. Zhang, Entropy-driven highly chaotic MXene-based heterostructures as an efficient sulfur redox electrocatalysts for Li-S battery, Adv. Funct. Mater. 34 (2024), https://doi.org/10.1002/adfm.202404976.

[41] J.O. Ighalo, P.B. Amama, Recent progress in the design of dry reforming catalysts supported on low-dimensional materials, J. CO_2 Util. 81 (2024) 102734, https://doi.org/10.1016/j.jcou.2024.102734.

[42] S. Chen, Z. Lu, J. Niu, Y. Shao, Y. Chen, Y. Ni, X. Liu, X. Wei, X. Ou, X. Fan, Y. Wei, H. Chen, Enhancing H_2 production from plasma-assisted methanol steam reforming by catalyst engineering in a MXene membrane reactor, AIChE J. 71 (2025), https://doi.org/10.1002/aic.18685.

[43] Y. Cheng, W. Wang, C. Shao, Revealing the origin of activity and selectivity in nitrate to ammonia conversion on single transition metal atom catalysts supported by a Ti_2NO_2 monolayer, Phys. Chem. Chem. Phys. 27 (2025) 4202–4210, https://doi.org/10.1039/D5CP00062A.

[44] Y. Zhou, Y. Chai, X. Li, Z. Wu, J. Lin, Y. Han, L. Li, H. Qi, Y. Gu, L. Kang, X. Wang, Defect-rich TiO_2 In situ evolved from MXene for the enhanced oxidative dehydrogenation of ethane to ethylene, ACS Catal. 11 (2021) 15223–15233, https://doi.org/10.1021/acscatal.1c04409.
[45] J. Nie, X. Zhang, M. Wang, Y. Ou, S. Li, P. Zhong, W. Wang, G. Zhu, X. Ma, MXene quantum dots decorated g-C_3N_4/BiOI heterojunction photocatalyst for efficient NO deep oxidation and CO_2 reduction, Sep. Purif. Technol. 354 (2025) 128961, https://doi.org/10.1016/j.seppur.2024.128961.
[46] J.J. John Jeya Kamaraj, A. Kunka Ravindran, S.P. Muthu, R. Perumalsamy, MXene-supported 2D bimetallic chalcogenide electrocatalyst: enhanced electrochemical seawater splitting, J. Power Sources 629 (2025) 235951, https://doi.org/10.1016/j.jpowsour.2024.235951.
[47] E. Kountoupi, A.J. Barrios, Z. Chen, C.R. Müller, V.V. Ordomsky, A. Comas-Vives, A. Fedorov, The impact of oxygen surface coverage and carbidic carbon on the activity and selectivity of two-dimensional molybdenum carbide (2D-Mo_2C) in Fischer–Tropsch synthesis, ACS Catal. 14 (2024) 1834–1845, https://doi.org/10.1021/acscatal.3c03956.
[48] M.O. Madi, M. Tahir, Ternary V_2C-$LaCoO_3$ coupled g-C_3N_4 composite for investigating influential parameters in photocatalytic CO_2 methanation through response surface methodology, Mater. Sci. Eng. B 313 (2025) 117953, https://doi.org/10.1016/j.mseb.2024.117953.
[49] L. Ding, J. Xu, Z. Zhang, K. Qi, G. Jin, N,S-doped Ti_3C_2 MXene quantum dots-anchored metal ruthenium: efficient electrocatalyst for pH-universal hydrogen evolution reaction, J. Colloid Interface Sci. 689 (2025) 137245, https://doi.org/10.1016/j.jcis.2025.03.034.
[50] F. Zhu, C. Liu, L. Hao, C. Xu, Y. Zhu, X. Liu, H. He, H. Huang, 2D/2D Heterojunction of cobalt-iron selenide nanolamellas/MXene for enhanced electrocatalytic hydrogen evolution, ChemNanoMat 10 (2024), https://doi.org/10.1002/cnma.202400045.
[51] M. Jussambayev, K. Shakenov, S. Sultakhan, U. Zhantikeyev, K. Askaruly, K. Toshtay, S. Azat, MXenes for sustainable energy: a comprehensive review on conservation and storage applications, Carbon Trends 19 (2025) 100471, https://doi.org/10.1016/j.cartre.2025.100471.
[52] N. Oefner, C.E. Shuck, L. Schumacher, F. Heck, K. Hofmann, J. Schmidpeter, W. Li, M. Bahri, B.L. Mehdi, A. Drochner, B. Albert, C. Hess, Y. Gogotsi, B.J. M. Etzold, MXene Aerogel derived ultra-active Vanadia catalyst for selective conversion of sustainable alcohols to base chemicals, ACS Appl. Mater. Interfaces 15 (2023) 16714–16722, https://doi.org/10.1021/acsami.2c22720.
[53] R.S. Mane, S. Mane, V. Somkuwar, N.V. Thombre, A.V. Patwardhan, N. Jha, A novel hierarchically hybrid structure of MXene and bi-ligand ZIF-67 based trifunctional electrocatalyst for zinc-air battery and water splitting, Batter. Energy 2 (2023), https://doi.org/10.1002/bte2.20230019.
[54] V. Prajapati, A. Shah, R. Patel, N.A. Trivedi, N.N. Som, D.N. Srivastava, P. M. Pataniya, C.K. Sumesh, Utilizing electrooxidation for textile effluent wastewater treatment and simultaneous electrocatalytic hydrogen production: transforming waste into energy and promoting water reuse in a circular economy context, Renew. Energy 237 (2024) 121733, https://doi.org/10.1016/j.renene.2024.121733.
[55] J. Lemena, R.A. Harris, H.C. Swart, J. J.Terblans, D.E. Motaung, Advances in the engineering of MXenes-based sensors: a transition towards advanced sensing technologies, Sens. Actuators B (2025) 137939, https://doi.org/10.1016/j.snb.2025.137939.
[56] S. Riaz, S. Ullah, S. Bashir, A.ur Rehman, R. Iqbal, T. Najam, M.A. Ismail, M. R. Karim, S.S. Ahmad Shah, M.A. Nazir, Recent advances in layered double hydroixdes@MXene (LDHs@MXene) composites: synthesis, properties, and catalytic applications, Appl. Clay Sci. 275 (2025) 107866, https://doi.org/10.1016/j.clay.2025.107866.
[57] R. Wang, X. Dai, Z. Qian, S. Zhong, S. Chen, S. Fan, H. Zhang, F. Wu, Boosting lithium storage in free-standing black phosphorus anode via multifunction of nanocellulose, ACS Appl. Mater. Interfaces 12 (28) (2020) 31628–31636, https://doi.org/10.1021/acsami.0c08346.
[58] D. Jiang, Z. Liu, Z. Xiao, Z. Qian, Y. Sun, Z. Zeng, R. Wang, Flexible electronics based on 2D transition metal dichalcogenides, J. Mater. Chem. A. 10 (1) (2022) 89–121, https://doi.org/10.1039/D1TA06741A.
[59] Q. Chen, Y. Wei, P.B. Zhai, Y.J. Gong, Van der Waals gap engineering in 2D materials for energy storage and conversion, Rare Met. 43 (12) (2024) 6125–6143, https://doi.org/10.1007/s12598-024-02817-3.
[60] Z. Xiao, X. Dai, D. Jiang, H. Xie, X. Liu, M. Wu, D. Liu, Y. Li, Zh. Qian, R. Wang, 3D nanocellulose matrix enhancing the lithiation dynamics of $FePS_3$ anode, Adv. Funct. Mater. 33 (45) (2023) 2304766, https://doi.org/10.1002/adfm.202304766.
[61] Z. Korkembay, K. Toshtay, M. Atamanov, F. Malchik, R. Amrousse, Y. Merkibayev, Determination of the catalytic activity of the MXene in the combustion of ammonium perchlorate, J. Eng. Phys. Thermophys. 97 (2024) 1651, https://doi.org/10.1007/s10891-024-03043-5.
[62] Z. Cui, P. Zhao, H. Wang, C. Li, W. Peng, X. Fan, J. Liu, Molten salts etching strategy construct alloy/MXene heterostructures for efficient ammonia synthesis and energy supply via Zn-nitrite battery, Appl. Catal. B Environ. Energy 348 (2024) 123862, https://doi.org/10.1016/j.apcatb.2024.123862.
[63] Y. Zhang, J. Luo, X. Wang, D. Zhang, H. Xu, Y. Sun, X. Gu, X. Hu, B. Gao, H. Ren, Photoresponse of $Ti_3C_2T_x$ MXene promotes its adsorptive-reductive removal of Cr (VI) from water, J. Environ. Manag. 370 (2024) 122673, https://doi.org/10.1016/j.jenvman.2024.122673.
[64] Q. Zhang, J. He, X. Fu, S. Xie, R. Fan, H. Lai, W. Cheng, P. Ji, J. Sheng, Q. Liao, W. Zhu, H. Li, Fluorine-free strategy for hydroxylated Ti_3C_2/Ti_3AlC_2 catalysts with enhanced aerobic oxidative desulfurization and mechanism, Chem. Eng. J. 430 (2022) 132950, https://doi.org/10.1016/j.cej.2021.132950.
[65] A.T. Isa, H.Y. Hafeez, J. Mohammed, C.E. Ndikilar, A.B. Suleiman, A.D.G. Kafadi, Photocatalytic performance of MXenes co-catalyst in hydrogen (H_2) production via photocatalytic water splitting: a review, J. Alloys Compd. 1005 (2024) 175951, https://doi.org/10.1016/j.jallcom.2024.175951.
[66] L. Liu, H. Zschiesche, M. Antonietti, B. Daffos, N.V. Tarakina, M. Gibilaro, P. Chamelot, L. Massot, B. Duployer, P. Taberna, P. Simon, Tuning the surface chemistry of MXene to improve energy storage: example of nitrification by salt melt, Adv. Energy Mater. 13 (2023), https://doi.org/10.1002/aenm.202202709.
[67] D.D. Kruger, H. García, A. Primo, Molten salt derived MXenes: synthesis and applications, Adv. Sci. 11 (35) (2024) 2307106, https://doi.org/10.1002/advs.202307106.
[68] M. Rostami, A. Badiei, Molten salt-shielded preparation of the ultrathin nanosheets of $Ti_3C_2Cl_2$@TiO_2 coupled with Fe_3O_4@C-C_3N_4 for assessing photocatalytic activity, Ceram. Int. 50 (2024) 13608–13620, https://doi.org/10.1016/j.ceramint.2024.01.275.
[69] Y. Li, H. Shao, Z. Lin, J. Lu, L. Liu, B. Duployer, P.O.Å. Persson, P. Eklund, L. Hultman, M. Li, K. Chen, X.-H. Zha, S. Du, P. Rozier, Z. Chai, E. Raymundo-Piñero, P.-L. Taberna, P. Simon, Q. Huang, A general Lewis acidic etching route for preparing MXenes with enhanced electrochemical performance in non-aqueous electrolyte, Nat. Mater. 19 (2020) 894–899, https://doi.org/10.1038/s41563-020-0657-0.
[70] X. Zhang, X. Bai, C. Wei, Z. Wang, B. Xi, S. Xiong, J. Feng, Triggering the electronic microenvironment of extraordinary nitrogen-bridged atomic iron coordinated with in-plane nitrogen by manipulating phase-reconfigured 2D vanadium nitride MXenes toward invigorated lithium–sulfur batteries, Energy Environ. Sci. 17 (2024) 7403–7415, https://doi.org/10.1039/D4EE02979H.
[71] J.Y. Kim, S.H. Ahn, D.G. Kim, Z.M. Huang, Y.S. Song, Injection-molded PEO/MXene nanocomposite for polymer-based solid-state electrolyte, Compos. Commun. 50 (2024) 102005, https://doi.org/10.1016/j.coco.2024.102005.
[72] A. Gentile, S. Marchionna, M. Balordi, G. Pagot, C. Ferrara, V. Di Noto, R. Ruffo, Critical analysis of MXene production with In-situ HF forming agents for sustainable manufacturing, ChemElectroChem 9 (23) (2022), https://doi.org/10.1002/celc.202200891 e202200891.
[73] X. Zhang, W. Zhang, H. Zhao, Electrochemical performance of $Ti_3C_2T_x$ MXenes obtained via ultrasound assisted LiF-HCl method, Mater. Today Commun. 33 (2022) 104384, https://doi.org/10.1016/j.mtcomm.2022.104384.
[74] P. Sarkar, K. Chatterjee, P. Pal, K. Das, Exploring the molarity of Lithium Fluoride in minimally intensive layer delamination (MILD) method for efficient room temperature synthesis of high quality $Ti_3C_2T_x$ free-standing film, Mater. Sci. Semicond. Process. 185 (2025) 108881, https://doi.org/10.1016/j.mssp.2024.108881.
[75] F. Bibi, L. Siok Ee, M. Khalid, A. Numan, Effect of ammonium and sodium fluoride etchants on the synthesis of double transition metal ($Mo_2TiC_2T_x$) MXene, ECS J. Solid State Sci. Technol. 14 (2025) 021005, https://doi.org/10.1149/2162-8777/adb78b.
[76] C.B. Cockreham, V.G. Goncharov, E. Hammond-Pereira, M.E. Reece, A. C. Strzelecki, W. Xu, S.R. Saunders, H. Xu, X. Guo, D. Wu, Energetic stability and interfacial complexity of $Ti_3C_2T_x$ MXenes synthesized with HF/HCl and CoF_2/HCl as etching agents, ACS Appl. Mater. Interfaces 14 (2022) 41542–41554, https://doi.org/10.1021/acsami.2c09669.
[77] X. Wang, C. Garnero, G. Rochard, D. Magne, S. Morisset, S. Hurand, P. Chartier, J. Rousseau, T. Cabioc'h, C. Coutanceau, V. Mauchamp, S. Célérier, A new etching environment (FeF_3/HCl) for the synthesis of two-dimensional titanium carbide MXenes: a route towards selective reactivity vs. water, J. Mater. Chem. A 5 (2017) 22012–22023, https://doi.org/10.1039/C7TA01082F.
[78] Z. Wei, Z. Peigen, T. Wubian, Q. Xia, Z. Yamei, S. ZhengMing, Alkali treated $Ti_3C_2T_x$ MXenes and their dye adsorption performance, Mater. Chem. Phys. 206 (2018) 270–276, https://doi.org/10.1016/j.matchemphys.2017.12.034.
[79] M. Kulkarni, A. Lalic, R. Balu, H. Zhang, N.K. Dutta, N.Roy Choudhury, Hydrothermal synthesis of MXenes in alkali environment and development of MXene/PEDOT:PSS composite electrodes for supercapacitor applications, MRS Adv. 9 (2024) 1310–1317, https://doi.org/10.1557/s43580-024-00951-9.
[80] Y. Li, X. Feng, W.Y. Lieu, L. Fu, C. Zhang, T. Ghosh, A. Thakur, B.C. Wyatt, B. Anasori, W. Liu, Q. Zhang, J. Lu, Z.W. Seh, MXene-based anode-free magnesium metal battery, Adv. Funct. Mater. 33 (2023), https://doi.org/10.1002/adfm.202303067.
[81] D. Liu, J. Liu, C. Li, Y. Ji, Y. Han, Z. Xue, Q. Lv, J. Chen, Y. Wang, H. Li, Tailoring surface terminals on MXene enables high-efficiency electromagnetic absorption, Carbon N. Y. 228 (2024) 119392, https://doi.org/10.1016/j.carbon.2024.119392.
[82] T. Li, L. Yao, Q. Liu, J. Gu, R. Luo, J. Li, X. Yan, W. Wang, P. Liu, B. Chen, W. Zhang, W. Abbas, R. Naz, D. Zhang, Fluorine-free synthesis of high-purity $Ti_3C_2T_x$ (T=OH, O) via Alkali treatment, Angew. Chemie Int. Ed. 57 (2018) 6115–6119, https://doi.org/10.1002/anie.201800887.
[83] X. Xie, Y. Xue, L. Li, S. Chen, Y. Nie, W. Ding, Z. Wei, Surface Al leached Ti_3AlC_2 as a substitute for carbon for use as a catalyst support in a harsh corrosive electrochemical system, Nanoscale 6 (2014) 11035–11040, https://doi.org/10.1039/C4NR02080D.
[84] J. Xuan, Z. Wang, Y. Chen, D. Liang, L. Cheng, X. Yang, Z. Liu, R. Ma, T. Sasaki, F. Geng, Organic-base-driven intercalation and delamination for the production of functionalized titanium carbide nanosheets with superior photothermal therapeutic performance, Angew. Chemie 128 (2016) 14789–14794, https://doi.org/10.1002/ange.201606643.

[85] G. Li, L. Tan, Y. Zhang, B. Wu, L. Li, Highly efficiently delaminated single-layered MXene nanosheets with large lateral size, Langmuir 33 (2017) 9000–9006, https://doi.org/10.1021/acs.langmuir.7b01339.

[86] G. Zou, J. Guo, X. Liu, Q. Zhang, G. Huang, C. Fernandez, Q. Peng, Hydrogenated core–shell MAX@$K_2Ti_8O_{17}$ pseudocapacitance with ultrafast sodium storage and long-term cycling, Adv. Energy Mater. 7 (2017), https://doi.org/10.1002/aenm.201700700.

[87] W. Yuan, L. Cheng, Y. An, H. Wu, N. Yao, X. Fan, X. Guo, MXene nanofibers as highly active catalysts for hydrogen evolution reaction, ACS Sustain. Chem. Eng. 6 (2018) 8976–8982, https://doi.org/10.1021/acssuschemeng.8b01348.

[88] A. Shahzad, M. Nawaz, M. Moztahida, K. Tahir, J. Kim, Y. Lim, B. Kim, J. Jang, D. S. Lee, Exfoliation of titanium aluminum carbide (211 MAX Phase) to form nanofibers and two-dimensional nanosheets and their application in aqueous-phase cadmium sequestration, ACS Appl. Mater. Interfaces 11 (2019) 19156–19166, https://doi.org/10.1021/acsami.9b03899.

[89] F.E.A. Latif, M. Khalid, A. Numan, N.A. Manaf, N.M. Mubarak, H.A. Zaharin, E. C. Abdullah, Microwave-assisted hydrothermal synthesis of $Ti_3C_2T_x$ MXene: a sustainable and scalable approach using alkaline etchant, J. Mol. Struct. 1329 (2025) 141407, https://doi.org/10.1016/j.molstruc.2025.141407.

[90] X. Li, M. Li, Q. Yang, G. Liang, Z. Huang, L. Ma, D. Wang, F. Mo, B. Dong, Q. Huang, C. Zhi, In situ electrochemical synthesis of MXenes without acid/alkali usage in/for an aqueous zinc ion battery, Adv. Energy Mater. 10 (2020), https://doi.org/10.1002/aenm.202001791.

[91] J. Chen, M. Chen, W. Zhou, X. Xu, B. Liu, W. Zhang, C. Wong, Simplified synthesis of fluoride-free $Ti_3C_2T_x$ via electrochemical etching toward high-performance electrochemical capacitors, ACS Nano 16 (2022) 2461–2470, https://doi.org/10.1021/acsnano.1c09004.

[92] T. Yin, Y. Li, R. Wang, O.A. Al-Hartomy, A. Al-Ghamdi, S. Wageh, X. Luo, X. Tang, H. Zhang, Synthesis of $Ti_3C_2F_x$ MXene with controllable fluorination by electrochemical etching for lithium-ion batteries applications, Ceram. Int. 47 (2021) 28642–28649, https://doi.org/10.1016/j.ceramint.2021.07.023.

[93] P. Srivastava, A. Mishra, H. Mizuseki, K.-R. Lee, A.K. Singh, Mechanistic insight into the chemical exfoliation and functionalization of Ti_3C_2 MXene, ACS Appl. Mater. Interfaces 8 (2016) 24256–24264, https://doi.org/10.1021/acsami.6b08413.

[94] S.-Y. Pang, Y.-T. Wong, S. Yuan, Y. Liu, M.-K. Tsang, Z. Yang, H. Huang, W.-T. Wong, J. Hao, Universal strategy for HF-free facile and rapid synthesis of two-dimensional MXenes as multifunctional energy materials, J. Am. Chem. Soc. 141 (2019) 9610–9616, https://doi.org/10.1021/jacs.9b02578.

[95] M.R. Lukatskaya, O. Mashtalir, C.E. Ren, Y. Dall'Agnese, P. Rozier, P.L. Taberna, M. Naguib, P. Simon, M.W. Barsoum, Y. Gogotsi, Cation intercalation and high volumetric capacitance of two-dimensional titanium carbide, Science 341 (2013) 1502–1505, https://doi.org/10.1126/science.1241488.

[96] X. Zou, H. Liu, H. Xu, X. Wu, X. Han, J. Kang, K.M. Reddy, A simple approach to synthesis Cr_2CT_x MXene for efficient hydrogen evolution reaction, Mater. Today Energy 20 (2021) 100668, https://doi.org/10.1016/j.mtener.2021.100668.

[97] D. Wang, C. Zhou, A.S. Filatov, W. Cho, F. Lagunas, M. Wang, S. Vaikuntanathan, C. Liu, R.F. Klie, D.V. Talapin, Direct synthesis and chemical vapor deposition of 2D carbide and nitride MXenes, Science 379 (2023) 1242–1247, https://doi.org/10.1126/science.add9204.

[98] K.M.M.D.K. Kimbulapitiya, B. Rehman, S.S. Wani, C.-T. Chen, R.-H. Cyu, A. Manikandan, M.K. Date, Y.-R. Peng, R.J.G.L.R. Kumara, F.-C. Chuang, Y.-L. Chueh, Phase-engineered heterostructures of Mo_2C by plasma-assisted selenization and sulfurization processes toward excellent hydrogen evolution reaction, Nano Energy 122 (2024) 109235, https://doi.org/10.1016/j.nanoen.2023.109235.

[99] N. Li, H. Dai, M. He, J. Wang, Z. Cheng, B. Yan, W. Peng, G. Chen, Cu distribution pattern controlled active species generation and sulfamethoxazole degradation routes in a peroxymonosulfate system, Engineering (2023), https://doi.org/10.1016/j.eng.2023.07.020.

[100] D. Guo, X. Guo, X. Li, Construction of 3D porous MXene-based multiple heterojunction catalyst for efficient water oxidation reaction at high current density, J. Colloid Interface Sci. 691 (2025) 137441, https://doi.org/10.1016/j.jcis.2025.137441.

[101] X. Du, Y. Wang, Z. Ye, W. Wang, Y. Wang, Interface effect of MXene/CoP_2 on oxygen evolution reaction, Mater. Lett. 360 (2024) 136024, https://doi.org/10.1016/j.matlet.2024.136024.

[102] Inamuddin, R. Boddula, M.I. Ahamed, A.M. Asiri (Eds.), Layered 2D Advanced Materials and Their Allied Applications, Wiley, 2020, https://doi.org/10.1002/9781119655190.

[103] K.P. Akshay Kumar, K. Ghosh, O. Alduhaish, M. Pumera, Dip-coating of MXene and transition metal dichalcogenides on 3D-printed nanocarbon electrodes for the hydrogen evolution reaction, Electrochem. Commun. 122 (2021) 106890, https://doi.org/10.1016/j.elecom.2020.106890.

[104] Z. Li, Y. Xiao, P.R. Chowdhury, Z. Wu, T. Ma, J.Z. Chen, G. Wan, T.-H. Kim, D. Jing, P. He, P.J. Potdar, L. Zhou, Z. Zeng, X. Ruan, J.T. Miller, J.P. Greeley, Y. Wu, A. Varma, Direct methane activation by atomically thin platinum nanolayers on two-dimensional metal carbides, Nat. Catal. 4 (2021) 882–891, https://doi.org/10.1038/s41929-021-00686-y.

[105] X. Zhang, B. Shao, Z. Sun, Z. Gao, Y. Qin, C. Zhang, F. Cui, X. Yang, Platinum nanoparticle-deposited $Ti_3C_2T_x$ MXene for hydrogen evolution reaction, Ind. Eng. Chem. Res. 59 (2020) 1822–1828, https://doi.org/10.1021/acs.iecr.9b05046.

[106] S.M. El-Mas, M.A. Hassaan, G.M. El-Subruiti, A.S. Eltaweil, A. El Nemr, Microwave-induced degradation of Congo red dye in the presence of 2D $Ti_3C_2T_x$ MXene as a catalyst, Sci. Rep. 15 (2025) 634, https://doi.org/10.1038/s41598-024-82911-9.

[107] L. Chen, X. Shi, N. Yu, X. Zhang, X. Du, J. Lin, Measurement and analysis of thermal conductivity of Ti_3C_2tx MXene films, Materials (Basel) 11 (2018) 1701, https://doi.org/10.3390/ma11091701.

[108] X. Wang, X. Fan, M. Li, W. Zhu, J. Xue, F. Ye, L. Cheng, Cheng, Structure and electromagnetic properties of $Ti_3C_2T_x$ MXene derived from Ti_3AlC_2 with different microstructures, Ceram. Int. (2021) 13628–13634, https://doi.org/10.1016/j.ceramint.2021.01.223.

[109] R. Garg, A. Agarwal, M. Agarwal, Synthesis and optimisation of MXene for supercapacitor application, J. Mater. Sci. 31 (2020) 18614–18626, https://doi.org/10.1007/s10854-020-04404-5.

[110] S.M. Albukhari, M. Abdel Salam, A.M.M. Aldawsari, Removal of malachite green dye from water using MXene (Ti_3C_2) nanosheets, Sustainability 14 (2022) 5996, https://doi.org/10.3390/su14105996.

[111] Y.-T. Kao, C. Young, Trimetallic oxide catalysts from metal-organic frameworks on ti$_3$c$_2$tx MXene for enhanced water splitting, Int. J. Hydrogen Energy 100 (2025) 704–712, https://doi.org/10.1016/j.ijhydene.2024.12.190.

[112] Y. Zhang, R. Hu, H. Su, Y. Su, Enhancement of C_{5+} selectivity in photothermal Fischer–Tropsch synthesis by an inorganic heteropoly acid catalyst promotor, Catal. Sci. Technol. 13 (2023) 2092–2100, https://doi.org/10.1039/D3CY00002H.

[113] A. Rosenkranz, L. Freeman, B. Suen, Y. Fainman, F.E. Talke, Tip-enhanced raman spectroscopy studies on amorphous carbon films and carbon overcoats in commercial hard disk drives, Tribol. Lett. 66 (2018) 54, https://doi.org/10.1007/s11249-018-1005-2.

[114] B. Ma, R.D. Rodriguez, A. Ruban, S. Pavlov, E. Sheremet, The correlation between electrical conductivity and second-order Raman modes of laser-reduced graphene oxide, Phys. Chem. Chem. Phys. 21 (2019) 10125–10134, https://doi.org/10.1039/C9CP00093C.

[115] M.A. Pimenta, G. Dresselhaus, M.S. Dresselhaus, L.G. Cançado, A. Jorio, R. Saito, Studying disorder in graphite-based systems by Raman spectroscopy, Phys. Chem. Chem. Phys. 9 (2007) 1276–1290, https://doi.org/10.1039/B613962K.

[116] J. Schwan, S. Ulrich, V. Batori, H. Ehrhardt, S.R.P. Silva, Raman spectroscopy on amorphous carbon films, J. Appl. Phys. 80 (1996) 440–447, https://doi.org/10.1063/1.362745.

[117] K. Farooq, Z. Yang, M. Murtaza, M.A. Naseeb, A. Waseem, Y. Zhu, Y. Xia, MXene-enhanced metal–Organic framework-derived CoP nanocomposites as highly efficient trifunctional electrocatalysts for OER, HER, and ORR, Adv. Energy Sustain. Res. (2025), https://doi.org/10.1002/aesr.202400400.

[118] J. Liew, S. Bashir, K. Ramesh, S. Ramesh, A comprehensive characterisation of titanium carbide (Ti_3C_2) MXene with hydrothermal-assisted in-situ hydrofluoric acid etching, Mater. Sci. Eng. B 314 (2025) 118076, https://doi.org/10.1016/j.mseb.2025.118076.

[119] H. Zhang, Y. Huang, X. Wang, J. Meng, L. Gao, Y. Li, Y. Zhang, Y. Liao, W.-L. Dai, Tightly-bound interfaces between $ZnIn_2S_4$ nanosheets and few-layered Mo_2TiC_2 MXene induced highly efficient noble-metal-free Schottky junction for photocatalytic hydrogen evolution, Sep. Purif. Technol. 360 (2025) 131199, https://doi.org/10.1016/j.seppur.2024.131199.

[120] H. Gu, H. Zhang, X. Wang, Q. Li, S. Chang, Y. Huang, L. Gao, Y. Cui, R. Liu, W.-L. Dai, Robust construction of CdSe nanorods@Ti_3C_2 MXene nanosheet for superior photocatalytic H_2 evolution, Appl. Catal. B Environ. 328 (2023) 122537, https://doi.org/10.1016/j.apcatb.2023.122537.

[121] Q. Zhao, W. Zhou, M. Zhang, Y. Wang, Z. Duan, C. Tan, B. Liu, F. Ouyang, Z. Yuan, H. Tai, Y. Jiang, Edge-enriched Mo_2TiC_2Tx/MoS_2 heterostructure with coupling interface for selective NO_2 monitoring, Adv. Funct. Mater. 32 (2022), https://doi.org/10.1002/adfm.202203528.

[122] D. Nugroho, Y.J. Joo, K.Y. Cho, R. Benchawattananon, S. Chanthai, W.-C. Oh, Synergistic magnetic field effect to enhance photocatalytic effect for pharmaceutics degradation by Ti_3C_2 MXene/GQDs@ZnO, J. Photochem. Photobiol. A Chem. 462 (2025) 116224, https://doi.org/10.1016/j.jphotochem.2024.116224.

[123] G.L. Kabongo, G.H. Mhlongo, B.M. Mothudi, K.T. Hillie, P.S. Mbule, M. S. Dhlamini, Structural, photoluminescence and XPS properties of Tm^{3+} ions in ZnO nanostructures, J. Lumin. 187 (2017) 141–153, https://doi.org/10.1016/j.jlumin.2017.02.024.

[124] Y. Wang, S. Wang, R. Li, W. Li, T. Long, L. Wang, L. Kong, F. Cao, Q. Wu, G. Jia, X. Yang, Quantum-confined perovskite nanocrystals enabled by negative catalyst strategy for efficient light-emitting diodes, Small 20 (2024), https://doi.org/10.1002/smll.202402825.

[125] S.W. Lee, M.L. Luna, N. Berdunov, W. Wan, S. Kunze, S. Shaikhutdinov, B. R. Cuenya, Unraveling surface structures of gallium promoted transition metal catalysts in CO_2 hydrogenation, Nat. Commun. 14 (2023) 4649, https://doi.org/10.1038/s41467-023-40361-3.

[126] C. Xiao, Z. Ma, X. Gao, P. Zou, L. Jia, Fabrication of Pt functionalized $LaFeO_3$ porous structures for highly sensitive detection of formaldehyde, Sensors Actuators B Chem. 410 (2024) 135644, https://doi.org/10.1016/j.snb.2024.135644.

[127] A. Pazniak, P. Bazhin, N. Shplis, E. Kolesnikov, I. Shchetinin, A. Komissarov, J. Polcak, A. Stolin, D. Kuznetsov, $Ti_3C_2T_x$ MXene characterization produced from SHS-ground Ti_3AlC_2, Mater. Des. 183 (2019) 108143, https://doi.org/10.1016/j.matdes.2019.108143.

[128] Y.S. Alqahtani, A.M. Mahmoud, M.H. Mahnashi, R. Ali, R.Y. Shahin, M.M. El-Wekil, H.A. Batakoushy, Facile fabrication of boron and nitrogen co-doped carbon dots for "ON–OFF–ON" fluorescence sensing of Al^{3+} and F^- ions in water samples, RSC Adv. 13 (2023) 23736–23744, https://doi.org/10.1039/D3RA02919K.

[129] Y. Song, Y. Peng, N.V. Long, Z. Huang, Y. Yang, Multifunctional self-assembly 3D Ag/g-C_3N_4/RGO aerogel as highly efficient adsorbent and photocatalyst for R6G

removal from wastewater, Appl. Surf. Sci. 542 (2021) 148584, https://doi.org/10.1016/j.apsusc.2020.148584.
[130] J. Xiong, H.-Y. Zeng, S. Xu, J.-F. Peng, F.-Y. Liu, L.-H. Wang, Enhancing the intrinsic properties of flower-like BiOI by S-doping toward excellent photocatalytic performances, J. Mater. Sci. Technol. 118 (2022) 181–189, https://doi.org/10.1016/j.jmst.2021.12.024.
[131] X. Bai, L. Wang, Y. Wang, W. Yao, Y. Zhu, Enhanced oxidation ability of g-C_3N_4 photocatalyst via C_{60} modification, Appl. Catal. B Environ. 152–153 (2014) 262–270, https://doi.org/10.1016/j.apcatb.2014.01.046.
[132] X. Lu, Y. Jin, X. Zhang, G. Xu, D. Wang, J. Lv, Z. Zheng, Y. Wu, Controllable synthesis of graphitic C_3N_4/ultrathin MoS_2 nanosheet hybrid nanostructures with enhanced photocatalytic performance, Dalt. Trans. 45 (2016) 15406–15414, https://doi.org/10.1039/C6DT02247B.
[133] J. Jiang, Y. Song, X. Wang, T. Li, M. Li, Y. Lin, T. Xie, S. Dong, Enhancing aqueous pollutant photodegradation via a Fermi level matched Z-scheme BiOI/Pt/g-C_3N_4 photocatalyst: unobstructed photogenerated charge behavior and degradation pathway exploration, Catal. Sci. Technol. 10 (2020) 3324–3333, https://doi.org/10.1039/D0CY00429D.
[134] A. Shahzad, K. Rasool, M. Nawaz, W. Miran, J. Jang, M. Moztahida, K. A. Mahmoud, D.S. Lee, Heterostructural TiO_2/$Ti_3C_2T_x$ (MXene) for photocatalytic degradation of antiepileptic drug carbamazepine, Chem. Eng. J. 349 (2018) 748–755, https://doi.org/10.1016/j.cej.2018.05.148.
[135] S. Gong, G. Zhu, R. Wang, F. Rao, X. Shi, J. Gao, Y. Huang, C. He, M. Hojamberdiev, Synergistically boosting highly selective CO_2–to–CO photoreduction over BiOCl nanosheets via in-situ formation of surface defects and non-precious metal nanoparticles, Appl. Catal. B Environ. 297 (2021) 120413, https://doi.org/10.1016/j.apcatb.2021.120413.
[136] S. Chen, A. Chen, Electrochemical reduction of carbon dioxide on Au nanoparticles: an in situ FTIR study, J. Phys. Chem. C 123 (2019) 23898–23906, https://doi.org/10.1021/acs.jpcc.9b04080.
[137] K.D. Dubois, A. Petushkov, E. Garcia Cardona, S.C. Larsen, G. Li, Adsorption and photochemical properties of a molecular CO_2 reduction catalyst in hierarchical mesoporous ZSM-5: an In situ FTIR study, J. Phys. Chem. Lett. 3 (2012) 486–492, https://doi.org/10.1021/jz201701y.
[138] R.W. Stevens, R.V. Siriwardane, J. Logan, In situ fourier transform infrared (FTIR) investigation of CO_2 adsorption onto zeolite materials, Energy Fuels 22 (2008) 3070–3079, https://doi.org/10.1021/ef800209a.
[139] X. Li, H. Jiang, C. Ma, Z. Zhu, X. Song, H. Wang, P. Huo, X. Li, Local surface plasma resonance effect enhanced Z-scheme ZnO/Au/g-C_3N_4 film photocatalyst for reduction of CO2 to CO, Appl. Catal. B Environ. 283 (2021) 119638, https://doi.org/10.1016/j.apcatb.2020.119638.
[140] H. Shi, Q. Li, T. Su, X. Luo, Z. Qin, H. Ji, CoZn B/Nb2CT (MXene) for cinnamaldehyde hydrogenation to cinnamyl alcohol: effects of Zn, Appl. Catal. A Gen. 689 (2025) 120024, https://doi.org/10.1016/j.apcata.2024.120024.
[141] J.L. Hart, K. Hantanasirisakul, A.C. Lang, B. Anasori, D. Pinto, Y. Pivak, J.T. van Omme, S.J. May, Y. Gogotsi, M.L. Taheri, Control of MXenes' electronic properties through termination and intercalation, Nat. Commun. 10 (2019) 522, https://doi.org/10.1038/s41467-018-08169-8.
[142] N. Khandan, M. Kazemeini, M. Aghaziarati, Determining an optimum catalyst for liquid-phase dehydration of methanol to dimethyl ether, Appl. Catal. A Gen. 349 (2008) 6–12, https://doi.org/10.1016/j.apcata.2008.07.029.
[143] Q. Li, H. Shi, T. Su, X. Luo, X. Xie, Z. Qin, H. Ji, Multilayer Nb_2CT_x (MXene) supports CoB for the selective hydrogenation of cinnamaldehyde to cinnamyl alcohol: effect of the electron-modified CoB site and lewis acid site, Catal. Lett. 154 (2024) 4457–4468, https://doi.org/10.1007/s10562-024-04642-w.
[144] J. Wang, Y. Wang, Y. Wang, X. Li, C. Wu, T. Zhang, B. Tian, L. Qian, Y. Guo, L. Wu, L. Zheng, Y. Li, X. Ding, Novel two-dimensional $Ti_3C_2T_x$ MXene-supported Ni-M (M = Pd, Pt, Ru): a remarkable catalyst for efficient HDO of guaiacol under hydrothermal conditions: performance, mechanism and kinetic studies, Fuel 374 (2024) 132493, https://doi.org/10.1016/j.fuel.2024.132493.
[145] L. Li, G. Zhao, Z. Lv, P. An, J. Ao, M. Song, J. Zhao, G. Liu, Optimizing coordination environment in bimetallic NiPt catalysts boosts n-dodecane steam reforming, Chem. Eng. J. 474 (2023) 145647, https://doi.org/10.1016/j.cej.2023.145647.
[146] J. Gao, Y. Cao, G. Luo, J. Fan, J.H. Clark, S. Zhang, High-efficiency catalytic hydrodeoxygenation of lignin-derived vanillin with nickel-supported metal phosphate catalysts, Chem. Eng. J. 448 (2022) 137723, https://doi.org/10.1016/j.cej.2022.137723.
[147] X. Ding, T. Li, J. Wang, L. Wu, L. Zheng, Y. Wang, Catalytic co-liquefaction of microalgae + corn straw over K_3PO_4+γ-Al_2O_3 supported Fe and Ni mono-/bimetallic in-situ composite catalysts for the production of liquid biofuel, Chem. Eng. J. 471 (2023) 144668, https://doi.org/10.1016/j.cej.2023.144668.
[148] F. Wang, R. Pace, Y. Ji, J. Jiang, X. Jiang, A. Krystianiak, O. Heintz, G. Caboche, E. Santillan-Jimenez, M. Crocker, Effect of Pd promotion and catalyst support on the Ni-catalyzed deoxygenation of tristearin to fuel-like hydrocarbons, Renew. Energy 195 (2022) 1468–1479, https://doi.org/10.1016/j.renene.2022.06.065.
[149] J. Wang, S. Zhang, J. Ma, X. Liu, Y. Ma, Z. Fan, J. Wang, Augmenting levoglucosan production through catalytic pyrolysis of biomass exploiting $Ti_3C_2T_x$ MXene, Chinese Chem. Lett. 35 (2024) 109725, https://doi.org/10.1016/j.cclet.2024.109725.
[150] N. Huang, T. Su, Z. Qin, H. Ji, Nickel supported on multilayer vanadium carbide for dry reforming of methane, ChemistrySelect 7 (2022), https://doi.org/10.1002/slct.202203873.
[151] D. Tyndall, L. Gannon, L. Hughes, J. Carolan, S. Pinilla, S. Jaśkaniec, D. Spurling, O. Ronan, C. McGuinness, N. McEvoy, V. Nicolosi, M.P. Browne, Understanding the effect of MXene in a TMO/MXene hybrid catalyst for the oxygen evolution reaction, Npj 2D Mater. Appl. 7 (2023) 15, https://doi.org/10.1038/s41699-023-00377-1.
[152] Z. Li, J. Xiong, H. Song, S. Liu, Y. Huang, Y. Huang, G.I.N. Waterhouse, Z. Wang, Y. Mao, Z. Liang, X. Luo, Synergistically enhancing CO_2 adsorption/activation and electron transfer in ZIF-67/$Ti_3C_2T_x$ MXene for boosting photocatalytic CO_2 reduction, Sep. Purif. Technol. 341 (2024) 126817, https://doi.org/10.1016/j.seppur.2024.126817.
[153] K.T. Rommens, M. Saeys, Molecular views on Fischer–Tropsch synthesis, Chem. Rev. 123 (2023) 5798–5858, https://doi.org/10.1021/acs.chemrev.2c00508.
[154] C.K. Rofer-DePoorter, A comprehensive mechanism for the Fischer-Tropsch synthesis, Chem. Rev. 81 (1981) 447–474, https://doi.org/10.1021/cr00045a002.
[155] G.L. Bezemer, J.H. Bitter, H.P.C.E. Kuipers, H. Oosterbeek, J.E. Holewijn, X. Xu, F. Kapteijn, A.J. van Dillen, K.P. de Jong, Cobalt particle size effects in the Fischer−Tropsch reaction studied with carbon nanofiber supported catalysts, J. Am. Chem. Soc. 128 (2006) 3956–3964, https://doi.org/10.1021/ja058282w.
[156] I.A.W. Filot, R.A. van Santen, E.J.M. Hensen, The optimally performing Fischer–Tropsch catalyst, Angew. Chemie Int. Ed. 53 (2014) 12746–12750, https://doi.org/10.1002/anie.201406521.
[157] A.Y. Khodakov, W. Chu, P. Fongarland, Advances in the development of novel cobalt Fischer−Tropsch catalysts for synthesis of long-chain hydrocarbons and clean fuels, Chem. Rev. 107 (2007) 1692–1744, https://doi.org/10.1021/cr050972v.
[158] V.V. Ordomsky, Y. Luo, B. Gu, A. Carvalho, P.A. Chernavskii, K. Cheng, A. Y. Khodakov, Soldering of iron catalysts for direct synthesis of light olefins from Syngas under mild reaction conditions, ACS Catal. 7 (2017) 6445–6452, https://doi.org/10.1021/acscatal.7b01307.
[159] V. Subramanian, K. Cheng, C. Lancelot, S. Heyte, S. Paul, S. Moldovan, O. Ersen, M. Marinova, V.V. Ordomsky, A.Y. Khodakov, Nanoreactors: an efficient tool to control the chain-length distribution in Fischer–Tropsch synthesis, ACS Catal. 6 (2016) 1785–1792, https://doi.org/10.1021/acscatal.5b01596.
[160] Y. Chen, N. Batalha, M. Marinova, M. Impéror-Clerc, C. Ma, O. Ersen, W. Baaziz, J.A. Stewart, D. Curulla-Ferré, A.Y. Khodakov, V.V. Ordomsky, Ruthenium silica nanoreactors with varied metal–wall distance for efficient control of hydrocarbon distribution in Fischer–Tropsch synthesis, J. Catal. 365 (2018) 429–439, https://doi.org/10.1016/j.jcat.2018.06.023.
[161] S. Zaman, K.J. Smith, A review of molybdenum catalysts for synthesis gas conversion to alcohols: catalysts, mechanisms and kinetics, Catal. Rev. 54 (2012) 41–132, https://doi.org/10.1080/01614940.2012.627224.
[162] P. Patterson, Carbon monoxide hydrogenation over molybdenum and tungsten carbides, Appl. Catal. A Gen. 251 (2003) 449–455, https://doi.org/10.1016/S0926-860X(03)00371-5.
[163] J.A. Schaidle, L.T. Thompson, Fischer–Tropsch synthesis over early transition metal carbides and nitrides: CO activation and chain growth, J. Catal. 329 (2015) 325–334, https://doi.org/10.1016/j.jcat.2015.05.020.
[164] H.-G. Kim, K.H. Lee, J.S. Lee, Carbon monoxide hydrogenation over molybdenum carbide catalysts, Res. Chem. Intermed. 26 (2000) 427–443, https://doi.org/10.1163/156856700×00435.
[165] A. Griboval-Constant, Catalytic behaviour of cobalt or ruthenium supported molybdenum carbide catalysts for FT reaction, Appl. Catal. A Gen. 260 (2004) 35–45, https://doi.org/10.1016/j.apcata.2003.10.031.
[166] H.C. Woo, K.Y. Park, Y.G. Kim, I.-S. Namau]Jong ShikChung, J.S. Lee, Mixed alcohol synthesis from carbon monoxide and dihydrogen over potassium-promoted molybdenum carbide catalysts, Appl. Catal. 75 (1991) 267–280, https://doi.org/10.1016/S0166-9834(00)83136-X.
[167] Q. Wu, J.M. Christensen, G.L. Chiarello, L.D.L. Duchstein, J.B. Wagner, B. Temel, J.-D. Grunwaldt, A.D. Jensen, Supported molybdenum carbide for higher alcohol synthesis from syngas, Catal. Today 215 (2013) 162–168, https://doi.org/10.1016/j.cattod.2013.03.002.
[168] T. Li, M. Virginie, A.Y. Khodakov, Effect of potassium promotion on the structure and performance of alumina supported carburized molybdenum catalysts for Fischer-Tropsch synthesis, Appl. Catal. A Gen. 542 (2017) 154–162, https://doi.org/10.1016/j.apcata.2017.05.018.
[169] D.-V.N. Vo, T.-H. Nguyen, E.M. Kennedy, B.Z. Dlugogorski, A.A. Adesina, Fischer–Tropsch synthesis: effect of promoter type on alumina-supported Mo carbide catalysts, Catal. Today 175 (2011) 450–459, https://doi.org/10.1016/j.cattod.2011.04.045.
[170] M. Naguib, O. Mashtalir, J. Carle, V. Presser, J. Lu, L. Hultman, Y. Gogotsi, M. W. Barsoum, Two-dimensional transition metal carbides, ACS Nano 6 (2012) 1322–1331, https://doi.org/10.1021/nn204153h.
[171] B. Anasori, M.R. Lukatskaya, Y. Gogotsi, 2D metal carbides and nitrides (MXenes) for energy storage, Nat. Rev. Mater. 2 (2017) 16098, https://doi.org/10.1038/natrevmats.2016.98.
[172] M. Naguib, V.N. Mochalin, M.W. Barsoum, Y. Gogotsi, 25th Anniversary article: MXenes: a new Family of two-dimensional materials, Adv. Mater. 26 (2014) 992–1005, https://doi.org/10.1002/adma.201304138.
[173] K.R.G. Lim, M. Shekhirev, B.C. Wyatt, B. Anasori, Y. Gogotsi, Z.W. Seh, Fundamentals of MXene synthesis, Nat. Synth. 1 (2022) 601–614, https://doi.org/10.1038/s44160-022-00104-6.
[174] E.B. Deeva, A. Kurlov, P.M. Abdala, D. Lebedev, S.M. Kim, C.P. Gordon, A. Tsoukalou, A. Fedorov, C.R. Müller, In situ XANES/XRD study of the structural stability of two-dimensional molybdenum carbide Mo_2CT_x : implications for the catalytic activity in the water–Gas shift reaction, Chem. Mater. 31 (2019) 4505–4513, https://doi.org/10.1021/acs.chemmater.9b01105.
[175] H. Zhou, Z. Chen, E. Kountoupi, A. Tsoukalou, P.M. Abdala, P. Florian, A. Fedorov, C.R. Müller, Two-dimensional molybdenum carbide 2D-Mo_2C as a

superior catalyst for CO_2 hydrogenation, Nat. Commun. 12 (2021) 5510, https://doi.org/10.1038/s41467-021-25784-0.
[176] M. Tahir, Construction of a stable two-dimensional MAX supported protonated graphitic carbon nitride (pg-C_3N_4)/Ti_3AlC_2/TiO_2 Z-scheme multiheterojunction system for efficient photocatalytic CO_2 reduction through dry reforming of methanol, Energy & Fuels 34 (2020) 3540–3556, https://doi.org/10.1021/acs.energyfuels.9b04393.
[177] X. Wang, Q. Li, Q. Lin, R. Zhang, M. Ding, CdS-sensitized 3D ordered macroporous g-C_3N_4 for enhanced visible-light photocatalytic hydrogen generation, J. Mater. Sci. Technol. 111 (2022) 204–210, https://doi.org/10.1016/j.jmst.2021.09.046.
[178] L. Wang, G. Huang, L. Zhang, R. Lian, J. Huang, H. She, C. Liu, Q. Wang, Construction of TiO_2-covalent organic framework Z-Scheme hybrid through coordination bond for photocatalytic CO_2 conversion, J. Energy Chem. 64 (2022) 85–92, https://doi.org/10.1016/j.jechem.2021.04.053.
[179] S.-R. Xu, F.-X. Xiao, Metal halide perovskites quantum dots: synthesis and modification strategies for solar CO_2 conversion, Chinese J. Struct. Chem. 42 (2023) 100173, https://doi.org/10.1016/j.cjsc.2023.100173.
[180] R.R. Ikreedeegh, M. Tahir, A critical review in recent developments of metal-organic-frameworks (MOFs) with band engineering alteration for photocatalytic CO_2 reduction to solar fuels, J. CO_2 Util. 43 (2021) 101381, https://doi.org/10.1016/j.jcou.2020.101381.
[181] M. Tahir, B. Tahir, Constructing S-scheme 2D/0D g-C_3N_4/TiO_2 NPs/MPs heterojunction with 2D-Ti_3AlC_2 MAX cocatalyst for photocatalytic CO2 reduction to CO/CH_4 in fixed-bed and monolith photoreactors, J. Mater. Sci. Technol. 106 (2022) 195–210, https://doi.org/10.1016/j.jmst.2021.08.019.
[182] M.O. Madi, M. Tahir, Well-designed 2D vanadium carbide (V_2C) MXenes supported $LaCoO_3$/g-C_3N_4 heterojunction for highly efficient and stable photocatalytic CO_2 reduction to CO and CH_4, J. Alloys Compd. 983 (2024) 173730, https://doi.org/10.1016/j.jallcom.2024.173730.
[183] T. Wojciechowski, A. Rozmysłowska-Wojciechowska, G. Matyszczak, M. Wrzecionek, A. Olszyna, A. Peter, A. Mihaly-Cozmuta, C. Nicula, L. Mihaly-Cozmuta, S. Podsiadło, D. Basiak, W. Ziemkowska, A. Jastrzębska, Ti_2C MXene modified with ceramic oxide and noble metal nanoparticles: synthesis, morphostructural properties, and high photocatalytic activity, Inorg. Chem. 58 (2019) 7602–7614, https://doi.org/10.1021/acs.inorgchem.9b01015.
[184] M. Madi, M. Tahir, Highly stable $LaCoO_3$ perovskite supported g-C_3N_4 nanotextures with proficient charges migration for visible light CO_2 photoreduction to CO and CH_4, Mater. Sci. Semicond. Process. 142 (2022) 106517, https://doi.org/10.1016/j.mssp.2022.106517.
[185] J. Li, J. Zhang, J. Zhang, K. Pan, H. Xu, H. Chen, G. Liu, N. Wu, C. Yuan, X. Liu, Tailoring supports for enhancing the electrocatalytic hydrogen evolution performance of platinum species: a review, J. Mater. Chem. A 11 (2023) 19812–19844, https://doi.org/10.1039/D3TA04199A.
[186] J. Li, J. Zhang, J. Shen, H. Wu, H. Chen, C. Yuan, N. Wu, G. Liu, D. Guo, X. Liu, Self-supported electrocatalysts for the hydrogen evolution reaction, Mater. Chem. Front. 7 (2023) 567–606, https://doi.org/10.1039/D2QM00931E.
[187] W. Zhang, B. Huang, K. Wang, W. Yang, F. Lv, N. Li, Y. Chao, P. Zhou, Y. Yang, Y. Li, J. Zhou, W. Zhang, Y. Du, D. Su, S. Guo, WO x -surface decorated PtNi@Pt dendritic nanowires as efficient pH-universal hydrogen evolution electrocatalysts, Adv. Energy Mater. 11 (2021), https://doi.org/10.1002/aenm.202003192.
[188] P. Kuang, Z. Ni, B. Zhu, Y. Lin, J. Yu, Modulating the d-band center enables ultrafine Pt_3Fe alloy nanoparticles for pH-universal hydrogen evolution reaction, Adv. Mater. 35 (41) (2023) 2303030, https://doi.org/10.1002/adma.202303030.
[189] J. Li, N. Wu, J. Zhang, H.-H. Wu, K. Pan, Y. Wang, G. Liu, X. Liu, Z. Yao, Q. Zhang, Machine learning-assisted low-dimensional electrocatalysts design for hydrogen evolution reaction, Nano-Micro Lett 15 (2023) 227, https://doi.org/10.1007/s40820-023-01192-5.
[190] P.K.L. Tran, T.H. Nguyen, D.T. Tran, V.A. Dinh, T.T. Nga Ta, C.-L. Dong, N. H. Kim, J.H. Lee, Tunable charge Pt sites-dominated alloy confined by mxene-derived oxycarbide enables ultra-stable ampere-level hydrogen production, Appl. Catal. B Environ. Energy 363 (2025) 124801, https://doi.org/10.1016/j.apcatb.2024.124801.
[191] T.H. Nguyen, P.K.L. Tran, D.T. Tran, V.A. Dinh, N.H. Kim, J.H. Lee, Ru-Ru_2P hetero-cluster promoted V_2CT_x sheets-based electrocatalyst enables industrial-level AEM water electrolysis, Appl. Catal. B Environ. 343 (2024) 123517, https://doi.org/10.1016/j.apcatb.2023.123517.
[192] K. Chang, D.T. Tran, J. Wang, S. Prabhakaran, D.H. Kim, N.H. Kim, J.H. Lee, Atomic heterointerface engineering of Ni_2P-$NiSe_2$ nanosheets coupled ZnP-based arrays for high-efficiency solar-assisted water splitting, Adv. Funct. Mater. 32 (31) (2022) 2113224, https://doi.org/10.1002/adfm.202113224.
[193] F. Li, G.-F. Han, H.-J. Noh, J.-P. Jeon, I. Ahmad, S. Chen, C. Yang, Y. Bu, Z. Fu, Y. Lu, J.-B. Baek, Balancing hydrogen adsorption/desorption by orbital modulation for efficient hydrogen evolution catalysis, Nat. Commun. 10 (2019) 4060, https://doi.org/10.1038/s41467-019-12012-z.
[194] Y.-H. Pan, S. Perumal, M. Sakthivel, S.-N. Lin, M.-H. Yeh, W.-Y. Yu, K.-C. Ho, Reconstructed vanadium carbide MXene supported cerium based trimetallic phosphide as an efficient electrocatalyst for alkaline water splitting, Chem. Eng. J. 515 (2025) 163888, https://doi.org/10.1016/j.cej.2025.163888.
[195] G.T.M. Kadja, S.A.C. Natalya, F. Balqis, N.J. Azhari, N. Nurdini, A. Sumboja, R. S. Rahayu, U. Pratomo, M. Khalil, Irkham, gold nanoparticles−supported Ti_3C_2 MXene nanosheets for enhanced electrocatalytic hydrogen evolution reaction, Nano-Struct. Nano-Objects 36 (2023) 101059, https://doi.org/10.1016/j.nanoso.2023.101059.
[196] B. Sarfraz, M.T. Mehran, F. Shahzad, S. Hussain, S.R. Naqvi, H.A. Khan, K. Mahmood, Bifunctional CuS/Cl-terminated greener MXene electrocatalyst for efficient hydrogen production by water splitting, RSC Adv 13 (2023) 22017–22028, https://doi.org/10.1039/D3RA02581K.
[197] A. Patra, C.S. Rout, Architecturally robust $MoWS_2$ and $Ti_3C_2T_x$ MXene nanosheets hybrid for high-performance energy storage and conversion applications, Energy Storage 5 (2023) e411, https://doi.org/10.1002/est2.411.
[198] B. Sarfraz, M.T. Mehran, M.M. Baig, S.R. Naqvi, A.H. Khoja, F. Shahzad, HF free greener Cl-terminated MXene as novel electrocatalyst for overall water splitting in alkaline media, Int. J. Energy Res. 46 (2022) 10942–10954, https://doi.org/10.1002/er.7895.
[199] X. Zhao, K. Tang, C. Lee, C. Du, H. Yu, X. Wang, W. Qi, Q. Ye, Q. Yan, Promoting the water-reduction kinetics and alkali tolerance of MoNi 4 nanocrystals via a $Mo_2TiC_2T_x$ induced built-In electric field, Small 18 (15) (2022) 2107541, https://doi.org/10.1002/smll.202107541.
[200] Nabilah Saafie, Suriati Sufian, Farah Amelia Shahirah Roslan, Muhamad Irfan Khan, Optimization of synthesizing conditions for MXene (Ti_3C_2) photocatalyst: effect of LiF:Ti_3AlC_2 mass ratio, J. Adv. Res. Appl. Sci. Eng. Technol. 47 (2024) 183–192, https://doi.org/10.37934/araset.47.2.183192.
[201] X. Chen, Z. Zhou, F.O. Gudda, L. Tang, H. Wang, B. Czech, P. Oleszczuk, Y. Gao, Hydroxyl groups and vacancy defects modified Mo_2C MXene as peroxymonosulfate activator for antibiotics degradation, J. Clean. Prod. 486 (2025) 144540, https://doi.org/10.1016/j.jclepro.2024.144540.
[202] H. Zhang, H. Ding, W. Wang, J. Zhao, B. Sun, Y. Xia, G. Li, X. Chang, Air plasma activation of catalytic sites within MXene nanosheets for oxygen evolution and urea oxidation catalysis, Mater. Today Energy 44 (2024) 101623, https://doi.org/10.1016/j.mtener.2024.101623.
[203] D.-E. Lee, A. Ali, K.T. Kang, M. Danish, W.-K. Jo, Advancing the integration of covalent-organic-framework with organic, inorganic, and polymeric materials for light-assisted green H_2 generation: a review of emerging trends, Mater. Sci. Eng. R Rep. 161 (2024) 100858, https://doi.org/10.1016/j.mser.2024.100858.
[204] M. Chen, Q. Fan, P. Yu, K. Chen, P. Li, K. Liang, Engineering Ti_3C_2-MXene surface composition for excellent Li^+ storage performance, Molecules 29 (2024) 1731, https://doi.org/10.3390/molecules29081731.
[205] M.Z. Abid, K. Rafiq, A. Rauf, E. Hussain, Unveiling the potential of MXene-fabricated catalysts: an effective approach for H_2 generation from water splitting, Nanoscale Adv. 6 (2024) 5861–5873, https://doi.org/10.1039/D4NA00754A.
[206] J. Long, Q. Yao, J. Xia, Z.-H. Lu, Modulating electronic density of active metal site via MXene intercalated by alkali ions for superior hydrogen production, Appl. Catal. B Environ. Energy 363 (2025) 124823, https://doi.org/10.1016/j.apcatb.2024.124823.
[207] Z. Wei, Z. Zhao, C. Qiu, S. Huang, Z. Yao, M. Wang, Y. Chen, Y. Lin, X. Zhong, X. Li, J. Wang, Tripodal Pd metallenes mediated by Nb_2C MXenes for boosting alkynes semihydrogenation, Nat. Commun. 14 (2023) 661, https://doi.org/10.1038/s41467-023-36378-3.
[208] S. Liu, F. Hu, W. Shao, W. Zhang, T. Zhang, C. Song, M. Yao, H. Huang, X. Jian, A novel strategy of In situ trimerization of cyano groups between the $Ti_3C_2T_x$ (MXene) interlayers for high-energy and high-power sodium-ion capacitors, Nano-Micro Lett. 12 (2020) 135, https://doi.org/10.1007/s40820-020-00473-7.
[209] H. Huang, J. Qin, C. Liu, L. Luo, Y. Lan, L. Yang, J. Zhang, H. He, Constructing Zn-based MOF-MXene nanoarchitectures to stabilize ultrafine Pt nanocrystals with enhanced methanol oxidation performance, Carbon N. Y. 226 (2024) 119171, https://doi.org/10.1016/j.carbon.2024.119171.
[210] C. Sun, Y. Yang, L. Zhao, H. Zhan, S. Cheng, Carbonized spider silk/V_2CT_x heterostructured electrocatalysts for efficient hydrogen evolution reaction, J. Mater. Sci. 59 (2024) 21895–21908, https://doi.org/10.1007/s10853-024-10475-0.
[211] W. Fan, C. Jin, C. Peng, F. Ren, G. Li, Q. Gu, $SrTiO_3$/$Ti_3C_2T_x$ schottky heterojunction as a promising high-efficiency photocatalyst for H_2 evolution, Appl. Phys. Lett. (2022) 121, https://doi.org/10.1063/5.0121818.
[212] S. Singh, A. Raucci, W. Cimmino, A. Numan, M. Khalid, S. Cinti, Bismuth-MXene nanocomposite: a low-cost portable solution for zinc (II) detection in water for safer environmental monitoring, Sens. Actuators B Chem. 418 (2024) 136219, https://doi.org/10.1016/j.snb.2024.136219.
[213] S. Singh, A. Numan, M. Khalid, I. Bello, E. Panza, S. Cinti, Facile and affordable design of MXene-Co_3O_4 -based nanocomposites for detection of hydrogen peroxide in cancer cells: toward portable tool for cancer management, Small 19 (2023), https://doi.org/10.1002/smll.202208209.
[214] F.E. Ab Latif, A. Numan, N.M. Mubarak, M. Khalid, M.A.A. Mohd Abdah, W. P. Wong, Enhanced dopamine detection using $Ti_3C_2T_x$/rGO/Pt ternary composite synthesized via microwave-assisted hydrothermal method, Mater. Today Sustain. 28 (2024) 100996, https://doi.org/10.1016/j.mtsust.2024.100996.
[215] S. Zhou, X. Yang, W. Pei, N. Liu, J. Zhao, Heterostructures of MXenes and N-doped graphene as highly active bifunctional electrocatalysts, Nanoscale 10 (2018) 10876–10883, https://doi.org/10.1039/C8NR01090K.
[216] J. Wang, W. Ming, L. Chen, T. Song, M. Yele, H. Zhang, L. Yang, G. Sarula, B. Liang, L. Yan, G. Wang, MoS_2 lubricate-toughened MXene/ANF composites for multifunctional electromagnetic interference shielding, Nano-Micro Lett. 17 (2025) 36, https://doi.org/10.1007/s40820-024-01496-0.
[217] M. Fan, L. Liu, Y. Li, F. Gu, X. He, H. Chen, Highly dispersed Ir nanoparticles on $Ti_3C_2T_x$ MXene nanosheets for efficient oxygen evolution in acidic media, J. Colloid Interface Sci. 679 (2025) 676–685, https://doi.org/10.1016/j.jcis.2024.10.009.
[218] W. Zhang, L. He, Y. Chen, Z. Wu, P. Yu, K. Chen, F. Ge, M. Li, L. Yu, N. Lin, H. B. Hawash, K. Liang, Unraveling the potential of MXenes as multifunctional cathodes: innovations and challenges for next-generation energy storage systems, Mater. Sci. Eng. R Rep. 164 (2025) 100975, https://doi.org/10.1016/j.mser.2025.100975.

[219] D.T.K. Anh, P.H. Minh, K. Yamanoi, M. Cadatal-Raduban, L.V. Mui, D.M. Hieu, N. D. Hung, Electronic, optical and thermoelectric properties of two-dimensional molybdenum carbon Mo_2C-MXenes, Appl. Sci. 14 (2024) 9257, https://doi.org/10.3390/app14209257.
[220] E. Marquis, F. Benini, B. Anasori, A. Rosenkranz, M.C. Righi, Effect of vacancies and edges in promoting water chemisorption on titanium-based MXenes, Nano Converg. 10 (2023) 16, https://doi.org/10.1186/s40580-023-00364-8.
[221] Y. Chen, X. Chen, X. Xu, H. Liu, C. Guo, X. Li, J. Pu, W. Gong, Y. Liu, P. Xue, J. Han, Synergistically enhancing ion migration kinetics and inducing orientation deposition for dendrite-free aqueous zinc-ion batteries, Energy Storage Mater. 71 (2024) 103676, https://doi.org/10.1016/j.ensm.2024.103676.
[222] J. Peng, W. Han, T. Wu, L. Song, Y. Yin, C. Wang, A superhydrophobic e-fabric based on polydopamine template-assisted MXene/MWNTs with strain sensing, EMI shielding and electrothermal performance for health management, J. Alloys Compd. 990 (2024) 174514, https://doi.org/10.1016/j.jallcom.2024.174514.
[223] F. Yang, P. Zhang, J. Qu, X. Yang, Y. Cai, C.Ming Li, J. Hu, Highly efficient photoenzymatic CO_2 reduction dominated by 2D/2D MXene/C_3N_5 heterostructured artificial photosynthesis platform, J. Colloid Interface Sci. 678 (2025) 1121–1131, https://doi.org/10.1016/j.jcis.2024.08.149.
[224] C. Croisé, X. Courtois, S. Célérier, L. Loupias, C. Canaff, J. Rousseau, N. Bion, F. Can, (Ru-)Mo_2C (MXene) catalysts for ammonia synthesis: from Haber-Bosch to chemical looping processes, Mater. Today Catal. 7 (2024) 100066, https://doi.org/10.1016/j.mtcata.2024.100066.
[225] S. Guo, Y. Zheng, X. Zhang, X. Lei, H. Sun, T. Wen, Carbon nanoplating stabilization of hierarchical MXene@C@MnO_2 catalyst for effective Fenton-like reaction, Appl. Catal. A Gen. 670 (2024) 119543, https://doi.org/10.1016/j.apcata.2023.119543.
[226] Y. Yan, F. Morfin, B.-B. Xiao, H. Guesmi, M. Aouine, M. Prévot, S. Morisset, S. Célérier, L. Piccolo, $Mo_2Ti_2C_3T_X$ MXene performance in catalytic CO_2 hydrogenation and its promotion with single Pt atoms, Mater. Today Catal. 7 (2024) 100069, https://doi.org/10.1016/j.mtcata.2024.100069.
[227] A. Cui, P. Meng, J. Hu, H. Yang, Z. Yang, H. Li, Y. Sun, Fabrication of high-performance cell-imprinted polymers based on AuNPs/MXene composites via metal-free visible light-induced ATRP, Analyst 148 (2023) 1058–1067, https://doi.org/10.1039/D2AN01896A.
[228] X. Xu, L. Li, W. Liu, Z. Chen, D. Chen, G. Shen, Thermally chargeable supercapacitor with 3D $Ti_3C_2T_x$ MXene hollow sphere based freestanding electrodes, Adv. Mater. Interfaces 9 (2022), https://doi.org/10.1002/admi.202201165.
[229] N. Abdullah, N.A.I.M. Ishak, K.H. Tan, M.A. Zaed, R. Saidur, A.K. Pandey, Investigating the impact of various etching agents on $Ti_3C_2T_x$ MXene synthesis for electrochemical energy conversion, FlatChem 47 (2024) 100730, https://doi.org/10.1016/j.flatc.2024.100730.